University of Canterbury

Ph.D Thesis

Free-Electron Laser and Synchrotron Spectroscopy of Fundamental Excitations in Ytterbium-Doped Fluoride Lattices

Author:
Rosa B. Hughes-Currie

Supervisor:
Assoc. Prof. Jon-Paul Wells

Co–supervisor:
Prof. Mike Reid

Submitted in Partial Fulfillment of the Requirements for the Degree
Doctor of Philosophy in Physics

June 18, 2015

Abstract

The spectroscopy of wide-bandgap fluoride materials doped with divalent ytterbium is presented. The structure of impurity-trapped excitons is explored, vacuum ultraviolet excitation is used to investigate the transfer processes between excitations, and the effect of confinement on self-trapped excitons is studied.

The excited-state structure of impurity-trapped excitons is measured in the multisite system $NaMgF_3$:Yb^{2+}. A two-colour ultraviolet-infrared pulsed photoluminescence enhancement technique is employed to probe the interlevel transitions and dynamics of impurity-trapped excitons in doped insulating phosphor materials. $NaMgF_3$:Yb^{2+} exhibits emission from two charge-compensation centres with peaks at 22 300 cm^{-1} (448 nm) and 24 000 cm^{-1} (417 nm). The observed photoluminescence enhancement is caused by a combination of intra-excitonic excitation and electron trap liberation. The electron traps are inferred to have a depth of approximately 800 cm^{-1}.

Time-resolved VUV spectroscopic studies of emission and excitation spectra of CaF_2:Yb, $NaMgF_3$:Yb and MgF_2:Yb are presented to investigate excitation and relaxation mechanisms of both impurity-trapped excitons and intrinsic excitons in each fluoride host. Host-to-impurity energy transfer mechanisms leading to formation of impurity-trapped excitons are discussed. The $4f^{14} \rightarrow 4f^{13}5d$ CaF_2:Yb^{2+} absorption bands are successfully modeled with a semi-empirical effective Hamiltonian calculation for $NaMgF_3$:Yb^{2+} and MgF_2:Yb^{2+}. The excitation and emission spectra of all studied materials are compared.

Results on VUV spectroscopy of 3 and 5 monolayer CdF_2–CaF_2 superlattices show the change in optical behaviour of the self-trapped exciton in CdF_2 when it is confined and give an indication of the radius of the exciton. The decay of the emission is modeled with three components, corresponding to three self-trapped exciton states. Results on the VUV spectroscopy of CdF_2–CaF_2 superlattices show that the confinement effect seems to equally influence the energy of excitonic and bandgap absorption in 3 and 5 monolayer superlattices. At the same time, as the self-trapped exciton is more confined, the emission is blue-shifted by 1600 cm^{-1} indicating that the effective excitonic radius is about three monolayers.

Acknowledgements

My first and largest thanks go to mum and dad, for giving me a sense of wonder at the universe, and for all the love and support through many years of study.

Assoc. Prof. Jon-Paul Wells and Prof. Mike Reid were excellent supervisors. They provided me with ample direction and encouragement, and facilitated my growth as an independent scientist.

I am very thankful for Prof. Roger Reeves taking the time for some thorough editing of manuscripts. His high standards have greatly improved my writing and his keen interest in the work made our discussions a pleasure.

To my collaborators: Dr. Pubudu Senanyake, Alex Salkeld, and Dr. Konstantin Ivanovskhih, I'm glad our many hours of work together have proved so fruitful, and thanks for your effort and support.

The beam scientists at the facilities we used all went above and beyond the duties of their job to help us make the most of our limited time. Dr. Robert Gordon at APS was in particular very obliging. Dr. Giel Berden at FELIX was proficient and helpful, as well as Dr. Aleksei Kotlov at DESY.

Dr. Andries Meijerink kindly provided the MgF_2:Yb and $NaMgF_3$:Yb samples used in this study, and showed enthusiastic interest in the work at FELIX and DESY.

Dr. Lynda Soderholm's group at the Chemistry Division of Argonne was very hospitable to me. In particular Dr. Mark Antonio was invaluable in helping analyse the XANES data we collected.

Many thanks to all my colleagues in the Physics department, especially Alex Neiman, Jade Bennett, Lancia Hubley, Sophie Koster, Emil Schroder, Chrissy Emeny and Dr. Ian Farrell. At the time of printing the total number of cakes we have shared together in the office on Friday afternoons stands at 81. I'm lucky to have had such a great bunch of friends to work with.

The support of the University of Canterbury through a scholarship and the Department of Physics and Astronomy at the University of Canterbury through teaching opportunities are acknowledged.

This thesis is dedicated to my nieces, Isabella Louise Hughes-Scott and Olivia Wendy Grace Hughes. I hope they are never held back from mastering anything they think is useful and interesting, and I know that they will achieve things so amazing that I can't even imagine them yet.

Banish Air from Air
Divide Light if you dare

—Emily Dickinson

Contents

Figures xi

Tables xv

1 Introduction 1

1.1 Lanthanide Spectroscopy 2

1.2 Impurity-Trapped Excitons 4

1.2.1 Anomalous Luminescence and Impurity-Trapped Excitons 4

1.2.2 Impurity-Trapped Excitons in CaF_2:Yb^{2+} 8

1.2.3 Impurity-Trapped Excitons in $NaMgF_3$:Yb^{2+} 10

1.2.4 Emission from MgF_2:Yb^{2+} 10

1.3 Charge Transfer Transitions 11

1.4 Self-Trapped Excitons 11

1.4.1 Structural Intrepretation of STEs 12

1.4.2 Recombination Luminescence 15

1.5 Outline 17

2 Theoretical Background 19

2.1 Crystal Field Calculations 19

2.1.1 Constructing an Effective Hamiltonian 20

2.1.2 Central Field Approximation 20

2.1.3 Free Ion Parameters 21

2.1.4 Crystal Field Parameters 22

2.1.5 Transition Intensity Calculations 23

2.1.6 The Superposition Model 25

2.1.7 Modelling Excitons With Crystal Field Theory 25

2.2 Rate Equations 26

3 Experimental Methods 32

3.1 Sample Growth 32

3.1.1 Bulk Crystals 32

3.1.2 Superlattices 33

3.2 Characterisation Measurements 34

3.3 XANES Fluorescence Measurements 35

3.4 Site-Selective Two-Colour Photoluminescence Enhancement 37

3.5 Vacuum Ultraviolet Spectroscopy 41

4 Material Characterisation 43

4.1 Optical Absorption Measurements of Yb-doped CaF_2, SrF_2, and $NaMgF_3$ 43

4.2 ITE Emission from Photoluminescence Measurements 44

4.3 X-ray Luminescence Spectra 47

4.4 Valency Measurements using the XANES Technique 49

4.5 Conclusion 53

5 SSTPE of ITEs in $NaMgF_3$:Yb^{2+} 55

5.1 Site-Selective Transient Photoluminescence Enhancement 56

5.2 Two-Dimensional Spectroscopy 56

5.3 Intra-Excitonic Absorption 63

5.4 Analysis of Emission Dynamics 65

5.4.1 IR Power Dependence 69

5.4.2 Temperature Dependence 74

5.4.3 Wavelength Dependence 78

5.4.4 UV Power Dependence 80

5.4.5 Trap Liberation 80

5.5 Conclusion 82

6 Vacuum Ultraviolet Spectroscopy 85

6.1 CaF_2:Yb 86

6.1.1 Emission and Excitation Measurements of CaF_2 86

6.1.2 Temperature Dependence of CaF_2 Free Exciton Peak 92

6.2 $NaMgF_3$:Yb 98

6.2.1 Emission and Excitation Measurements of $NaMgF_3$:Yb 98

6.2.2 Intraconfigurational Transistions of $NaMgF_3$:Yb 101

6.3 MgF_2:Yb 109

6.4 Comparisons Between Materials 115

6.5 Conclusion 118

7 CdF_2-CaF_2 Superlattices 120

7.1 Background Work 120

7.1.1 Cadmium Fluoride 121

7.1.2 Previous work on CdF_2-CaF_2 Superlattices 122

7.2 Results 123

7.3 Conclusion 129

8 Conclusions and Future Work **132**

References **136**

A Additional Experimental Techniques **151**

A.1 Electron Paramagnetic Resonance 151

A.2 Density Functional Theory 153

A.3 X-ray Photoelectron Spectroscopy 154

Figures

1.1 Trivalent Dieke diagram. 5

1.2 Divalent Dieke diagram. 6

1.3 An illustration of an ITE. 7

1.4 Temperature-dependence of peak emission from CaF_2:Yb^{2+}. 8

1.5 Configurational coordinate diagram of an ITE. 9

1.6 Illustration of a V_K centre in CaF_2. 12

1.7 Illustration of an H (or V_H) centre and a fluoride anion vacancy in CaF_2. 13

1.8 Schematic of the suggested geometry of the self-trapped hole in $KMgF_3$. 14

1.9 Schematic of the suggested geometry of the STE and F-H pairs in MgF_2. 15

1.10 The states involved in recombination luminescence of STEs in alkali halides. 16

2.1 Schematic showing the rates between energy levels in a simple 3-level model. 27

2.2 Thermal equilibrium between three energy levels at a temperature of 300 K. 28

2.3 Thermal equilibrium between three energy levels at a temperature of 50 K. 29

2.4 Population distribution and intensity between three energy levels as temperature changes. 29

2.5 Shape of IR excitation pulse. 31

2.6 Modelled transients with the IR excitation. 31

3.1 Illustration of an X-ray fluorescence process. 36

3.2 Illustration of the X-ray fluorescence measurement setup at 20-BM. 36

3.3 The Si 111 double crystal monochromator. 37

3.4 The experimental hutch for 20-BM. 38

3.5 A schematic of the SSTPE method. 39

3.6 Schematic of the VUV fluorescence measurement setup at SUPERLUMI. 42

4.1 Excitation and absorption of fluoride crystals doped with Yb at a sample temperature of 10 K. 45

4.2 Emission of fluoride crystals doped with Yb excited into a Yb^{2+} $5d$ levels. 46

4.3 X-ray luminescence of CaF_2:Yb at 4 K excited at 8949 eV at two Yb concentrations. 48

4.4 X-ray luminescence of SrF_2:Yb at 4 K excited at 8949 eV. 48

4.5 X-ray luminescence of $NaMgF_3$:Yb excited at 8949 eV at two sample temperatures. 49

4.6 XANES edge fit for $NaMgF_3$:0.5%Yb^{2+}. 51

4.7 XANES edge fit for CaF_2:Yb and SrF_2:Yb. 54

5.1 Two-dimensional emission spectrum of $NaMgF_3$:Yb^{2+}. 57

5.2 8 K emission spectrum of $NaMgF_3$:Yb^{2+}. 58

5.3 Time evolution of the SSTPE excitation spectrum of $NaMgF_3$:Yb^{2+}. 61

5.4 8 K site-selective excitation spectra of $NaMgF_3$:Yb^{2+}. 62

5.5 Integrated emission of $NaMgF_3$:Yb^{2+} at 8 K. 64

5.6 The energy level transitions involved in the dynamic behaviour of $NaMgF_3$:Yb^{2+} after IR excitation. The transitions are labeled with the rates used in Equations 5.3-5.7. W terms represent rates of non-radiative transitions. F terms are mechanisms driven by the IR pulse, which are the population transfer from the lower to higher excitonic states (F_{24}) and electrons released from traps (F_{TC}). A_{21} and A_{31} are the radiative rates from the ITE levels. 68

5.7 IR power-dependent dynamics of the IR enhancement of $NaMgF_3$:Yb^{2+}. 72

5.8 The parameter values for the transients varying with IR fluence and temperature. The circles are the optimal values of the parameters used to model the transients in Figs. 5.7 and 5.9 and the lines are the fits to those values, described in the Equations5.10–5.14. 73

5.9 Temperature-dependent dynamics of the IR enhancement of $NaMgF_3:Yb^{2+}$. 76

5.10 Temperature-dependent dynamics of the IR enhancement of $NaMgF_3:Yb^{2+}$ at a lower IR excitation power. 77

5.11 IR wavelength-dependent dynamics of the $NaMgF_3:Yb^{2+}$ IR enhancement. 79

5.12 The IR enhancement of $NaMgF_3:Yb^{2+}$ as the UV pre-pulse power varies. 81

5.13 The trap population for three emission energies. 83

6.1 Emission from CaF_2:0.1%Yb at a sample temperature of 8 K. 88

6.2 Schematic of the VUV spectroscopy measurement. 89

6.3 Emission from CaF_2:0.1%Yb after VUV excitation. 90

6.4 VUV Excitation spectra of $CaF_2:0.05\%Yb^{2+}$. 93

6.5 VUV Excitation spectra of CaF_2:Yb at three concentrations. 94

6.6 Emission spectra of CaF_2:Yb for various concentrations of Yb doping. 95

6.7 The energy shift of the free exciton excitation peak in CaF_2:Yb as a function of temperature. 96

6.8 Modelling the energy shift of the free exciton excitation peak in CaF_2 with Viña's equation. 97

6.9 Emission from $NaMgF_3$:Yb after VUV excitation. 99

6.10 VUV Excitation spectra of $NaMgF_3$:0.6%Yb. 100

6.11 Emission from $NaMgF_3$:0.6%Yb after VUV excitation. 102

6.12 Emission from $NaMgF_3$:0.6%Yb modeled with Gaussians. 103

6.13 The nearby F^- ions around Yb^{2+} in $NaMgF_3$. 105

6.14 Tetragonal site with lateral elongation used to approximate the crystal field acting on Yb^{2+} for $NaMgF_3$:Yb^{2+}. 106

6.15 Simulated spectrum of $NaMgF_3$:Yb^{2+} from a semi-empirical crystal field model. 107

6.16 Emission from MgF_2:Yb at a sample temperature after VUV excitation. 110

6.17 VUV excitation spectra of MgF_2:Yb. 111

6.18 Emission from MgF_2:Yb after above-bandgap excitation. 112

6.19 Simulated spectrum of MgF_2:Yb calculated with a semi-empirical crystal field model. 113

6.20 Comparison between excitation spectra of Yb in CaF_2, MgF_2, and $NaMgF_3$. 116

6.21 Emission of Yb-doped CaF_2, MgF_2, and $NaMgF_3$. 117

7.1 Schematic of the CdF_2–CaF_2 superlattice structure. 121

7.2 Energy-band diagram for the CdF_2-CaF_2-Si(111) heterostructure. 122

7.3 Emission spectra from CdF_2–CaF_2 superlattices. 125

7.4 Excitation from CdF_2–CaF_2 superlattices. 128

7.5 Emission decay kinetics from CdF_2–CaF_2 superlattices. 130

A.1 The simulated absorption spectrum of a system of free electrons in a varying magnetic field. 152

Tables

2.1 Parameter values for a toy rates model. 28

4.1 Lattice constants of fluoride crystals. 44

4.2 Absorption and emission frequencies for Yb^{2+}-doped fluorides. 47

4.3 Parameters for edge fitting XANES data. 52

5.1 Parameters for Gaussian function fits of $NaMgF_3$:Yb^{2+} emission. 59

5.2 The postitions and widths of the peaks in Figure 5.5. 63

5.3 Parameter values for modeling $NaMgF_3$:Yb^{2+} emission. 69

5.4 Comparison of indicated and modeled temperature for a range of IR powers. 70

5.5 The values for Equations 5.10–5.12 that were found by fitting the change optimal rate equation parameters with IR fluence in figure Figure 5.8. 74

5.6 Comparison of the modeled temperatures used to calculate the emission dynamics for a range of indicated temperatures (shown in Figure 5.9). Uncertainties in model temperature are approximately 0.5 K. 74

5.7 The values for Equations 5.13–5.14 that were found by fitting the change optimal rate equation parameters with temperature in figure Figure 5.8. 75

5.8 Parameter values for the rate equation model as a function of IR wavelength. 80

6.1 The parameters used to fit Gaussian functions. 104

6.2 Calculated coordinates of nearby F^- ions for Yb^{2+} in $NaMgF_3$. 105

6.3 Crystal field parameters for Yb^{2+} in $NaMgF_3$ and MgF_2. 108

6.4 Value of intrinsic parameters for CaF_2:Yb^{2+}, $NaMgF_3$:Yb^{2+} and MgF_2:Yb^{2+}. 114

6.5 Bandgap and free exciton energies for alkali fluorides measured by reflection. 115

7.1 Peak position of intrinsic emission observed in CdF_2–CaF_2 superlattices. 126

7.2 Parameters fitted to the superlattice emission transients. 129

Chapter 1

Introduction

Lanthanide-doped crystalline phosphors form the basis of many technologies. Lanthanide phosphors are used in fluorescent and LED lighting, in fibre optic amplifiers [1], and as scintillator materials [2, 3]. New phosphors are being developed to create efficient LED lighting [4] and high-power picosecond lasers [5].

This thesis concentrates on two excitations which occur in lanthanide-doped crystalline phosphors: impurity-trapped excitons and self-trapped excitons. By contributing to the fundamental understanding of these temporary defects in the crystal lattice, this thesis adds to our knowledge of the processes which occur in scintillators and phosphors and will support a greater ability to engineer more useful materials, as well as developing a more complete model of how light interacts with complex crystalline materials.

Impurity-trapped excitons (ITEs) play an important role in the relaxation processes of the highly-excited states of lanthanide ions used in phosphor materials. They are crucial to the processes by which scintillator materials convert X-rays to UV radiation [3, 6, 7]. Studying ITEs in efficient scintillator materials directly is difficult since the ITEs that form in these systems generally relax non-radiatively and so have to be studied indirectly. However, there are some material systems for which the photoluminescence appears to come directly from ITE states. In particular, certain fluoride crystals doped with Yb^{2+} are observed to have wide emission bands compared to $4f^{13}5d \rightarrow 4f^{14}$ transitions [8] and large Stokes shifts, suggesting the emission is from ITEs which are being formed on the ytterbium ions [9].

The self-trapped exciton (STE) is a lattice excitation that occurs in many ionic crystals. STEs are electron-hole pairs trapped in temporary lattice distortions [10]. STEs are often a first step in creating other radiation-induced defects, so understanding STEs provides a basis for further investigation of defects which occur upon high energy excitation of crystals [11].

Both ITEs and STEs are excitations which commonly occur in rare earth phosphors during scintillation processes. However there is still much to understand about ITEs and STEs as they usually occur as part of a sequence of relaxation processes and there is often no emission from ITE or STE states. By studying materials where direct emission from ITE and STE states is seen, we can understand more about their energy level structure and explore how energy is transfered to these states after the crystal is excited above the band gap. The materials studied in this thesis are the insulating bulk crystals CaF_2:Yb, SrF_2:Yb, $NaMgF_3$:Yb and MgF_2:Yb as well as CdF_2–CaF_2 superlattices. The materials contain both Yb^{2+} and Yb^{3+}: The valency of Yb is described in more detail in Chapter 4. The ITE emission is associated with Yb^{2+}, but Yb^{3+} features can also been seen in X-ray luminescence in Chapter 4 and the vacuum ultraviolet spectra in Chapter 6.

1.1 Lanthanide Spectroscopy

Lanthanides are the chemical elements with atomic numbers 57 to 71. Together with scandium and yttrium these elements are also known as "rare earths". When lanthanides are in divalent or trivalent valency states in crystals, their valence electrons are in the $4f$ shell. The $4f$ shell is contracted and shielded from surroundings by the closed $5s$ and $5p$ shells [12]. The outer shells determine the chemical bonding of the ion, which means the chemistry is very similar across the lanthanide series.

Lanthanide ions in solids have very unique spectroscopic properties which make them useful in luminescent materials for various optical applications [13]. The shielded $4f$ shell of the lanthanide ions means the local crystal environment doesn't strongly affect their intraconfigurational $4f^n$ transitions. The transitions are characterised by sharp atomic lines which can be predicted for any host material.

The $5d$ shell of the lanthanides is distributed much further from the centre of the ion than the $4f$ shell, and the $5d$ shell is not shielded from the lattice surrounding the ion. Therefore the crystal field from the host material has a huge effect on the position of the $4f^{n-1}5d^1$ energy levels. In contrast to the intraconfigurational $4f^n$ transitions, the lowest $5d$ absorption frequency for the same lanthanide ion in two different crystals can differ in energy by as much as 10 000 cm^{-1} [14]. The $4f^{n-1}5d - 4f^n$ transitions are parity allowed, and are associated with intense absorption and emission bands.

The difference in energy between the absorption and emission bands is the Stokes shift. There is a Stokes shift of around 2000 cm^{-1} due to the low spin and high spin states

of the $4f^{13}5d^1$ configuration. When Yb^{2+} is in the $4f^{13}5d$ configuration, the exchange interaction between the $4f$ electrons and the $5d$ electron leads to a splitting of the $4f^{13}5d^1$ configuration into high spin and low spin states. The low spin state is typically located about 2000 cm^{-1} above the high spin state. The transition probability from the low spin $4f^{14}$ ground state into the low spin $4f^{13}5d^1$ state is much stronger than the transition from the $4f^{14}$ ground state into the high spin $4f^{13}5d^1$ state. $4f^n \rightarrow 4f^{n-1}5d^1$ emission is from the lowest $5d$ level, which is the high spin state. This difference in the spin states which are absorbed into and emitted from accounts for some of the Stokes shift seen for $4f^{n-1}5d^1$ to $4f^n$ transitions, but there is a greater Stokes shift caused by the bond length change of the transition.

The broad emission bands characteristic of $4f^{n-1}5d^1$ to $4f^n$ transitions are caused by the change in bond length between the lanthanide ion and surrounding ligands and make the energy levels of the $4f^{n-1}5d^1$ states harder to assign than the sharp emission lines of the $4f^n$ transitions. $4f^{n-1}5d^1$ to $4f^n$ transitions have a Stokes shift because of the large change in bond length which is additional to the Stokes shift associated with the high and low spin states of the $4f^{n-1}5d^1$ configuration.

General rules are being developed to predict the $5d$ energy levels of a particular lanthanide system because the high intensity of the transitions from these levels are useful for many applications. Dorenbos created a semi-empirical model for predicting the positions of the lowest $5d$ level for trivalent [15] and divalent lanthanide ions [14]. In 2002 van Pieterson et al.[16, 17] published excitation spectra and analysis of trivalent lanthanides in $LiYF_4$, CaF_2, and YPO_4. Many energy levels could be identified from analysis of the zero-phonon lines and vibrational bands.

The $4f^n$ transitions were studied in various systems before the 1960s. Many pieces of research identifying energy levels for each lanthanide ion from the absorption spectra of lanthanum chloride were presented together by Dieke in 1968 [18]. They are often presented in an energy level diagram known as the "Dieke diagram" shown in Figure 1.1. This diagram is a graphical representation of the energy of all configurations for each lanthanide. The original diagram was for trivalent lanthanides and did not include $4f^{n-1}5d$ transitions. This is because the $5d$ states are all at high energies (over 40 000 cm^{-1} above the ground state) for trivalent lanthanides. Populating the $4f^{n-1}5d^1$ levels most often requires high energy excitation sources. In the last two decades vacuum ultraviolet excitation sources have become more widespread, and the need for high energy scintillator materials has increased, so more research has been performed to extend the trivalent

Dieke diagram [19].

The $5d$ states are much lower for divalent lanthanides. Work began on modelling Yb $5d$ levels in the 1960s [20]. Figure 1.2 (taken from Dorenbos' paper on $4f^{n-1}5d^1 \rightarrow 4f^n$ transitions in divalent lanthanides [14]) shows the $4f$ levels and the position of the first $5d$ level across the series. The $5d$ levels are accessible for most lanthanides with optical photons. The gap between the lowest $4f$ and the lowest $5d$ level increases until the $4f$ shell is half-full, and then rises again until the shell is full. This means Eu^{2+} and Yb^{2+} have much higher $5d$ levels than other divalent lanthanide ions.

1.2 Impurity-Trapped Excitons

An impurity-trapped exciton (ITE) is an electron-hole pair trapped around an impurity centre. Although excitons may also be trapped around impurities in semiconductors, the term "impurity-trapped exciton" refers to impurities in ionic crystals [6]. They are created by exciting divalent impurities in the crystal. Figure 1.3 shows an illustration of an ITE located at a lanthanide impurity centre in a fluoride crystal with some arbitrary divalent cation (labelled M^{2+}). After excitation, a valence electron of the Ln^{2+} centre becomes delocalised and the Ln^{2+} centre becomes a Ln^{2+} and hole. The ITE consists of the hole trapped around the Ln^{2+} centre and an electron delocalised on the surrounding cations [9]. ITEs are created when the valence electrons of ions are excited into a state near or in the conduction band, so that the lanthanide ion is autoionized and the electron can become delocalised on the surrounding cations. The delocalised electron is bound to the hole that is trapped at the impurity site [21].

1.2.1 Anomalous Luminescence and Impurity-Trapped Excitons

In the 1960s Kaplyanskii and Feofilov identified the emission band from CaF_2:Yb^{2+} and BaF_2:Eu^{2+} as being "anomalous" [22]. The emission was termed "anomalous" because it was shifted to a much lower energy than the corresponding absorption band, a shift much greater than the expected Stokes shift. They proposed that the shift might be caused by some involvement of the $6s$ states. Reut later suggested a transition from a charge transfer state [23]. More experimental work was carried out by Kaplyanskii on the excitation and emission decay of CaF_2:Yb^{2+} and the results were attributed to the Jahn-Teller effect [24]. ITEs occuring in insulators were first reported in the 1960s in systems

Figure 1.1 Original Dieke diagram showing the positions of $4f$ trivalent lanthanide energy levels [18].

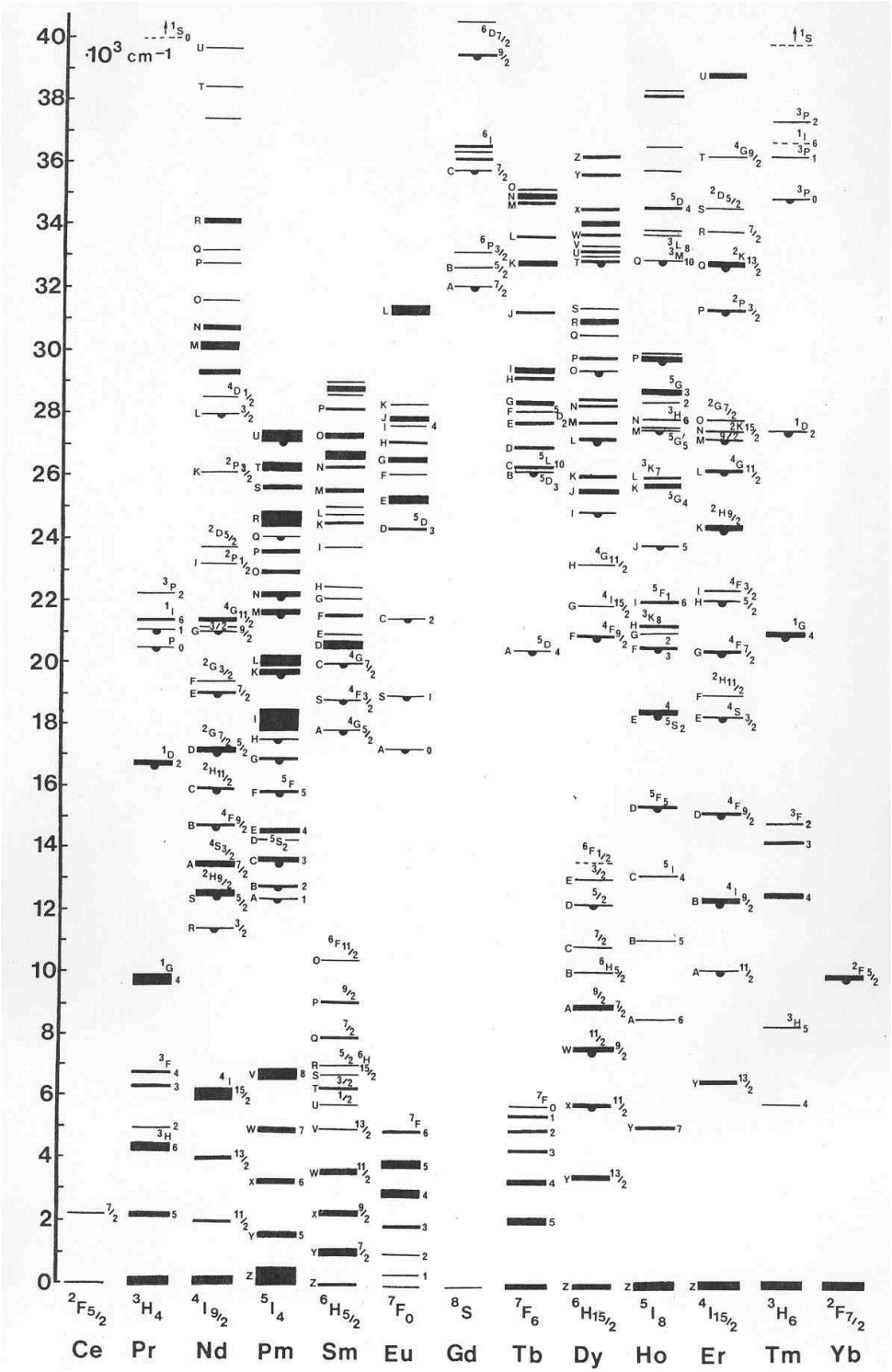

Figure 1.2 Dieke diagram showing the positions of $4f$ divalent lanthanide energy levels. The line shows the position of the first $5d$ level across the series [14].

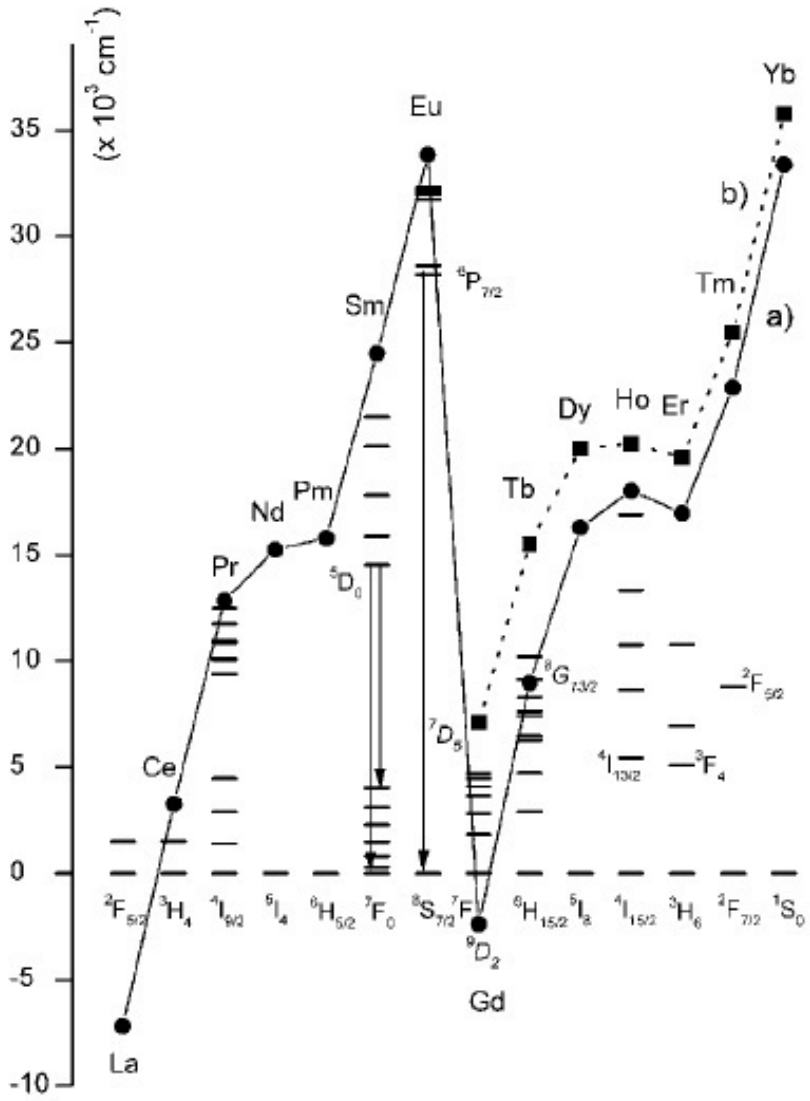

Figure 1.3 An illustration of an ITE [9]. The hole is trapped on the lanthanide ion (Ln^{2+}) and the electron is delocalised around the surrounding cations (M^{2+}).

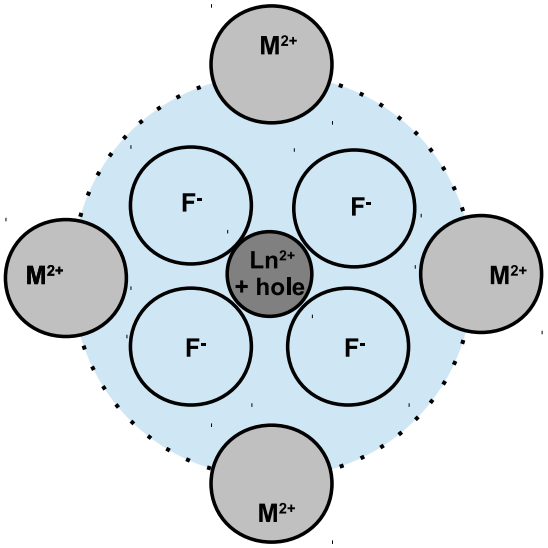

of divalent metal ions doped into manganese fluoride [25] and in the 1980s McClure and Pedrini [21] suggested that the "anomalous" emission could be caused by an ITE. Pedrini and Moine then measured the temperature dependence of the emission from CaF_2:Yb^{2+} and SrF_2:Yb^{2+} and proposed that the large Stokes shifts in these systems were caused by the formation of ITEs [26, 27].

Moine and Pedrini determined the energy from the impurity states to the conduction band by photoconductivity measurements and found for CaF_2:Yb^{2+}, SrF_2:Yb^{2+} and BaF_2:Yb^{2+} the $5d$ states overlap the conduction band, so the outer valence electron of the $4f^{13}5d$ configuration can become delocalised over neighbouring cations, creating an ITE state. The ITE state has a large configurational shift from the $5d$ state. When the ITE recombines, the configurational shift causes the energy shift in the emission. The configurational shift also causes a large change in bond length which is associated with the broad emission band.

The explanation of "anomalous" emission with an ITE model was first made for alkaline earth fluoride crystals doped with divalent ytterbium but "anomalous" emission occurs in many crystals doped with Eu^{2+} or Yb^{2+}. Dorenbos has gathered data on "anomalous" emission from over forty Eu^{2+} or Yb^{2+} doped crystal environments [9]. The position of the $5d$ levels relative to conduction band states and the presence of "anomalous" emission in these systems are related phenomena as the $5d$ state must be near enough to the

conduction band for an electron to become a delocalized ITE state. By quantifying the emission shift, Dorenbos found trends in the shift as a function of the size of the lanthanide ion and the sizes of the anions surrounding the lanthanide.

1.2.2 Impurity-Trapped Excitons in CaF_2:Yb^{2+}

Yb^{2+} ions in CaF_2 excited into the $4f^{13}5d$ configuration radiatively relax from an ITE state [6]. In CaF_2:Yb^{2+} ITEs have direct radiative recombination, giving broad emission with a large Stokes shift. The emission from the ITE in CaF_2:Yb^{2+} spans from 16 100 – 21 000 cm^{-1} and is shifted from the lowest $5d$ absorption by about 9000 cm^{-1} [28]. The emission deviates from the expected value (when compared to Eu^{2+} emission) by $\Delta D = -0.77$ eV (6200 cm^{-1}) [9].

The temperature dependence of the emission from the ITE in CaF_2:Yb^{2+} shown in Figure 1.4 is unusual. The intensity increases from 8 K to 110 K and then quenches by 180 K. When the emission peak position is measured, it shifts to higher energies up to 50 K and then shifts back to lower energy at higher temperatures.

Figure 1.4 The peak intensity of emission from CaF_2:Yb^{2+} varying with temperature after excitation into a Yb^{2+} $5d$ level at 28 200 cm^{-1} (355 nm) as measured by Moine et al.[26].

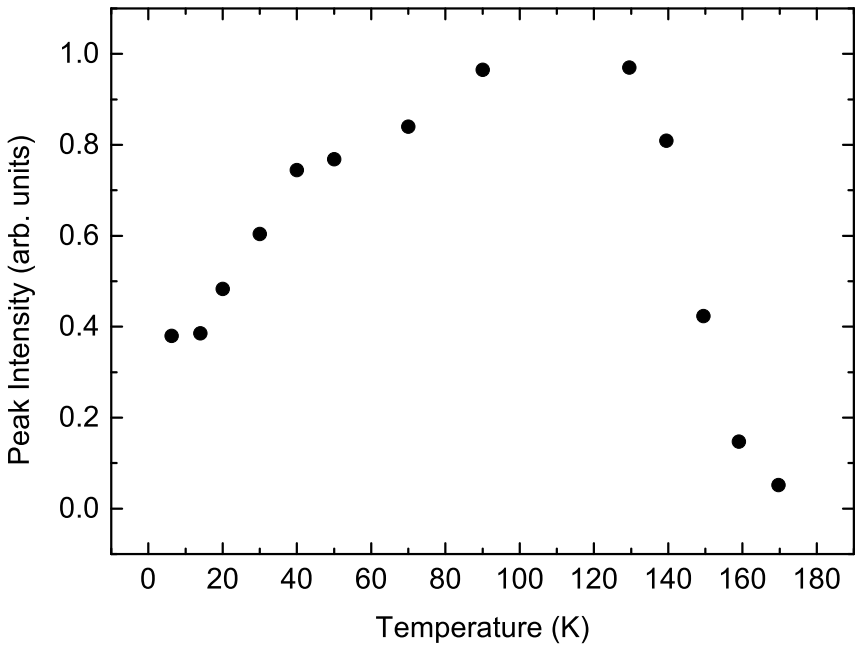

The temperature-dependent behaviour of the ITE emission was explained by Moine and

Pedrini [26, 27] with a model including two ITE states: an ITE ground state with a long radiative lifetime, and a higher energy state with a shorter radiative lifetime. At very low temperature all excited population is in the low energy state. The intensity of the emission initially rises with temperature, as the two states reach thermal equlilibrium. The temperature at which the intensity is at a maximum is related to the energy gap between the two ITE states. Once this equilibrium temperature is reached, the emission intensity falls with increased temperature, as it is thermally quenched. A configurational coordinate diagram of the two-level model is shown in Figure 1.5.

Figure 1.5 Configurational coordinate diagram of an ITE. ΔR is the ligand bond length. If the centre is excited into the $4f^{13}5d$ state near or in the conduction band (the shaded region of the Figure) it can relax into an ITE state where it will radiatively recombine. There are two ITE states, with similar energies but a large difference in configuration, causing very different emission frequencies. The two states are shown on the left. The higher-energy state has a higher emission rate than the lower-energy state.

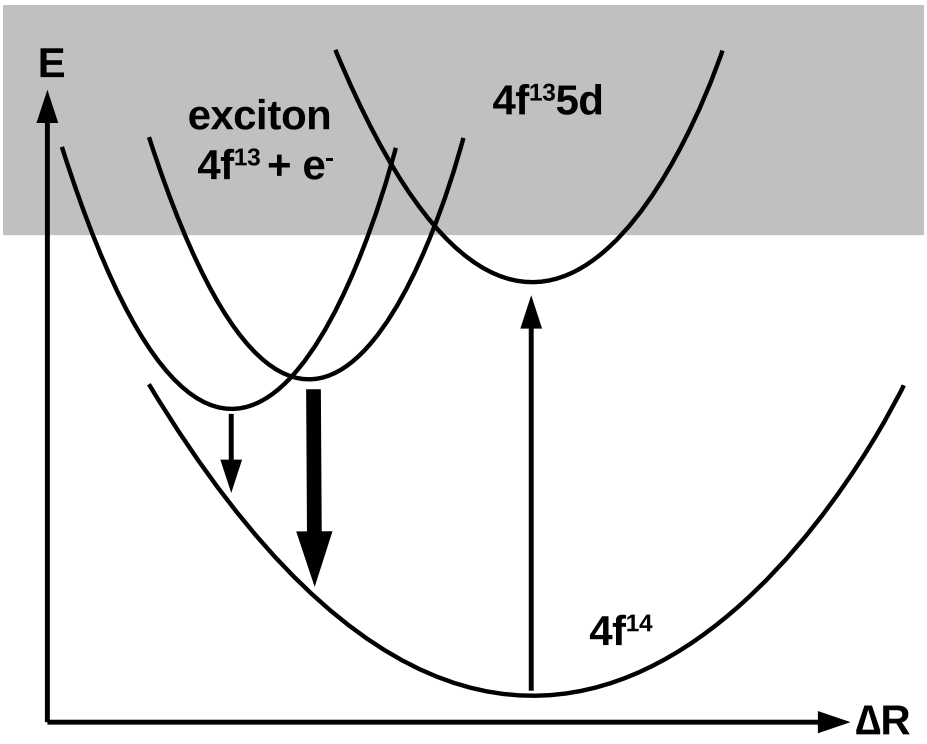

From the width of the emission, the bond-length change from the $4f^{14}$ ground state to the ITE ground state has been calculated to be 0.169 ± 0.002 Å and from the $4f^{14}$ ground state to the first excited ITE state is 0.154 ± 0.003 Å, so the first excited state has a bond length which is less contracted than the ITE ground state [28, 29].

1.2.3 Impurity-Trapped Excitons in $NaMgF_3$:Yb^{2+}

$NaMgF_3$:Yb^{2+} was one of the compounds identified by Dorenbos as "anomalous" [9]. It is specified as having a deviation from predicted normal Yb^{2+} emission of $\Delta D = -0.44$ eV (–3500 cm^{-1}) when compared to Eu^{2+} emission. Dorenbos states that "when ΔD is less than –0.1 eV (–800 cm^{-1}), conduction band states are likely to be involved in the emission," and the value for $NaMgF_3$:Yb^{2+} is well below this threshold value. The data on $NaMgF_3$:Yb^{2+} was recorded by Lizzo et al, [8] who commented that $NaMgF_3$:Yb^{2+} had wide emission bands and large Stokes shifts compared to $4f^n \rightarrow 4f^{n-1}5d^1$ transitions, suggesting the emission was from ITEs being formed around Yb^{2+} ions.

Lizzo also suggested the wide emission band and temperature-dependent band shape indicated there were two charge compensation centres present in $NaMgF_3$:Yb^{2+}. $NaMgF_3$ has an orthorhombically-distorted perovskite structure [30]. The Yb^{2+} replace Na^+ ions. It is likely that there are many charge-compensation centres for the Yb^{2+} ion, as multiple charge-compensation sites have been reported in $NaMgF_3$:Sm^{2+} [31] and $KMgF_3$:Eu^{2+} [32].

The presence of more than one charge compensation site in $NaMgF_3$:Yb^{2+} allows for the study of ITE formation in two impurity centres within the same crystal. Site-selective ITE spectroscopy where the two impurity centres can be distinguished by changing the monitored emission wavelength is the topic of Chapter 5 of this thesis.

1.2.4 Emission from MgF_2:Yb^{2+}

The emission from MgF_2:Yb^{2+} is a broad band extending from 17 000 to 25 000 cm^{-1}. Lizzo made high resolution measurements of the excitation spectrum and found four states from 22 920–23 560 cm^{-1}. Since the emission does not have a large Stokes shift from this fluoresence-detected absorption, Lizzo assigned the emission to a $4f^n \rightarrow 4f^{n-1}5d^1$ transition of the Yb^{2+} centres [8].

MgF_2:Yb^{2+} is different from CaF_2:Yb^{2+} and $NaMgF_3$:Yb^{2+} as the lowest component of the $4f^{13}5d^1$ excited state sits well below the conduction band. In 2003 Dorenbos [9] suggested the emission from MgF_2:Yb^{2+} deviated from where it would sit in comparison to MgF_2:Eu^{2+} emission by $\Delta D = -0.26$ eV (2100 cm^{-1}), so it was possible that the emission should be classified as "anomalous" and correspond to an ITE recombination. However, in 2012 Senanayake [33] failed to find any ITE states from two-colour experiments exciting

MgF_2:Yb^{2+} with UV and IR sources and concluded that the emission was indeed $4f^n \rightarrow 4f^{n-1}5d^1$.

1.3 Charge Transfer Transitions

A ligand-to-metal charge transfer transition is the transfer of an electron from the surrounding ligands to a central metal ion. It can also be described for a trivalent lanthanide (Ln) ion as the transfer of a hole from a Ln^{3+} ion to the surrounding ligands, causing the previously trivalent Ln ion to become divalent, and the hole to be trapped by the potential field caused by the effective negative charge of the Ln^{2+} ion. Lanthanide ions with high electron affinity have the lowest energy charge transfer transitions, such as Eu^{3+}, Yb^{3+} , Ce^{4+} and Tb^{4+} .

Absorption into charge transfer states has been observed across the lanthanide series, but emission from charge transfer states is quenched in many lanthanide ions [34]. In order for direct luminescence to occur from a charge transfer state, that state must sit at an energy lower than the $5d$ levels, but higher than the $4f$ states so that interstate crossing cannot occur. Charge transfer emission has only been reported for Yb^{3+} [35].

Impurity-trapped excitons could be created by a metal-to-cation charge transfer, where an electron is transferred from the Ln^{2+} ion to surrounding cations, creating an "Ln^{2+} + hole" centre.

1.4 Self-Trapped Excitons

Self-trapped excitons (STEs) are different to ITEs in that they are an intrinsic excitation of the crystal. An STE is an exciton in a transient lattice defect [10]. The study of STEs began with investigations of the darkening of alkali halide crystals when exposed to X-ray radiation in the 1940s and 50s. This colouration was determined to be from electrons trapped in ion vacancies called "F centres" [36], named for the German word "Fabre" meaning colour. Holes trapped around pairs of halogen ions were discovered around the same time and called "H centres" (i.e. halogen centres). In the 1960s, X-ray luminescence from alkali halide crystals was identified as the recombination of trapped holes and trapped electrons [37, 38]. These trapped excitons were indentified in alkali halides as precursors to lattice defects formed by ionizing radiation [39–41]. In the 1970s

STEs were also indentified in alkaline earth fluorides [42].

1.4.1 Structural Intrepretation of STEs

STEs are known to form in alkaline earth halides due to the ability of halide pairs to form covalent bonds and act as trapping centres [43]. To further discuss the structure of STEs, it is useful to define some terms used to describe crystal distortions.

A V_K centre is a hole trapped around a pair of halogen ions. The halogen pair contracts to about 30% of the normal lattice spacing to minimise the energy of the system. The interaction between the halogen ions give V_K centres a very characteristic electron paramagnetic resonance (EPR) signal associated with the hyperfine structure of the halogen pair. The halogen pair lie along the $\langle 100 \rangle$ axis as in Figure 1.6. H centres (sometimes called V_H centres) are V_K centres which have rotated so that one of the halogen ions fills an interstitial gap. H-centres have a similar EPR spectrum to V_K centres but the hyperfine lines are further split by interactions with surrounding halogen ions [44, 45].

Figure 1.6 Illustration of a V_K centre in CaF_2. The fluoride anions are labelled F and the calcium cation is labelled Ca. The position of the hole is indicated by the blue area.

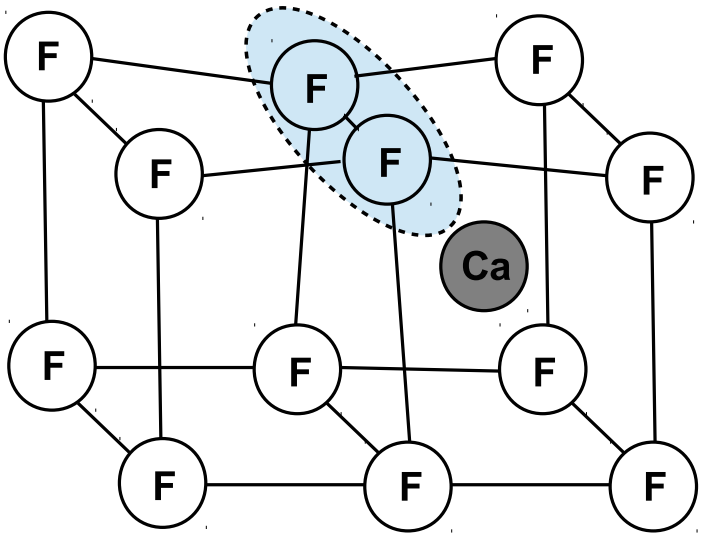

The self-trapped hole (STH) in CaF_2 has been shown to be a V_K centre comprised of two fluoride ions in several optical and EPR studies [43, 46]. When the STH captures an electron to become a STE, the fluoride ions which comprise the V_K centre rotate, and their

final position is along the ⟨111⟩ axis as an H centre. The rotation of one of the fluoride ions to an interstitial site leaves a vacant fluoride site, where the electron is localised, as in Figure 1.7, so the geometry of the STEs is that of an F-H centre pair. This geometery has been determined by optically detected EPR measurements and reinforced by *ab-initio* calculations [43, 47, 48].

Figure 1.7 Illustration of an H (or V_H) centre and a fluoride anion vacancy in CaF_2. The black circles are cations and the white circles are halogens. The position of the hole is indicated by the blue area.

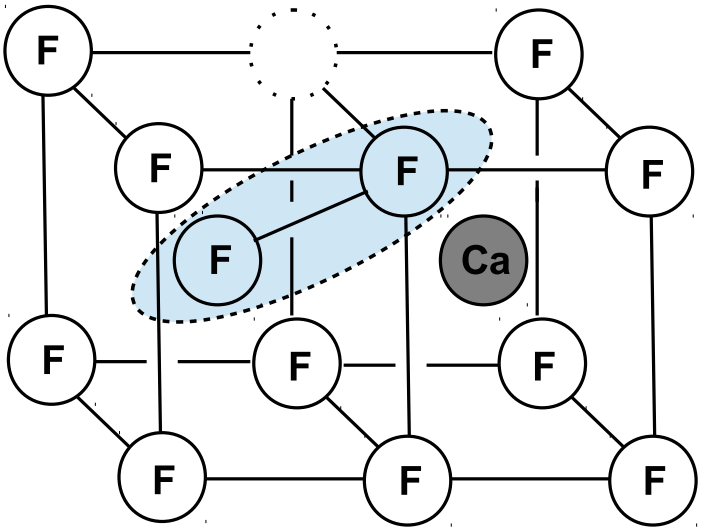

The STE in $NaMgF_3$ has not been studied in any detail, but we can assume that the results obtained for $KMgF_3$ will be relevant to $NaMgF_3$. $KMgF_3$ has been studied via EPR, *ab initio* method and an extended-ion method [49, 50]. The geometry of the STH in $KMgF_3$ is shown in figure 1.8. It is similar to CaF_2 as the STH is a V_K centre, but it is not aligned along the ⟨100⟩ axis. The fluoride pair rotates when it captures an electron.

The structure of the STE in MgF_2 has been theoretically proposed using an extended-ion model [51]. The STE configuration with the lowest calculated energy is an off-centre V_K centre as shown in Figure 1.9. This figure demonstrates the difference between a STE, where the electron and hole and bound to each other, and an F-H pair.

Figure 1.8 Schematic of the suggested geometry of the self-trapped hole in $KMgF_3$ [50]. The black circles are cations and the white circles are halogens. The position of the hole is indicated by the blue area.

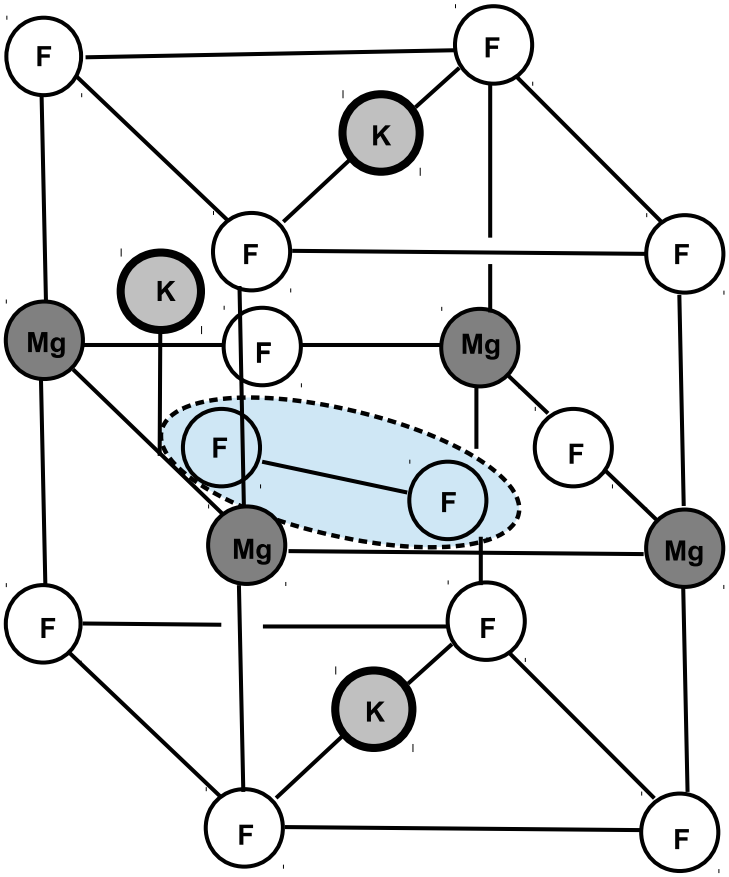

Figure 1.9 Schematic of (a) the suggested geometry of the STE in MgF_2. (b) the geometry of F-H pairs in MgF_2 [51]. The black circles are Mg^{2+} ions and the white circles are F^- ions. Specific fluoride ions are indicated by the labels 1, 2 and 3.

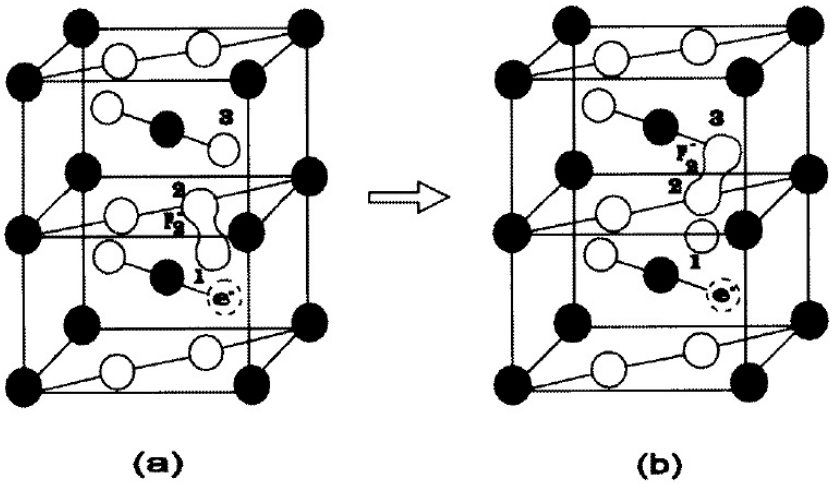

1.4.2 Recombination Luminescence

STEs are typically formed by above-bandgap excitation, which creates many free excitons. However, the amount of recombination luminescence from free excitons is very low. From the ratio of luminescence from free excitons to STEs, the lifetime of a free exciton before becoming self-trapped has been calculated to be on the order of picoseconds [52].

Recombination luminescence from STEs is usually in the form of a broad band with a Stokes shift of several electron volts. All STEs in alkali halides have an emission band with a characteristic polarisation, identified as the recombination of an STE state which is predominantly a triplet spin state [39]. In some cases emission attributed to recombination from a singlet state of the STE is also reported [53]. This singlet emission has distinct polarisation and a shorter radiative lifetime.

The recombination luminescence of STEs in alkali halides commonly quenches with temperature, which has been suggested to be because of the thermal increase of non-radiative transitions near the crossing of the configurational coordinate curves of the STE state to the system ground state shown in Figure 1.10 [54].

The STE in CaF_2 has a singlet and a triplet state which have overlapping emission bands with very different lifetimes. The lifetime of the singlet state is $\tau \approx 10$ ns and the triplet

Figure 1.10 A schematic representation of the states involved in recombination luminescence of STEs in alkali halides from Pooley and Runciman, 1970 [54].

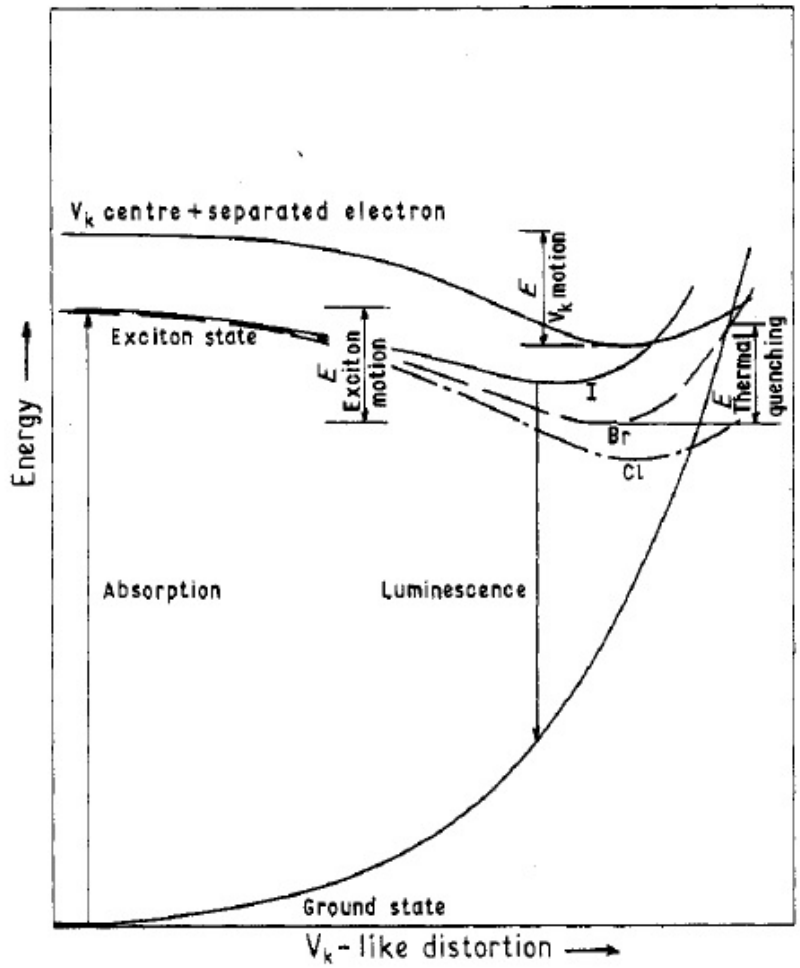

state is $\tau \approx 10$ μs [55].

Kristianpoller et al. identified emission from various defect states in irradiated $NaMgF_3$, but did not report STE emission. Triplet emission from $NaMgF_3$ STEs was identified in 2004 [56]. No singlet emission has been measured yet.

In 1977 Williams et al.measured broad band emission at 25 800 cm^{-1} in MgF_2 and identified that it was likely to be STE triplet emission [57]. The relationship between the dissipation of energy through creation of STEs compared to creation of Frenkel pairs has been the subject of MgF_2 studies, both spectroscopic [58] and theoretical [51, 59]. An extended emission spectrum by Kolobanov et al. [60] found an emission band at 67 800 cm^{-1} with a lifetime of 1.6 ns. This band was attributed to the singlet emission of the STE in MgF_2.

1.5 Outline

This work advances previous studies done on ITEs in insulating materials by measuring the dynamic behaviour of the ITE emission using a two-colour experiment in $NaMgF_3$. Previous work has been limited to UV excitation. The use of tunable-frequency IR excitation from an FEL enables intra-excitonic excitations to be performed.

STEs in alkaline earth fluorides have been investigated with X-ray spectroscopy, but limited VUV spectroscopy has been performed. VUV excitation allows for resonant absorption into intrinsic exciton states. By using a high-power VUV synchrotron source, this thesis presents clear emission from STEs over a range of excitation energies that gives new insight into energy transfer mechanisms between intrinsic excitations and ITE states in insulating materials.

The effect of confinement on STEs is studied by performing VUV spectroscopy on 2-dimensional CdF_2-CaF_2 superlattice materials.

This thesis contains the following chapters which examine the excitons that form in alkaline earth fluoride crystals:

- Chapter 2 is a review of the current knowledge relevant to the topics in this thesis. Semi-empirical crystal field modeling is introduced. The parts of the effective Hamiltonian are described and the crystal field parameters are given physical intepretation. Rate equation modelling of two-level systems is explained.

- Chapter 3 describes the experimental techniques used in this thesis. These techniques are: crystal growth, characterisation of materials using emisssion and absorption measurements, X-ray Absorption Near Edge Structure (XANES) measurements, two-colour photoluminescence enhancement, VUV measurements and two-colour excitation experiments using a Free-Electron Laser (FEL).

- Chapter 4 presents basic spectroscopic measurements of the materials used in this thesis, CaF_2:Yb^{2+}, $NaMgF_3$:Yb^{2+} and MgF_2:Yb^{2+} including emission and absorption spectra. The chapter also gives the valency distribution of the doped Yb^{2+} in CaF_2 and $NaMgF_3$ using the X-ray Absorption Near Edge Structure (XANES) measurement results.

- In Chapter 5 the details of impurity-trapped excitons which form from exciting Yb^{2+} in $NaMgF_3$ are examined using a two-colour technique called site-selective transient photoluminesence enhancement (SSTPE). The ITE states are investigated by varying experimental parameters such as temperature and excitation power. A system of rate equations is used to model the excited states of the ITEs.

- In Chapter 6 the relationship between the Yb^{2+} ITEs and intrinsic excitations in the host crystal is investigated with vacuum ultraviolet spectroscopy. VUV radiation excites into the band edge of these insulating materials, creating intrinsic excitons and e-h pairs. Spectra for CaF_2, $NaMgF_3$ and MgF_2 are all presented and compared to understand the energy transfer mechanisms between the host excitations and lanthanide impurity centres.

- In Chapter 7 the effect of confinement on self-trapped excitons in CdF_2 is explored. VUV spectra of CdF_2–CaF_2 superlattices are compared to bulk crystal measurements.

Chapter 2

Theoretical Background

In this chapter, the theory of $4f^n$ and $4f^{n-1}5d^1$ energy levels in lanthanide ions is presented. Semi-empirical crystal field modeling is introduced. The parts of the effective Hamiltonian are described and the crystal field parameters are given physical intepretation. Rate equation modelling of three-level systems is explained.

2.1 Crystal Field Calculations

Modelling and predicting the energies of excited states of lanthanide ions is a difficult problem. The states of the ion are affected by interactions between electrons in the ion and the ion's crystal surroundings, and taking all these effects into account will create a Hamiltonian which is far too complex to analytically solve. Computational methods have been developed to numerically solve for the energy levels with *ab initio* calculations using modifications to the Hartree-Fock method [61, 62].

A commonly-used method to calculate energy levels is to fit experimental spectra to a parameterised model. This method has been used to extract and compare parameters across ranges of ions and crystal hosts [63–65]. In semi-empirical crystal field calculations we construct a parameterised Hamiltonian matrix and diagonalise it to find its eigenvalues. By choosing the correct parameterisation the parameters can represent physical interactions of the ion and environment.

Crude *ab initio* calculations of the energy levels of lanthanide in host materials have been performed using the superposition model, which is discussed in more detail later in this chapter. More recently, an *ab initio* method using model potentials has been developed to perform embedded-cluster calculations and simulate the $4f^{n-1}5d^1 \rightarrow 4f^n$ transitions of lanthanide ions in ionic crystals [66, 67]. These calculations do not provide information directly about the magnitudes of the physical interactions involved, and a

limitation of these *ab initio* calculations is that they cannot be used to find trends in the interactions across the lanthanide series which could be extrapolated to predict results for other lanthanide systems.

The semi-empirical parameterised model can be linked to *ab initio* calculations [68, 69] so these methods complement each other in developing a model of lanthanide transitions in host materials.

In this work, the parameterised model is used to fit $NaMgF_3Yb^{2+}$ and MgF_2:Yb^{2+} $4f^{n-1}5d^1 \rightarrow 4f^n$ transitions, and the semi-empirical Hamiltonian that forms the basis of this model is explained in this chapter.

2.1.1 Constructing an Effective Hamiltonian

The effective Hamiltonian is the sum of two main parts, as shown in Equation 2.1: a free-ion Hamiltonian and a crystal field Hamiltonian.

$$H_{\text{eff}} = H_{\text{FI}} + H_{\text{CF}}. \tag{2.1}$$

The Hamiltonian is created by calculating the reduced matrix elements and multiplying them by the parameters which correspond to various interactions of the ion.

This Hamiltonian is then diagonalised to obtain the crystal field splitting as a function of the crystal field parameters. The eigenfunction basis is truncated to only include relevant energy levels, which, for this work, are the Yb^{2+} $4f^{14}$ and $4f^{13}5d$ levels.

A simulated spectrum can be created using the crystal field splitting and the associated transition intensities from the parameterised Hamiltonian. Parameters in the Hamiltonian are chosen to give a simulated spectrum that best matches experimental results.

2.1.2 Central Field Approximation

We can choose any parameterisation for a Hamiltonian, but it is useful to relate the parameters to physical interactions of the ion. To have a physically relevant parameterisation we utilise the central field approximation. The central field approximation is the simplification that the combined electric fields of the nucleus and all other electrons acting on any one of the electrons in an atom is radial and the same for all the electrons in the

atom. That is, every electron sees an identical potential $U(r)$ that is only a function of its distance from the nucleus. This leads to solutions of the form:

$$\psi_{n\,l\,m_l\,m_s}(r,\theta,\phi) = \frac{R_{nl}(r)}{r} Y_{l\,m_l}(\theta\phi)\chi_{m_s}. \tag{2.2}$$

R_{nl} are radial wavefunctions, $Y_{l\,m_l}$ are spherical harmonics and χ_{m_s} are spin functions.

2.1.3 Free Ion Parameters

As well as the central field, there are non-spherical parts of the potential which we add to the Hamiltonian as parameters multiplied by reduced matrix elements. The non-spherical terms we must add to the central field Hamiltonian are the operators that correspond to the two-body interactions of the valence electrons. The energies are calculated with respect to the ground configuration so the central field term E_{avg} can be set to zero and an E_{avg} term is added to account for the energy difference between the $5d$ and $4f$ states. The form of the free ion Hamiltonian used for semi-empirical fitting in this thesis is:

$$H_{\text{FI}} = E_{\text{avg}} + H_{\text{Cou}} + H_{\text{SO}}. \tag{2.3}$$

The free ion Hamiltonian given in Equation 2.3 above can be described as the sum of several components: E_{avg} is the central field, H_{Cou} describes the non-spherical Coulomb interaction between electrons in the ion and H_{SO} describes the relativistic spin-orbit interaction of electrons.

$H_{\text{Cou}} = \frac{e^2}{r_{ij}} - U(r)$ and by expanding $1/r_{ij}$ into scalar products of spherical harmonics, H_{Cou} can be given the form of a sum of a number of radial parameters multiplied by tensor operators:

$$H_{\text{Cou}} = \sum_{k=0,2,4,6} f_k\, F^k + \sum_{k=2,4} f_k(fd)\, F^k(fd) + \sum_{k=1,3,5} g_k(fd)\, G^k(fd). \tag{2.4}$$

F^k are the Slater integrals for the radial part of the electrostatic interaction. Here the F^k are associated with the repulsion between electrons within the $4f^{13}$ configuration, whereas $F^k(fd)$ and $G^k(fd)$ describe the Coulomb interaction between the $5d^1$ electron and the $4f^{13}$ shell. F^k are the direct terms which represent the potential of an electron on another. G^k are the exchange interaction terms which depend on electron wavefunction

integral overlap. For $4f^{13} - 4f^{13}$ interactions, the direct and exchange operators effect the same matrix elements, so only one term is needed. For $4f^{14} - 5d^1$ interactions the terms are distinct.

H_{SO} is also the sum of parameters multiplied by tensor operators:

$$H_{\mathrm{SO}} = \zeta_{ff}\, A_{\mathrm{SO}}(ff) + \zeta_{\mathrm{dd}}\, A_{\mathrm{SO}}(dd). \tag{2.5}$$

ζ_{ff} and ζ_{dd} are associated with the spin-orbit interactions in the $4f^{13}$ and $5d^1$ states and $\mathrm{A_{SO}}$ are calculated from matrix elements of the tensor operator V^{11}.

2.1.4 Crystal Field Parameters

When a lanthanide ion is situated in an enviroment with an electrostatic potential, such as a dielectric crystal, the spherical symmetry is lowered to that of the site symmetry in the crystal and the free ion levels split under the influence of the field provided by the neighbouring ions. This is represented by a crystal field Hamiltonian which is the sum of one-electron crystal field interaction parameters multiplied by many electron spherical tensor operators [70]:

$$H_{\mathrm{CF}} = \sum_{k,q} B_q^k C_q^{(k)}. \tag{2.6}$$

The B_q^k are treated as parameters that quantify the strength of the field acting on the rare earth ion. The values of k and q are governed by the triangular rule for the addition of angular momentum which gives non zero matrix elements associated with k even values due to parity. The $C_q^{(k)}$ are the Racah spherical tensor operators and are related to the spherical harmonics $Y_{k,q}$ by

$$C_q^{(k)} = \sqrt{\frac{4\pi}{2k+1}} Y_{k,q}. \tag{2.7}$$

Possible k and q values which give non-zero matrix elements are determined by the symmetry of the crystal field. For $\mathrm{O_H}$ symmetry centre the crystal field interaction Hamiltonian is [71]:

$$H_{\mathrm{CF}} = B^4\left[C_0^{(4)} + \sqrt{\frac{5}{14}}\left(C_4^{(4)} + C_{-4}^{(4)}\right)\right] + B^6\left[C_0^{(6)} + \sqrt{\frac{7}{2}}\left(C_4^{(6)} + C_{-4}^{(6)}\right)\right]. \tag{2.8}$$

If the symmetry is lowered by a tetragonal distortion the O_H Hamiltonian is modified with the addition of a $B_0^2 C_0^{(2)}$ term.

2.1.5 Transition Intensity Calculations

Lanthanide ions interact with the electromagnetic field of an exciting light source most commonly via the possession of an electric dipole moment. The intensity of transitions between energy levels in an ion is calculated from the interaction of electric and magnetic dipole moments of the ion with electromagnetic radiation. This interaction is represented by the electric and magnetic dipole operators given in Equation 2.9 and Equation 2.10 [72].

$$-eD_q^{(1)} = -erC_q^{(1)}, \tag{2.9}$$

$$M_q^{(1)} = \frac{-e\hbar}{2mc}(L_q^{(1)} + 2S_q^{(1)}). \tag{2.10}$$

$C_q^{(1)}$ is the spherical tensor operator given in equation 2.7, e and m are the charge and mass of an electron, $L_q^{(1)}$ is the orbital angular momentum operator and $S_q^{(1)}$ is the spin angular momentum operator. The value of q represents the polarization of light and can have the values $q = 0$ or ± 1.

The electric dipole operator has an odd parity whereas the magnetic dipole operator has an even parity. The fluoride systems studied in this work are symmetric, so transitions within either the $4f$ or $5d$ states are nominally electric dipole forbidden due to the absence of odd-parity interaction with the crystal. Transitions between $4f$ and $5d$ states are not electric dipole forbidden, as for these transitions $\Delta L = \pm 1$, but they are magnetic dipole forbidden.

If we average over all polarizations, the line strength S for a transition from an initial state I to a final state F is given by:

$$\begin{aligned} S_{FI}^{\mathrm{ED}} &= \frac{1}{3}\sum_q \sum_i \sum_f e^2 |\langle Ff \mid D_q^{(1)} \mid Ii\rangle|^2, \\ S_{FI}^{\mathrm{MD}} &= \frac{1}{3}\sum_q \sum_i \sum_f |\langle Ff \mid M_q^{(1)} \mid Ii\rangle|^2, \\ S &= S^{\mathrm{ED}} + S^{\mathrm{MD}}. \end{aligned} \tag{2.11}$$

The line strength can be easily related to stardard measures of absorption intensity such as the oscillator strength.

The absorption bands of $4f^{n-1}5d^1 \rightarrow 4f^n$ transitions are broadened by multiple mechanisms. There is a fundamental line width due to Heisenberg's uncertainty principal, which results in homogenous broadening. There is also a large inhomogeneous broadening due the change in bond length between $4f$ and $5d$ configurations changing the vibrational state of the system.

To model the smaller homogenous broadening and create zero phonon lines, the line strengths S_i are first convolved with Lorentzian functions with some small width γ for each absorption line i:

$$I_{\mathrm{zpl}}(E) = \sum_i \frac{S_i\,\gamma_i}{2(E - E_{\mathrm{peak},i})^2 + (\frac{\gamma_i}{2})^2}. \tag{2.12}$$

The vibronic band is approximated by adding a parameter E_{offset} to the energies associated with the zero phonon lines, and then convolving them with Gaussian functions:

$$I_{\mathrm{vib}}(E) = \sum_i \frac{2\sqrt{\ln 2}\,I_i}{\sqrt{\pi}\,\Gamma_i} \exp\left(\frac{-4\ln 2(E - E_{\mathrm{offset}})^2}{(\Gamma_i)^2}\right), \tag{2.13}$$

where the width Γ depends on the bond length change associated with the transition. The true lineshape of the vibronic broadening is more accurately described by a Pekarian function [73], however the band is sufficiently broad that a Gaussian function is a fair approximation. The final intensity is the sum of the zero phonon lines and the shifted vibronic bands:

$$I(E) = I_{\mathrm{zpl}}(E) + I_{\mathrm{vib}}(E). \tag{2.14}$$

2.1.6 The Superposition Model

The superposition model is a phenomenological model to calculate the crystal field parameters associated with a rare-earth ion in a site of a given geometric configuration [70]. The model assumes that the total crystal field can be expressed as a sum of the contributions from the nearest neighbour ions.

The value of crystal field parameters B_q^k depend on the geometry of the ligands. To compare interactions between ligands and ions in different crystal fields, it is useful to have a set of parameters that are independent of ligand orientation and bond length. These are called the intrinsic parameters.

The intrinsic parameters $\bar{B}^k(R_0)$ represent the crystal field of a ligand if we rotated the ligand to be aligned along the Z axis and moved it to a distance R_0 from the ion. The intrinsic parameters are a measure of the crystal field which is independent from the site geometry, so they should be comparable for the same ions with the same type of ligands in sites with different crystal symmetries. The crystal field parameters B_q^k are related to the *intrinsic* crystal field parameters $\bar{B}^k(R_0)$ by

$$B_q^k = \Sigma_L \bar{B}^k(R_0)(-1)^q \, C_{-q}^k(\theta_L, \phi_L) \left(\frac{R_0}{R_L}\right)^{t_k}, \tag{2.15}$$

where Σ_L indicates a sum over all nearest neighbour ligands, $C_{-q}^k(\theta_L, \phi_L)$ is a spherical tensor operator and represents a rotation from the Z axis to the proper ligand position. $\left(\frac{R_0}{R_L}\right)^{t_k}$ is the distance-dependent term. t_k depends on the distance between the ion and ligands. The distance term would be the same as an electrostatic potential if we chose $t_k = k + 1$ but comparison with experimental crystal field parameters suggests the value of t_k is higher [62].

2.1.7 Modelling Excitons With Crystal Field Theory

Recently some attempts to model ITEs with *ab-initio* and crystal field analysis have been made. The ITE state can be added to the system as a $6s$ state [74] but the success of the modeling varies with the host material [75]. Other methods of gathering information about energy levels of ITEs are needed to provide additional information for development of *ab-initio* models. Hence the two-colour excitation technique described in chapter 5, which is analysed with the two-level model described below.

2.2 Rate Equations

The ITEs that form in CaF_2:Yb^{2+}, SrF_2:Yb^{2+} and $NaMgF_3$:Yb^{2+} emit from two levels with very similar energies and very different radiative rates. This section describes the behaviour of two such states. We will create a simple three-level "toy" model using rate equations to show how the population of these levels changes with time as they reach thermal equilibrium. Then we will add a time-dependent term to move population from the lower state to the higher one, which simulates IR excitation in a two-colour experiment.

We will create a model for three energy levels:

1 The ground state of the system.
2 An excited state with radiative rate A_{21}.
3 An excited state with a greater radiative rate $A_{31} > A_{21}$.

We can model the time evolution of the populations of these levels N_1, N_2 and N_3 with a system of rate equations, visualised in Figure 2.1:

$$\frac{dN_1}{dt} = A_{21}N_2 + A_{31}N_3, \tag{2.16}$$
$$\frac{dN_2}{dt} = -(A_{21} + W_{23})N_2 + W_{32}N_3, \tag{2.17}$$
$$\frac{dN_3}{dt} = W_{23}N_2 - (A_{31} + W_{32})N_3. \tag{2.18}$$

The parameters A_{21} and A_{31} are the radiative rates of the two excited states. A_{31} is much greater than A_{21}. W_{23} and W_{32} are the non-radiative rates between the excited states. They are related by the equation:

$$W_{23} = W_{32}\frac{g_3}{g_2}\exp\left(\frac{-\Delta E_{23}}{kT}\right), \tag{2.19}$$

where g_2 and g_3 are the degeneracies of levels 2 and 3, ΔE_{23} is the energy difference between the excited levels, k is the Boltzman constant, and T is the temperature.

Figure 2.2 shows the dynamic behaviour of the population in a pair of energy levels 40 cm^{-1} apart, when all the population is put initially into level 2. The parameters used in this model are in Table 2.1. Level 3 is thermally populated, and the ratio of population

Figure 2.1 Schematic showing the rates between energy levels in a simple 3-level model.

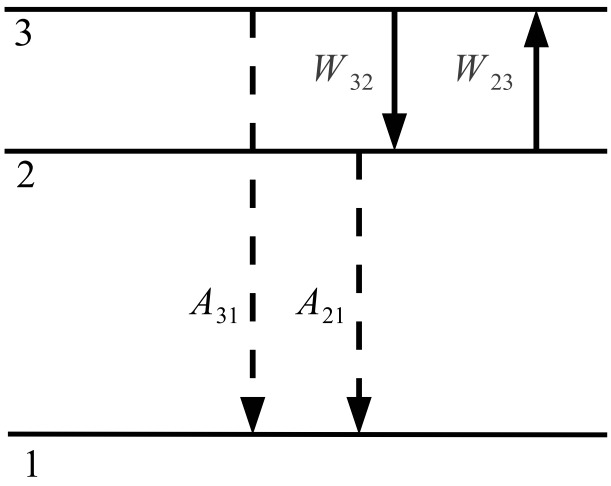

in level 3 compared to level 2 increases until thermal equilibrium is reached. At thermal equilibrium, the ratio of the population in level 3 compared to level 2 stabilises, which happens at around 20 μs in the figure. The population then radiatively decays from both levels into level 1. Since the radiative rate A_{31} is much greater than A_{21}, the transfer is mostly from level 3 to level 1, but population is then transferred non-radiatively from level 2 to level 3 to keep the ratio of the populations constant.

If the system is at a different temperature, the ratio between the populations in levels 2 and 3 will have a different equilibrium value. For example, if we take the same system as in Figure 2.2 and change the temperature from 300 K to 50 K, then as shown in Figure 2.3, the non-radiative rate from level 2 to 3 changes, and the equlibrium population distribution has more population in level 2 than at 300 K.

This decrease in population in level 2 compared to level 3 as temperature increases is shown in Figure 2.4(a). This figure shows the steady state populations, which are the eigensolutions of the system of ODEs in equations 2.16–2.18. The time the system takes to reach steady state depends on the value of W_{23}. In the example, the system reaches steady state by $\frac{1}{W_{23}} = \frac{1}{10^5\,\mathrm{s}^{-1}} = 10$ ms. We use the populations to calculate the radiative intensities of the two levels, as:

Figure 2.2 Demonstration of thermal equilibrium between three energy levels at a temperature of 300 K.

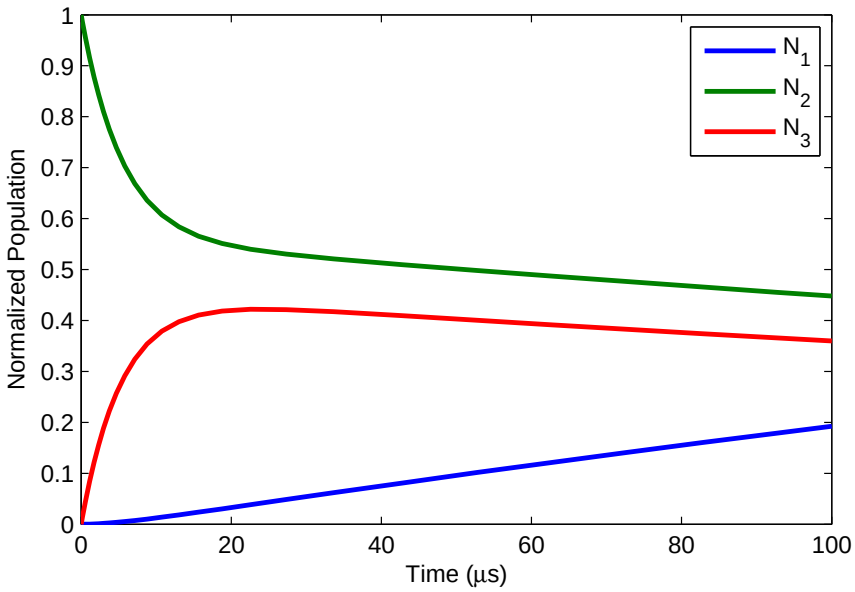

Table 2.1 Parameter values for the toy model. These parameters are used to show the general behaviour of two energy levels which are very close together. The parameters are used in equations 2.16–2.18 to calculate the populations in Figures 2.3–2.4.

Parameter	Value
A_{21} (s^{-1})	50 (20 ms)
A_{31} (s^{-1})	5000 (200 μs)
ΔE_{23} (cm^{-1})	40
g_2	1
g_3	1
W_{32} (s^{-1})	1.0×10^5

Figure 2.3 Demonstration of thermal equilibrium between three energy levels at a temperature of 50 K.

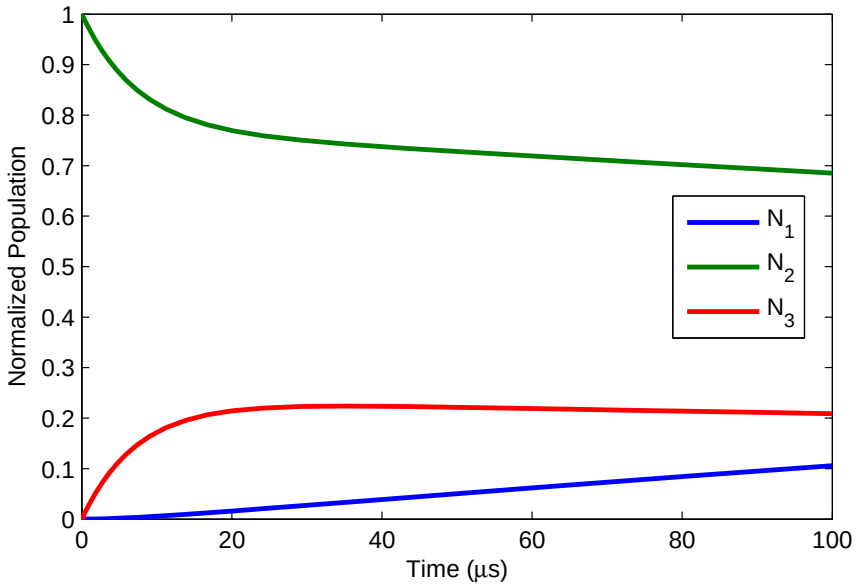

Figure 2.4 (a) Normalised equilibrium population distribution between three energy levels as temperature changes, (b) intensity of radiative transistions from the two energy levels as temperature changes.

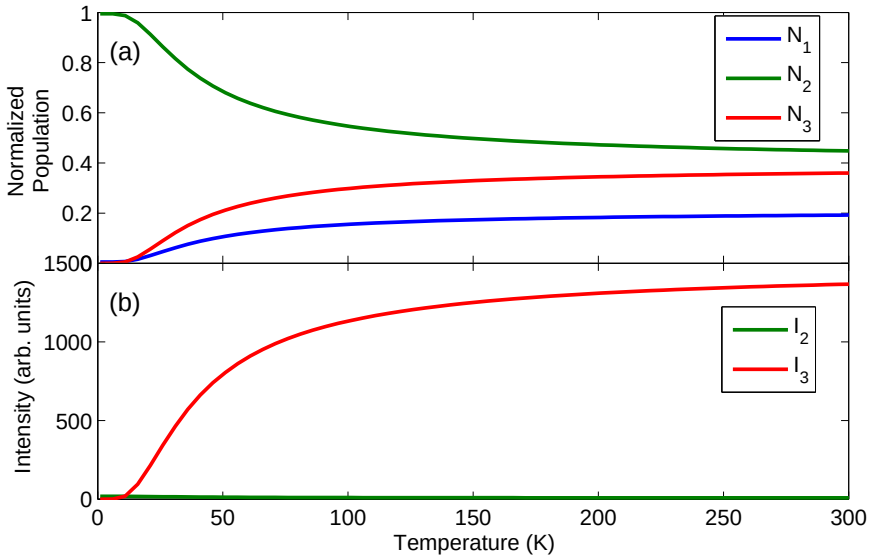

$$I_2 = A_{21}\, N_2, \tag{2.20}$$

$$\text{and } I_3 = A_{31}\, N_3. \tag{2.21}$$

Figure 2.4(b) shows if the system has population in the lower state and the temperature is increased, population is thermally excited into the higher level, which has a higher radiative rate, so the intensity of emission from the system increases.

The two-colour experiments described in Chapter 5 involve an IR excitation redistributing population from level 2 into level 3. In order to model this process, we can include a term P_{23}. The magnitude of P_{23} is time-dependent, and follows the shape of the IR pulse (shown in Figure 2.5). The new system of equations is:

$$\frac{dN_1}{dt} = A_{21}N_2 + A_{31}N_3, \tag{2.22}$$

$$\frac{dN_2}{dt} = -\left(A_{21} + W_{23} + P_{23}\right)N_2 + W_{32}N_3, \tag{2.23}$$

$$\frac{dN_3}{dt} = \left(W_{23} + P_{23}\right)N_2 - \left(A_{31} + W_{32}\right)N_3. \tag{2.24}$$

The enhancement in the transient in Figure 2.6 is the result of plotting the intensity calculated from Equations 2.22–2.24 using the parameters given in Table 2.1 and $P_{23} = 10^6$ s^{-1}. The value of P_{23} changes the height of the enhancement and the non-radiative rate changes the shape of the decay after the enhancement.

Figure 2.5 Shape of IR excitation pulse, which is used to model promotion of population from the second to third energy level.

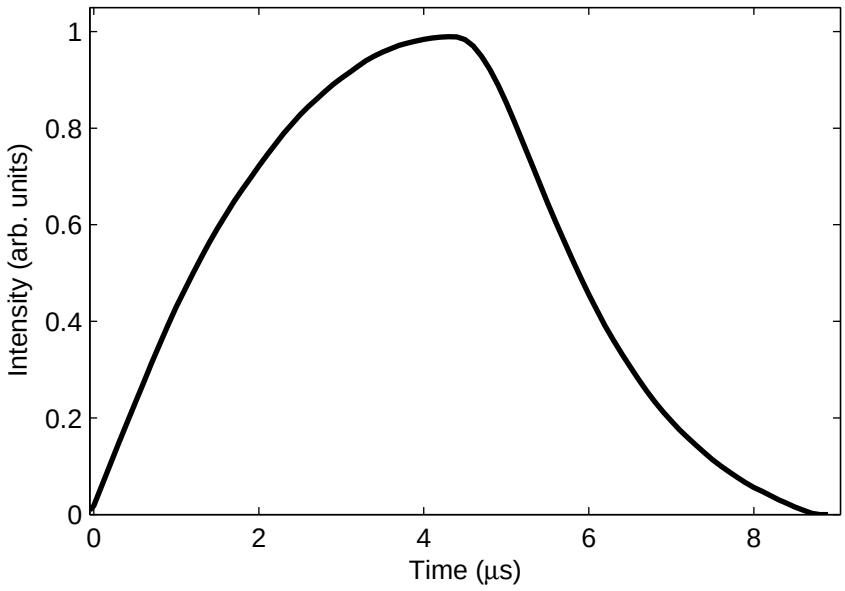

Figure 2.6 Modelled transients with the IR excitation, changing the non-radiative rate between levels 2 and 3 at 50 K.

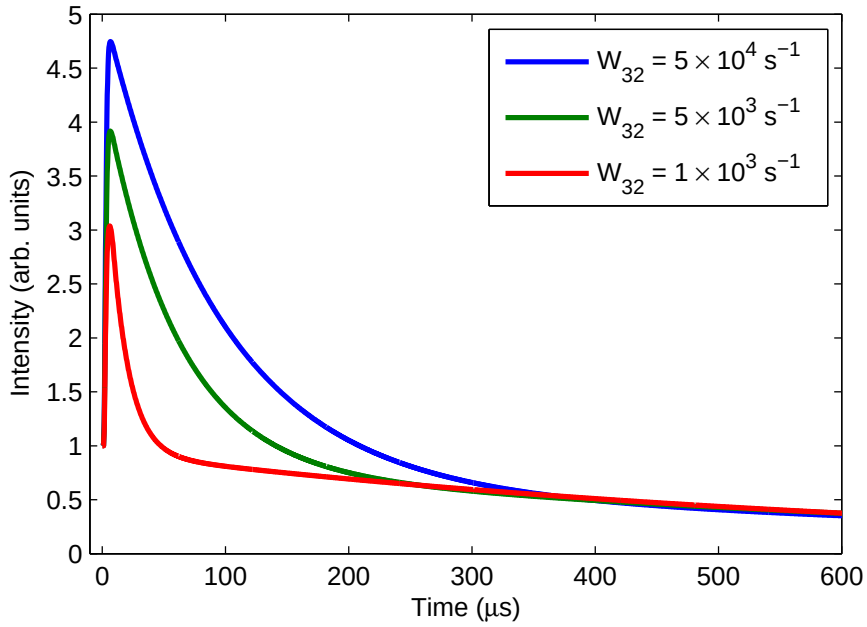

Chapter 3

Experimental Methods

This chapter describes the experimental techniques used to investigate the physics of Yb-doped alkaline earth fluoride crystals, and details the specific methodologies used to gather the data in this thesis.

3.1 Sample Growth

3.1.1 Bulk Crystals

The CaF_2:Yb and SrF_2:Yb crystals were grown by the author at the University of Canterbury, using the vertical Bridgman-Stockbarger technique in a 40 kW Arthur J. Little radio frequency (RF) furnace. Crushed pure metal fluoride crystal and 4N purity (ie impurities made up less than 10^{-4} percent) ytterbium fluoride powder were packed in a graphite crucible and placed within an insulated coil carrying RF current, located in a chamber capable of attaining a vacuum of around 3×10^{-5} mbar. Increasing the power output of the amplification system increased the electric field across the carbon crucible, which heated to the melting point of the mixture it contained. The dopant atoms were mixed evenly throughout the molten mixture by convection. The crucible was then slowly lowered out of the coil, causing the temperature to drop as it exited the RF field and the molten mixture crystallized [29].

The crystals were cut into samples with a thickness of approximately 2 mm with the use of a Struers Minitom diamond saw. The cut samples were then polished down to approximately 1 – 1.5 mm using a Struers LaboPol 2 polisher, initially employing progressively finer grades of Silicon Carbide (SiC) paper and subsequently diamond suspension activated fiber with progressively finer particulate sizes.

The calcium, strontium and ytterbium fluorides have melting temperatures of 1415, 1473

and 1052 °C, respectively. The CaF_2 crystals were typically grown at a RF output power of 9.9 kW, to achieve a nominal temperature of 1415 °C across the carbon crucible. The SrF_2 crystals were typically grown at a RF output power of 10.6 kW, to achieve a nominal temperature of 1473 °C.

Samples at dopant molar concentrations of 0.05% and 0.5% were grown. Growing crystals with greater amounts of YbF_3 causes the chemical reduction to Yb^{2+} ions to be less efficient, so more Yb^{3+} ions form than Yb^{2+} in higher concentration crystals.

The $NaMgF_3$:Yb and MgF_2:Yb crystals were grown in Interfacultair Reactor Instituut (IRI) in Delft and given to the University of Canterbury by Prof. Andries Meijerink, Utrecht University. Single crystals were grown via the Bridgman method in a carbon crucible in a reducing atmosphere of 75% N,/25% H, using a Philips PH 1006/13 high-frequency furnace. The $NaMgF_3$ mixture contained 0.5 mol % ytterbium. The actual amount of ytterbium in the crystals was determined by instrumental neutron activation analysis (INAA) to be 215 ppm [8]. For the MgF_2:Yb crystals, the starting materials used were MgF_2 (Highways Int., 4N) and YbF_3, which was prepared from Yb_20_3 (Highways Int., 5N). The crystal growth melt contained 0.6 mol% ytterbium [76].

3.1.2 Superlattices

CaF_2:Eu-CdF_2 superlattices (SLs) were grown at the Ioffe Institute, Russia by a molecular beam epitaxy (MBE) technique. Molten CaF_2:Eu and CdF_2 each in different effusion cells were alternatively deposited on a heated silicon substrate in an ultrahigh vacuum environment. The substrate was [111] oriented and its temperature was kept at 973 K. Several monolayers of CaF_2 were deposited on top of the Si substrate allowing subsequent coherent growth of CdF_2:Eu layers.

The overall thickness of the SLs is constant, and the number of monolayers indicates the thickness of each alternating layer. For the SL consisting of layers of five monolayer thickness (1 monolayer = 3.15 Å) of CaF_2:Eu and 5 monolayers of CdF_2, the number of alternating layers of material was about 30 [77].

3.2 Characterisation Measurements

Absorption was measured using a Cary 6000i Spectrophotometer. The sample was cooled with a Janis CCS-150 liquid helium cryostat system which was evacuated with a Pfieffer HiCube 80 Classic vacuum pump.

Photoluminescence was measured using a SpectraPhysics Cobra pulsed dye laser pumped with a Quanta-Ray pulsed ND:YAG with a repetition rate of 10 Hz. The dye used was Pyradine 2. The frequency of the laser output was doubled with a non-linear optical crystal to achieve an excitation range of 350-360 nm. The sample was kept at low temperatures with an Oxford Optistat CF2 system.

For the time-resolved measurements, the emission was collected with an Actor SpectraPro 2150i 0.150m imaging dual grating monochromator spectrograph and a PDA 100A EC silicon detector with a range of 340 nm–1100 nm. The transient was processed by a Tektronix TDS 2022 two-channel digital storage oscilliscope triggered off the laser pulse. For integrated measurements, the emission was dispersed by a Horba Jobin Yvon 1000M series II 1 m spectrometer and collected by a Hamamatsu C10372-02 photomultiplier tube with a range of 0-1500 nm.

The emission spectra presented in Chapter 4 were recorded at Victoria University using a Horiban Fluorolog with an iHR320 spectrometer using a 600 grooves/mm grating with a 1000 mm blaze angle and an electro-optical systems detector. The samples were excited with a xenon lamp. Spectra were corrected for lamp intensity and spectrometer sensitivity. The samples were cooled in a cryostat with liquid helium using a CTI helix 8001 compressor and the temperature was varied between 15 and 300 K using a Lakeshore 321 temperature controller.

The emission spectrum of SrF_2 was recorded at Dr.Guokui Lu's spectroscopy laboratory in Argonne National Laboratory with a Lambda Physik Scanmate YAG-dye combined system. The dye was Styryl 8 in ethanol. The power was 0.40mV at 375 nm. The sample was kept at low temperatures with an Oxford 43787 cryostat. The emission was collected with a Spex 1702/04 spectrometer and TSA 031034/467 photomultiplier tube.

3.3 XANES Fluorescence Measurements

X-ray Absorption Near Edge Structure (XANES) is a spectroscopic technique which is the X-ray equivalent to excitation measurements in optical spectroscopy [78]. The XANES measurements are scans over excitation energies around an absorption transition that excites a core electron into the conduction band, while monitoring the fluorescence intensity integrated over a specific band of X-ray energy. The excitation can be into any of the resonant transitions which will excite core electrons, but some transitions will be stronger than others due to dipole selection rules, $\Delta l = \pm 1, \Delta j = \pm 1, \Delta s = 0$. Similarly any resonant fluorescence transition can be monitored but practically only some transitions are strong enough to be measured. The resonant transitions are labelled based on the principal quantum numbers of the core state. The principal quantum numbers n=1, 2, and 3, correspond to the K, L, and M-edge respectively. Figure 3.1 is a schematic of the X-ray fluorescence process utilised for XANES measurements.

All XANES measurements in this thesis are of Yb. The Yb was excited into the L_3 edge at 8949 eV which corresponds to a transition from a $2p^{\frac{3}{2}}$ to the conduction band. The fluorescence transition that is monitored is the L_α emission line.

The XANES data were measured at the Pacific Northwest Consortium Collaborative Access Team (PNC-CAT) bending magnet beamline of the Advanced Photon Source (APS) in Argonne National Laboratory, Illinois [79]. The basic schematic of the X-ray beamline is shown in Figure 3.2. All energies of X-rays pass through an entrance slit, and the energy required is selected by a Si 111 double crystal monochromator. The incident intensity is measured before the beam hits the sample, using a 20 cm long parallel plate ionisation chamber filled with N_2 gas. The detector consists of parallel plates with a high voltage across them. Incident X-rays ionize the gas. The electron emitted from the ionised gas goes to one plate and the ion to the other, producing a current.

The X-ray fluorescence from the sample is measured with a mercury single element vortex system - a solid state X-ray detector which measures the energy of an incoming photon by the amount of ionization it produces in the high purity silicon detector. The optical fluorescence is measured with a CCD detector. The mercury single element vortex system has an unresponsive period or "dead time" after each signal event. The dead time depends on the total count rate and is corrected for using the incident intensity.

The 20-BM: Sector 20 bending magnet beamline used has an energy range of 2.7-32.7 keV and a flux of 1×10^{11} photons $s^{-1}/0.1\%$ BW at an energy of 10 keV. BW is the energy

Figure 3.1 Illustration of an X-ray fluorescence process: An incoming X-ray photoionizes an atom, leaving a hole in one of the core levels. The hole recombines with an electron from a higher core level, and an X-ray is emitted.

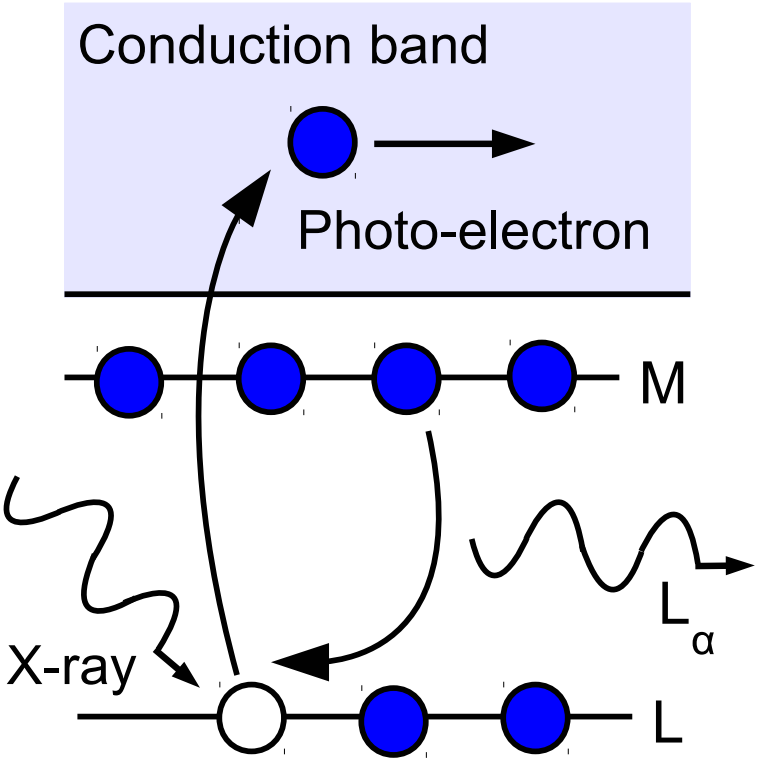

Figure 3.2 Illustration of the X-ray fluorescence measurement setup at 20-BM.

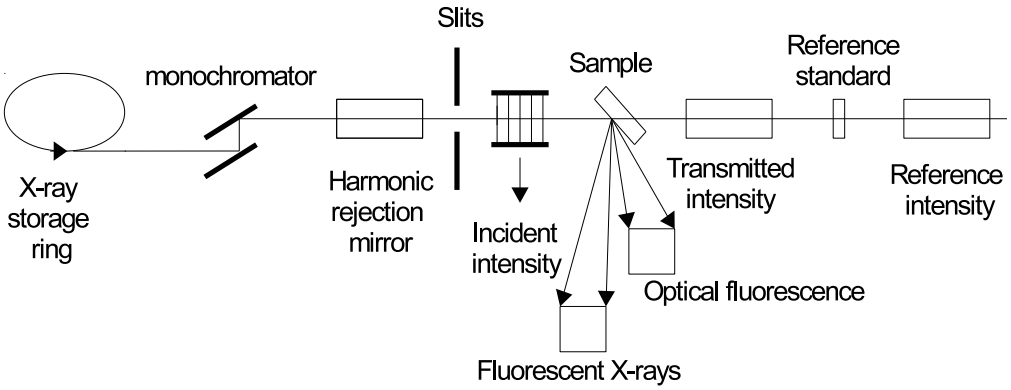

bandwidth of the monochromator. The monochromator is Si 111 and has a resolution of 0.14 eV at 10 keV and is shown in Figure 3.3. The unfocused beam size is 30 mm×1 mm. The beam is focused with a toroidal mirror and the focused beam size is 500 μm × 250 μm. Cold temperatures are achieved with a nitrogen microfridge capable of temperatures between 100-300 K. The setup in the experimental hutch is shown in Figure 3.4.

Figure 3.3 The Si 111 double crystal monochromator that selects the X-ray energy before the X-ray beam enters the experimental hutch.

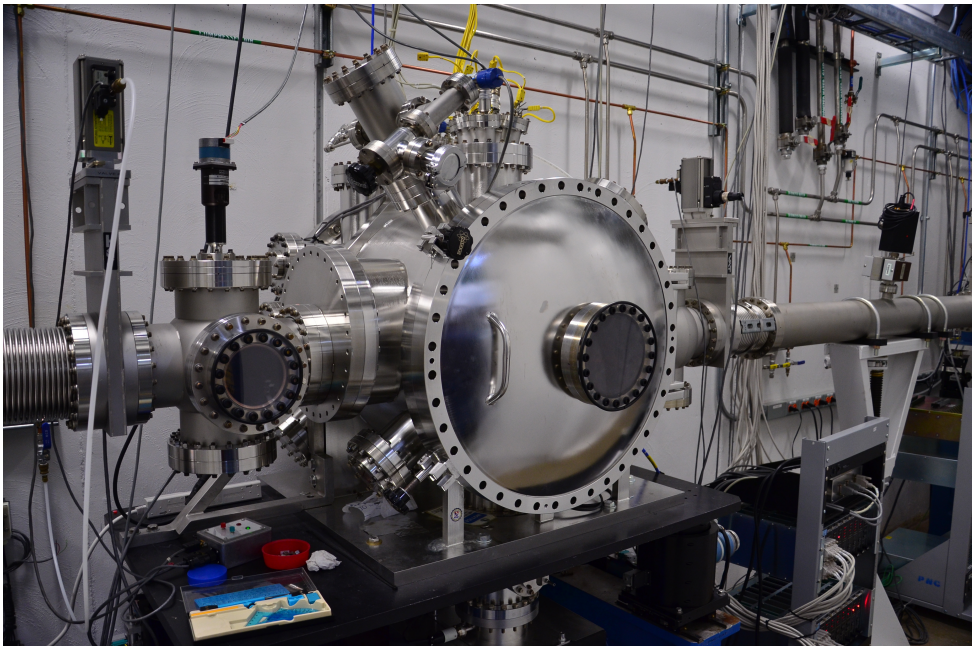

3.4 Site-Selective Two-Colour Photoluminescence Enhancement

The two-colour experimental technique described here was developed by Senanayake [29] and applied to the CaF_2:Yb^{2+} system to probe excitonic energy levels. Similar experiments are utilised in this thesis to probe the ITE in $NaMgF_3$:Yb^{2+} with the addition of site-selective spectroscopy to differentiate between the two emitting ITE centres present in $NaMgF_3$:Yb^{2+}.

A schematic of the Site-Selective Two-Colour Photoluminescence Enhancement (SSTPE) method is shown in Figure 3.5. A UV pulse delocalises the outer valency electron of the Yb^{2+} which forms an ITE in its ground state. Population in the ITE begins to slowly decay to the $4f^{14}$ configuration with a lifetime of several milliseconds. After the UV pulse, an IR pulse excites the ITE population into a higher-energy ITE state. The oscillators in the higher energy state decay non-radiatively to a faster emitting state, where they decay

Figure 3.4 The experimental hutch for 20-BM, the bending magnet beamline at APS used for XANES measurements.

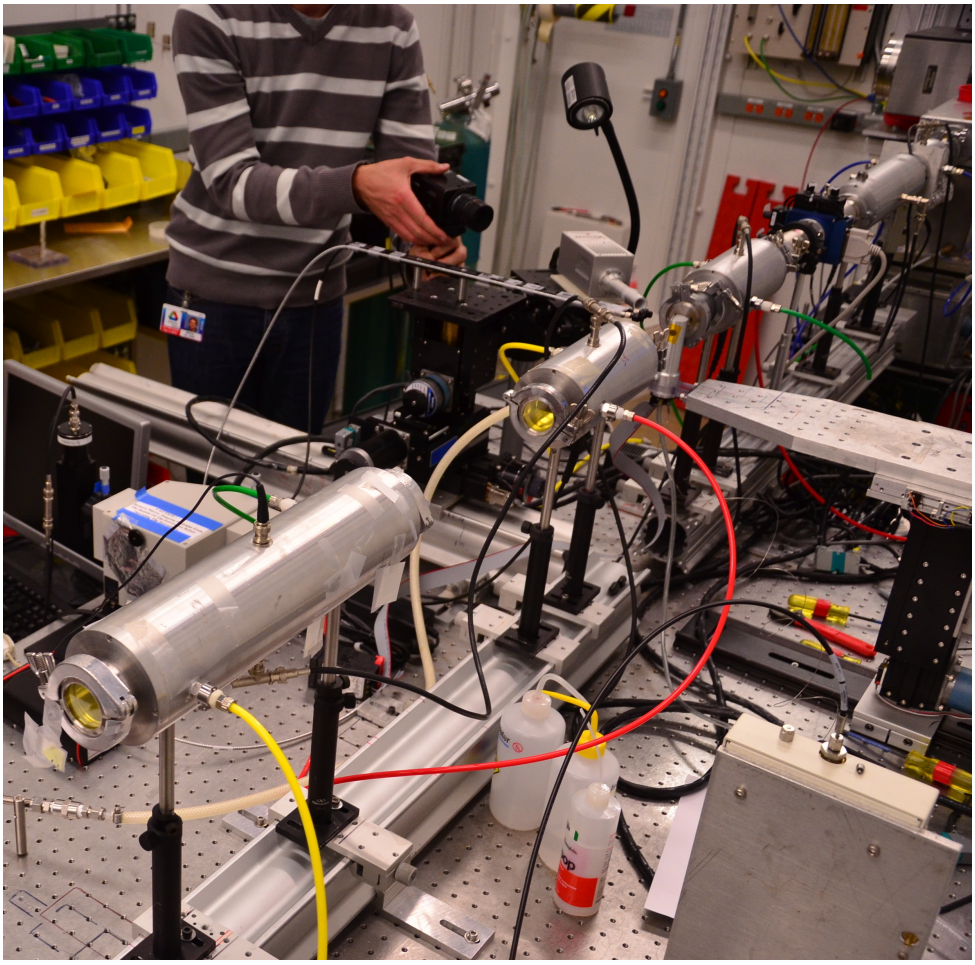

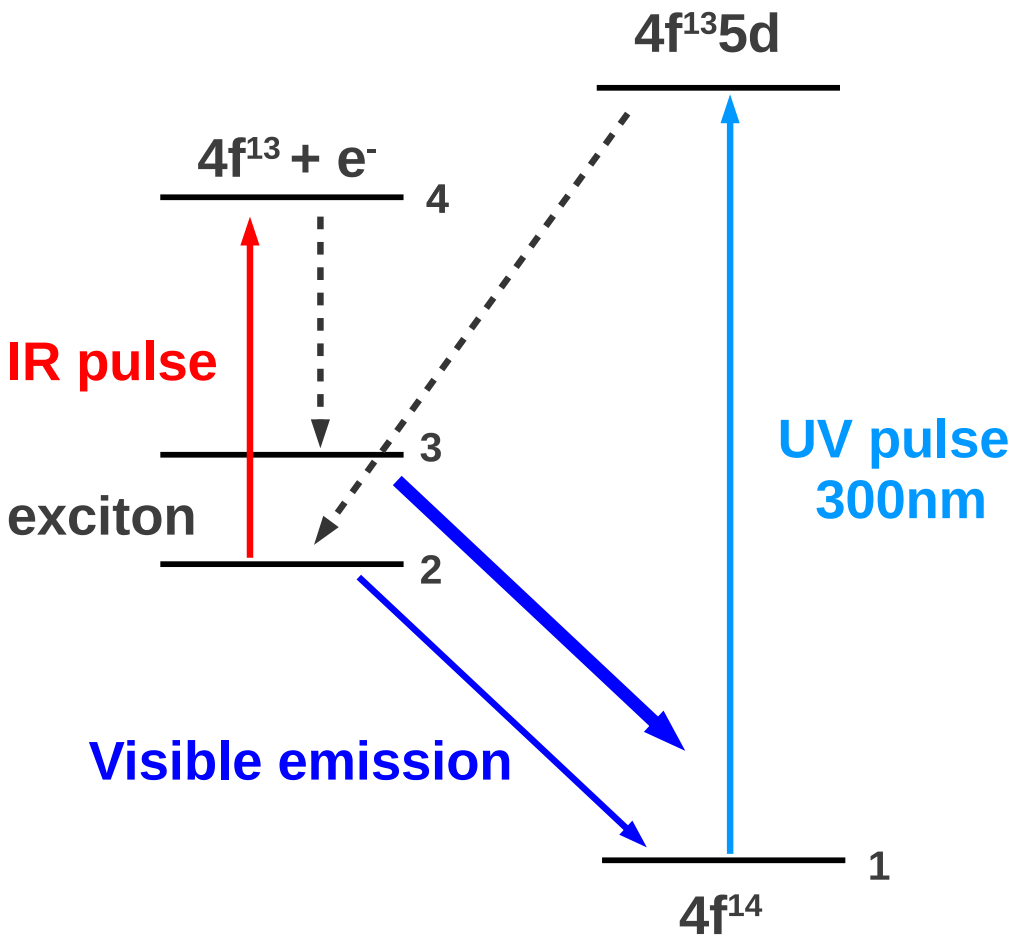

Figure 3.5 A schematic of the SSTPE method. UV excitation promotes Yb^{2+} ions from the Yb^{2+} ground state to a higher Yb^{2+} state from which they relax non-radiatively into the exciton ground state. There are two primary emitting exciton levels, the ground exciton state and a higher-energy exciton state. The higher-energy exciton state has a larger radiative rate. The IR pulse promotes excitons from their excitonic ground state into higher exciton energy levels, whereby they radiatively relax to the Yb^{2+} ground state.

to the $4f^{14}$ configuration with a lifetime of hundreds of microseconds.

The UV excitation source was a Ti-Sapphire RegA regenerative amplifier seeded by a MIRA 900F Ti-Sapphire oscillator, that pumped a Quantronix TOPAS Optical Parametric Amplifier (OPA) which provided tunable UV laser radiation output from 250 to 400 nm. The pulse width of the OPA was typically 3 ps with a repetition rate of 1 kHz. The average power output at the laser was 10 – 15 mW, with a maximum pulse fluence of approximately 0.13 Jcm^{-2}.

The infrared (IR) radiation was provided by the Dutch Free Electron Laser for Infrared eXperiments (FELIX), located at FOM Rijnhuizen in Nieuwegein, the Netherlands. FELIX has a tunable wavelength range from 3 –250 μm, and is able to be scanned continuously for over an octave. It is a pulsed laser, consisting of a macropulse with a width of 4–10 μs with a repetition rate of 5 or 10 Hz. For the experiments presented in this thesis the 10 Hz repetition rate was utilized. The macro-pulse contains a series of micro-pulses of variable width (0.3 to 10 ps) with a repetition rate of either 25 MHz or 1 GHz [80]. In this work, the rate was 25 MHz and the fact the pulse is constructed from a series of micro-pulses had no effect on the measurements.

FELIX has two beam lines, FEL2 and FEL1. The beam lines have different wavelength ranges. FEL2 allows for IR wavelengths between 3 – 45 μm, and can be set up to have a flat power output over a relatively large scan range, especially from 10 μm onward. FEL1 ranges from 45 – 250 μm but the power fluctuations are much greater at longer wavelengths. The experiments in this thesis use the FEL2 beamline.

The UV and IR beams were focused and spatially overlapped on the sample using a pinhole with a maximum diameter of 100 μm. A delay was introduced between the UV and IR pulses, with the UV arriving at the sample at 100 μs prior to the IR. The UV was focused using standard optical lenses. Due to the long wavelength of the IR beam, gold-plated off-axis parabolic mirrors were used for focussing.

The samples were cooled with liquid helium inside an Oxford Instruments Microstat, operating under a vacuum of 10^{-6} mbar. Stable temperature control from 8 K to room temperature was achieved using the variability of helium flow rate and a heating unit attached to the microstat. Either a CaF_2 or BaF_2 window was used for the front window of the microstat as to be transparent to the UV excitation and near IR emission from the sample. The rear window was required to be transparent to the IR excitation so a BaF_2, ZnSe or polythene window was used, depending on the range of the IR wavelengths it

needed to transmit.

The emitted light was detected with a TRIAX 320 spectrometer with a focal length of 320 mm and a C31034 photo multiplier tube (PMT), run at a voltage of 2000 to 1600 V. The signal from the PMT was passed through a Stanford Instruments SR 570 current amplifier to an oscilloscope where the data was captured via a GPIB interface, using LabView. UV laser scatter was blocked with long-pass optical filters placed in front of the input slit of the spectrometer. The slit width of the TRIAX was set to 1 mm giving the spectra a maximum resolution of 2.6 nm. Band pass filters were placed between the IR entry point into the experimental station and the sample to avoid higher harmonics of FELIX leaking through onto the PMT.

The data acquisition recorded the transient response of the sample to the two pulses. The maximum time span of a single transient was limited by the repetition rate of the UV pulse to 1 ms. FELIX was operated under a 10 Hz repetition rate, and by triggering the data acquisition hardware with the FELIX pulse it was possible to exclude the UV pulses which did not have an IR pulse following them.

Power and temperature dependent responses of the transients were recorded. Power was varied by using filters to attenuate the beam. Temperature was varied by using the PID-controlled cryostat heaters and manually controlling the helium gas flow.

3.5 Vacuum Ultraviolet Spectroscopy

The vacuum ultraviolet (VUV) is the region of the electromagnetic spectrum above ultraviolet but not so energetic as to be ionizing radiation. The term “vacuum” is used because photons with energies in the VUV range are strongly absorbed by atmospheric oxygen, so VUV spectroscopy measurements must be conducted in a vacuum. The region begins at 6 eV and extends to extreme UV at around 15 eV.

The VUV energy range is suitable for probing the conduction band edge of fluoride materials [19]. A tunable VUV excitation source enables excitation specifically just below and above the conduction band of the host material which gives more information about the connection between ITEs, STEs and the conduction band.

The VUV measurements were taken with the SUPERLUMI station at Hamburger Synchrotronstrahlungslabor (HASYLAB) in Hamburg, Germany. The excitation energy range of SUPERLUMI is 4 to 40 eV and the emission energies that can be detected

range from 1.2 to 25 eV. SUPERLUMI uses synchrotron radiation from the DORIS III storage ring. The interval between the bunches on the ring is 96 ns and each bunch has a FWHM of 130 ps [81, 82].

An illustration of the VUV spectroscopy setup is shown in Figure 3.6. The primary monochromator which selects the VUV energy is a 2 m unit in a McPherson mounting with a 1200 grooves per mm grating, giving a dispersion of 3.2 Å. The sample chamber is under ultra-high vacuum (approximately 10^{-9} mbar) to avoid oxygen and nitrogen absorption. The sample is held on a cold-finger within a cryostat and can be liquid helium cooled to 8 K. The cold-finger can hold many samples simultaneously. The luminescence is detected with a 0.3 m ARC SpectraPro-308i monochromator and a high-speed R3809U-50S (Hamamatsu) microchannel plate (MCP) detector. The time-integrated spectra were recorded by counting emission signal within the whole time period of 96 ns available between sychrotron pulses. The time-resolved spectra were recorded within two time gates (TGs): 2-9 ns (fast time gate) and 46-70 ns (slow time gate) relative to the beginning of the sychrotron pulse.

Figure 3.6 Schematic of the VUV fluorescence measurement setup at SUPERLUMI.

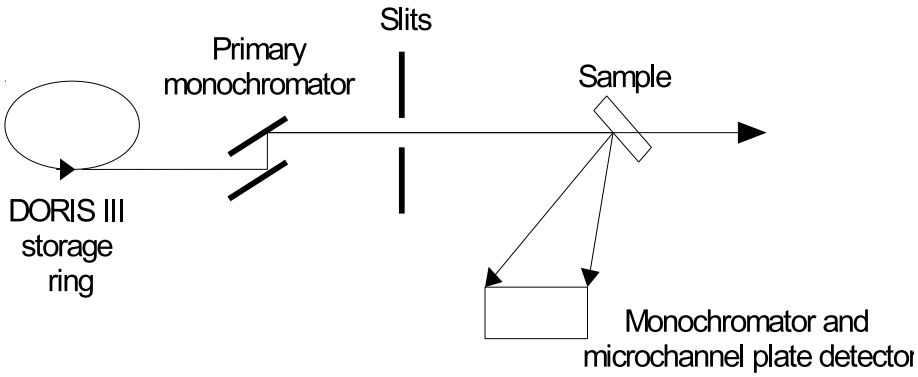

Chapter 4

Material Characterisation

This chapter presents some fundamental optical properties of the Yb-doped fluoride systems being studied in this thesis: SrF_2, CaF_2, MgF_2, and $NaMgF_3$. Their optical absorption and emission spectra are presented. The oxidation state of the Yb dopant is ascertained from XANES experiments. The measurements in this chapter give an understanding of the basic optical features of these fluoride systems.

4.1 Optical Absorption Measurements of Yb-doped CaF_2, SrF_2, and $NaMgF_3$

All absorption measurements were taken from 7000 cm^{-1} to 50 000 cm^{-1} and show transitions from the Yb^{2+} $4f^{14}$ ground state to the $4f^{13}5d^1$ excited configuration.

Figure 4.1(a) and (b) show the absorption spectra for Yb-doped SrF_2 and CaF_2 samples that are 1 mm thick. The spectra are very similar as the Yb^{2+} sites have the same symmetry in both hosts. There is a slight shift to higher energy for Yb^{2+} in SrF_2 because Sr^{2+} has a larger ionic radius than Ca^{2+}. The absorption peaks show the cubic field splitting into higher $4f^{13}5d(t_{2g})$ and lower $4f^{13}5d(e_g)$ states [26]. In cubic symmetry, the t_{2g} configuration has an electron distribution which is much closer to the ligands than the e_g configuration, so the t_{2g} states have a higher energy. Figure 4.1(a) shows the excitation spectrum for comparison: The higher energy peaks transfer energy into radiative ITE states much less efficiently than the peak at 27 000 cm^{-1}.

The excitation spectrum for Yb-doped MgF_2 and $NaMgF_3$ shown in Figures 4.1(c) and (d) are very different to CaF_2:Yb and SrF_2:Yb. The structures of MgF_2 and $NaMgF_3$ have a much lower symmetry than the cubic crystals [8, 76]. A lower symmetry site generally means more peaks will be observed in the excitation spectrum, as more transitions are allowed. The excitation spectra of MgF_2:Yb^{2+} and $NaMgF_3$:Yb^{2+} are extended to higher

energies and the peaks are analysed with a semi-empirical crystal field model in Chapter 6. The features in the excitation spectrum of $NaMgF_3$:Yb^{2+} depend on the emission energy which is monitored, because there are two sites which form ITEs in $NaMgF_3$:Yb^{2+}, and each has a different crystal field potential.

4.2 ITE Emission from Photoluminescence Measurements

Yb-doped CaF_2, SrF_2, MgF_2 and $NaMgF_3$ each display broad emission at significantly lower energy than the excitation frequency, as discussed in Chapter 2. Emission spectra of $5d$ Yb^{2+} states in these crystals are shown in Figure 4.2. The emission energies increase with decreasing lattice constants of the host crystals in Table 4.1.

Table 4.1 Lattice constants of fluoride crystals.

	a (Å)	c (Å)
SrF_2:Yb^{2+} [a]	5.79	
CaF_2:Yb^{2+} [b]	5.46	
MgF_2:Yb^{2+} [c]	4.64	3.02
$NaMgF_3$:Yb^{2+} [c]	3.87	

[a] Ref. [83] [b] Ref. [84]
[c] Ref. [85] [d] Ref. [86]

Figures 4.2(a) and (b) show the ITE emission from SrF_2:Yb^{2+} and CaF_2:Yb^{2+}. The shift of the peaks of both these crystals have been analysed by Moine et al. [26] along with temperature-dependent lifetime data. The initial intensity increase is caused by thermal excitation of a higher energy ITE level and the following emission quenching is due to the non-radiative decay of the ITE increasing with temperature.

The emission from MgF_2:Yb^{2+} shown in Figure 4.2(c) is half as wide as the other emission bands from Yb^{2+}-doped fluorides in the figure, and as discussed in section 1.2.4 of this thesis, this emission from MgF_2:Yb^{2+} is assigned to a Yb^{2+} $5d$ state rather than a multi-level ITE [33].

The emission from $NaMgF_3$:Yb^{2+} shown in Figure 4.2(d) has a similar temperature-dependent behaviour to CaF_2:Yb^{2+} but the emission quenches above 300 K for $NaMgF_3$:Yb^{2+} compared to 180 K for CaF_2:Yb^{2+} [8].

Figure 4.1 Excitation and absorption of fluoride crystals doped with Yb at a sample temperature of 10 K. The concentration of the Yb in the crystals are SrF_2:0.05%Yb, CaF_2:0.05%Yb, MgF_2:0.6%Yb and $NaMgF_3$:0.5%Yb. The peaks are associated with $4f^n \rightarrow 4f^{n-1}5d^1$ transitions of Yb^{2+}. Measurements are either absorption spectra, or excitation spectra labelled with the energy of the monitored emission.

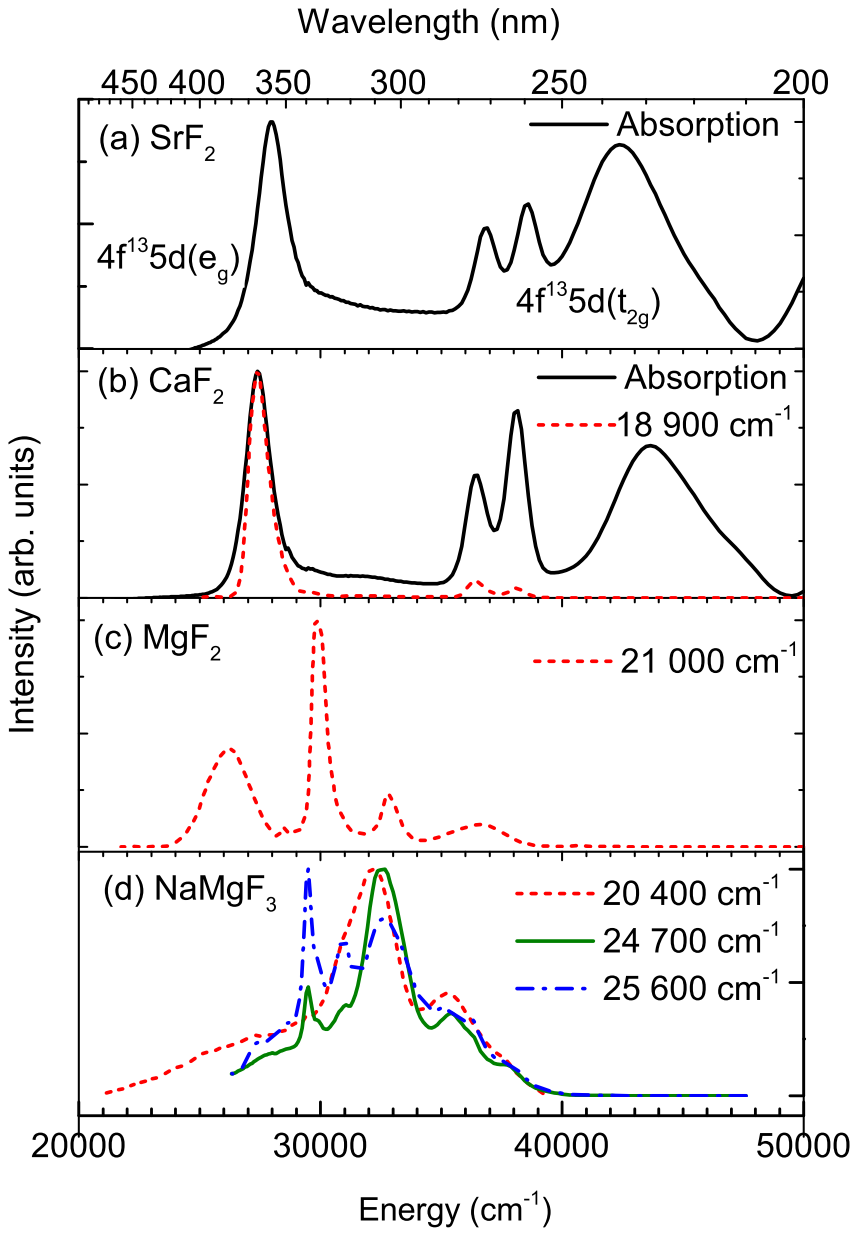

Figure 4.2 Emission of fluoride crystals doped with Yb excited into a Yb^{2+} $5d$ levels. The excitation energies are given in Table 4.2. The concentration of the Yb in the crystals are SrF_2:0.05%Yb, CaF_2:0.05%Yb, MgF_2:0.6%Yb and $NaMgF_3$:0.5%Yb. Measurements were made with a Horiban Fluorolog at a sample of temperature of 15 K as described in Chapter 3 except for (a) the SrF_2:Yb^{2+} emission, which was excited with a Lambda Physik Scanmate at a sample temperature of 10 K.

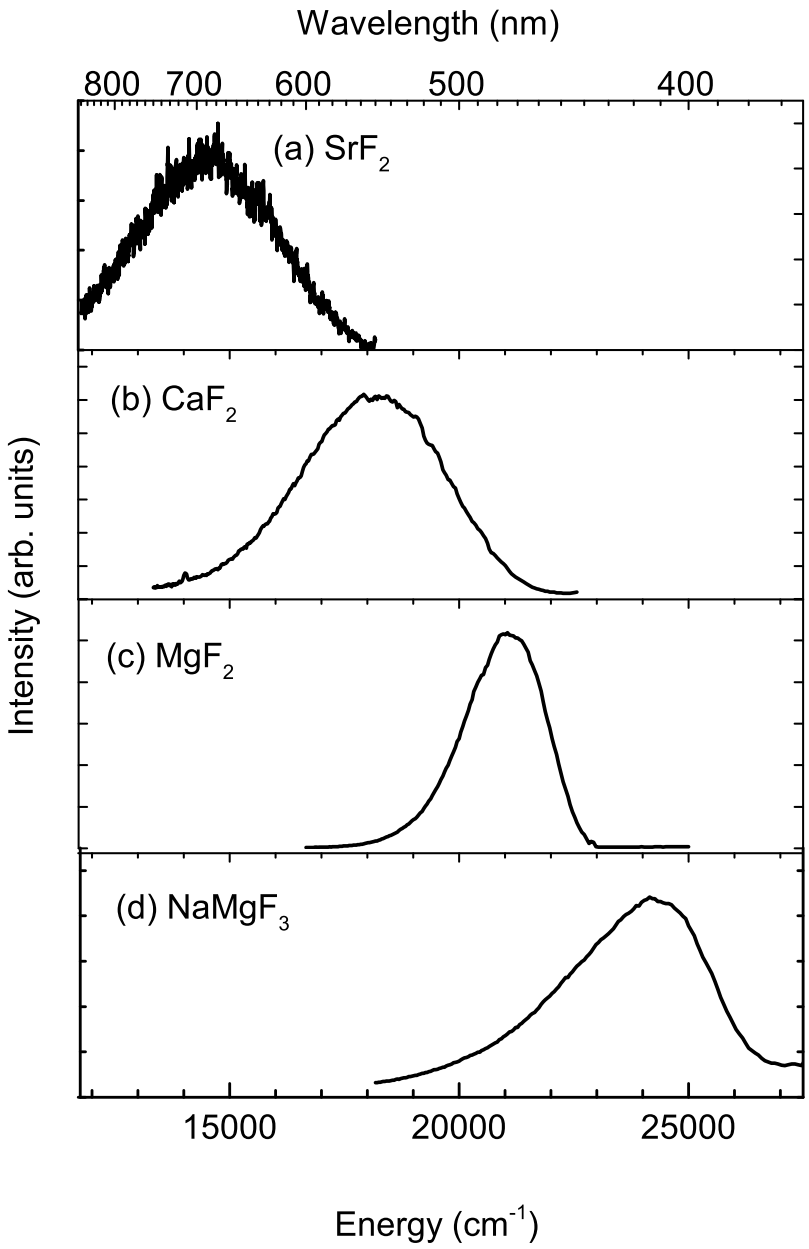

Table 4.2 Absorption and emission frequencies for fluoride host crystals doped with Yb^{2+} at 10 K. The absorption value corresponds to the centre of the lowest energy peak of the absorption spectrum. The emission values are the energy position corresponding to peak ITE emission intensity (or in the case of MgF_2:Yb^{2+} the peak $5d$ emission intensity). The lifetimes are attributed to the ITE ground state and excited state respectively. The emission position for SrF_2:Yb^{2+} is taken from the measurement at 15 K shown in Figure 4.2 rather than a published value.

	Absorption		Emission		Lifetime	
	(nm)	(cm^{-1})	(nm)	(cm^{-1})	τ_1 (ms)	τ_2 (μs)
SrF_2:Yb^{2+}	365	27.4 $\times 10^3$	690	14.5 $\times 10^3$	25 [a]	20 [a]
CaF_2:Yb^{2+} [a]	365	27.4 $\times 10^3$	565	17.7 $\times 10^3$	56	260
MgF_2:Yb^{2+} [b]	335	29.9 $\times 10^3$	475	21.1 $\times 10^3$	23	3000
$NaMgF_3$:Yb^{2+} S_a [c]	300	33.3 $\times 10^3$	476	21.0 $\times 10^3$	7.7	270
$NaMgF_3$:Yb^{2+} S_b [c]	300	33.3 $\times 10^3$	400	25.0 $\times 10^3$	8.9	140

[a] From Moine et al. [26] [b] From Lizzo et al. [76] [c] From Lizzo et al. [8]

4.3 X-ray Luminescence Spectra

When the fluoride crystals are excited at the energy of the Yb core $2p^{\frac{3}{2}}$ level (8949 eV i.e. 7.22×10^7 cm^{-1}) we see emission from three configurations: relaxation of STEs associated with the host lattice, ITEs trapped around Yb^{2+} sites, and Yb^{3+} transitions from the $^2F_{7/2}$ to $^2F_{5/2}$ state [87].

Figure 4.3 is the X-ray luminescence spectra for CaF_2:Yb. The peak at 33 000 cm^{-1} corresponds to emission from the STE. The peak at 18 000 cm^{-1} corresponds to emission from the Yb^{2+} ITE. The sharp peaks around 10 000 cm^{-1} are Yb^{3+} transitions.

In the X-ray luminescence spectra for SrF_2:Yb in Figure 4.4, emission from the STE at 33 000 cm^{-1} and Yb^{3+} transitions around 10 000 cm^{-1} are visible, but the Yb^{2+} ITE peak is quenched. The ITE emission is also quenched when SrF_2:Yb is excited with VUV light, as described in chapter 6, so high-energy excitation spectra could not be measured. There are dips in the STE emission band at 28 000, 37 000 and 39 000 cm^{-1}. The origin of these dips is likely to be an artifact in the measurement, as other X-ray luminescence measurements of the STE in SrF_2 show a smooth band from 25 000 to 40 000 cm^{-1} [42].

Figure 4.5 is the X-ray luminescence spectra for $NaMgF_3$:Yb. The STE peak at 20 000 cm^{-1} and the two ITE peaks at 25 000 cm^{-1} and 21 000 cm^{-1} are convoluted into one peak

Figure 4.3 X-ray luminescence of CaF_2:Yb at a sample temperature of 4 K excited at 8949 eV at two Yb concentrations.

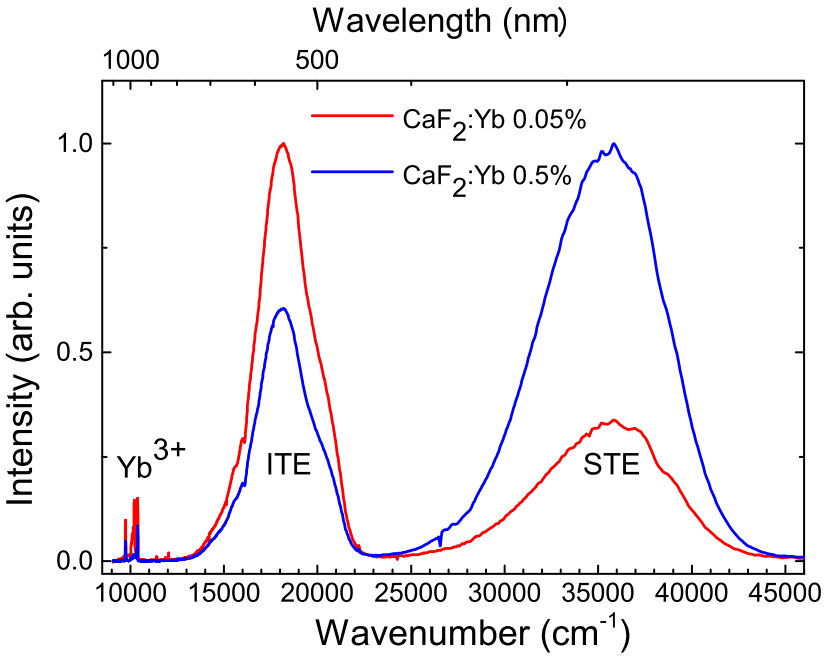

Figure 4.4 X-ray luminescence of SrF_2:Yb at a sample temperature of 4 K excited at 8949 eV at two Yb concentrations.

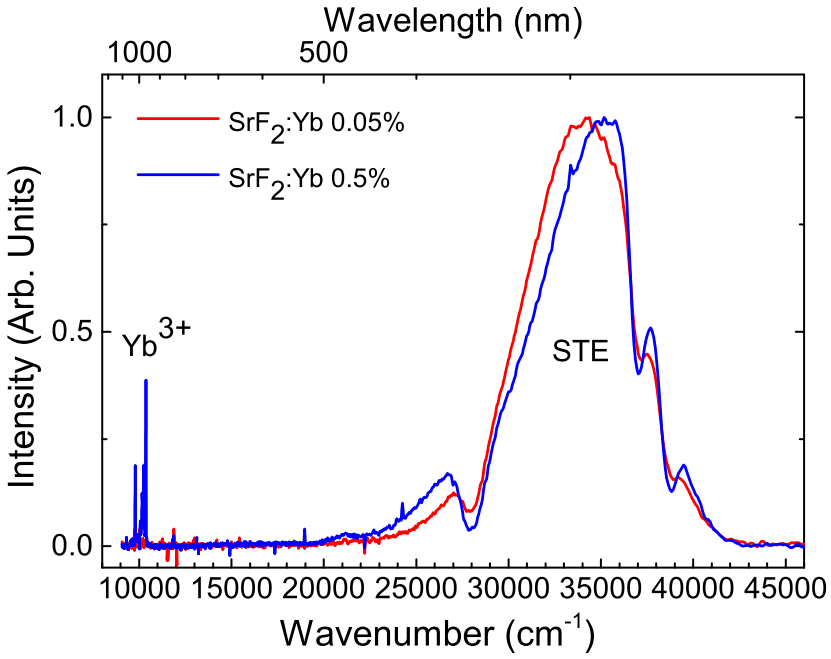

[8, 88]. The 80 K spectrum is dominated by the ITE emission, which is quenched in the 300 K spectrum, causing a relative increase in the higher-energy STE peak. A small peak of unknown origin at 14 000 cm^{-1} appears at 300 K.

Figure 4.5 X-ray luminescence of $NaMgF_3$:Yb excited at 8949 eV at two sample temperatures.

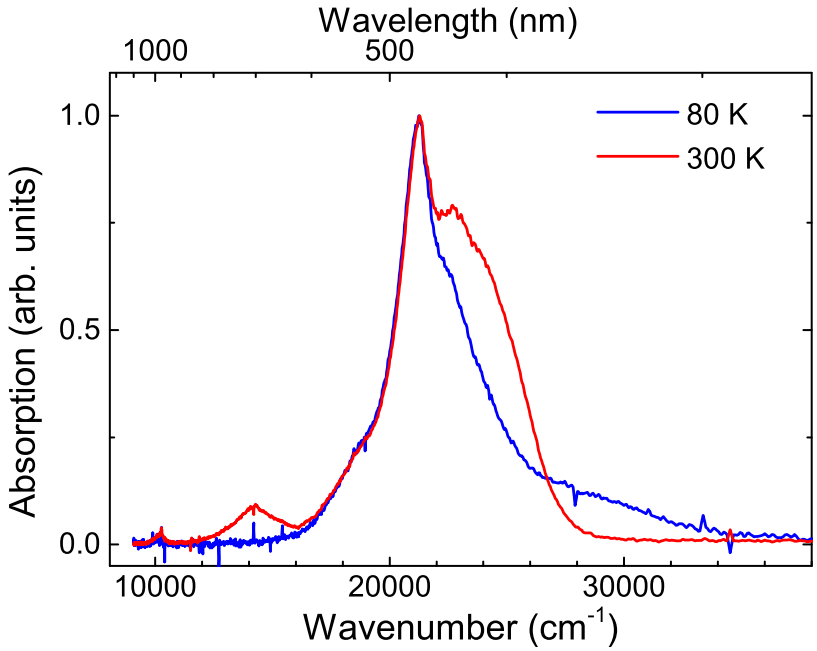

4.4 Valency Measurements using the XANES Technique

The valency of Yb in chloride hosts has been measured using X-ray Absorption Near Edge Structure (XANES). Excitation was scanned over the absorption resonance into the Yb L_3 core level (the $2p^{3/2}$ state) while measuring the X-ray fluorescence.

The near-edge features of XANES measurements are related to both the valency and site geometry of an ion [89]. The nature of this relationship is still an area of active research [90, 91]. Because of the difficulty of *ab-initio* analysis a semi-empirical indentification of peaks is often used, as it is in this work.

The presence of multiple sites in a crystal also effects XANES measurements by changing the shape of the band edge [90]. CaF_2:0.05%Yb^{3+} has two predominant sites, of trigonal and tetragonal point group symmetry [71]. Yb has multiple sites in $NaMgF_3$ as discussed in Chapter 1.

Optically-detected XANES, where an optical transition is monitored rather than the X-ray

emission, has been used to distinguish multiple sites in a material, but it is not a reliable detection scheme due to the complex relaxation pathways leading to the emission of an optical photon after excitation with X-ray energies [92]. This technique was attempted for $NaMgF_3$ and CaF_2 but no signal was detected.

There are two peaks in the X-ray fluorescence spectrum of Yb in the akaline earth fluorides which correspond to the trivalent and divalent valency states of Yb present in the crystals. An atom with a higher oxidation state requires an X-ray with higher energy to excite its core electrons because the nucleus is less-shielded and carries a higher effective charge [93].

XANES data was analysed with the software package Athena [94]. This program automatically subtracts background noise from the spectra and performs least squares fitting of the absorption edge and resonance peaks to output parameters corresponding to the areas, widths and positions of the edge and peaks. Comparing the areas of the peaks gives information about the ratio of the number of Yb ions in the crystal with each valency.

Previous valency measurements on Yb assumed the ratio of valency populations were simply given by the ratio of areas [95]. However, Antonio et al. [96] has shown that to find the exact ratio of valency population, the ratio between the X-ray emission transition probabilities for the two valency states must be known.

This ratio is not known for Yb, but it has been measured for Eu by measuring XANES on a specroelectrochemical cell which can change the valency of all the Eu in $EuCl_3.6H_2O$ from entirely Eu^{3+} to entirely Eu^{2+} [96]. The ratio of the areas are scaled by the ratio of the transition probabilities found for Eu^{2+} and Eu^{3+}. The valency populations $\frac{n^{3+}}{n^{2+}}$ is given by the ratio of the peak areas $\frac{A^{3+}}{A^{2+}}$ scaled by the ratio of the transition probabilities $\frac{P^{2+}}{P^{3+}}$:

$$\frac{n^{3+}}{n^{2+}} = \frac{A^{3+}}{A^{2+}} \frac{P^{2+}}{P^{3+}}.$$

The ratio $\frac{P^{2+}}{P^{3+}}$ is 0.656 for Eu [96]. This ratio is correlated to the strength of the $2p_{3/2} \rightarrow 5d$ transition in Eu. Since Yb is in the same chemical series as Eu and the same transition is being measured for Yb XANES, use of this ratio is justified.

Figure 4.6 presents the XANES spectrum for $NaMgF_3$:Yb. The parameters from the peak fitting are in Table 4.3 and the ratio of Yb^{3+} to Yb^{2+} is calculated to be 1.5 ± 0.3.

Figure 4.7 shows the XANES spectrum for CaF_2:Yb and SrF_2:Yb. The parameters from

the peak fitting are in Table 4.3. For both CaF_2:Yb and SrF_2:Yb, as the concentration of Yb in the crystal is increased from 0.05% to 0.5% the amount of Yb^{3+} compared to Yb^{2+} increases so that in the 0.5% samples the Yb^{2+} peak cannot be distinguished from the large Yb^{3+} peak. There is still Yb^{2+} in all the samples, as evidenced by continued detection of absorption and emission from Yb^{2+} states, but there is much more Yb^{3+} than Yb^{2+} in the samples with 0.5% Yb. The increasing amount of Yb^{3+} with increasing concentration is expected. A greater concentration of YbF_2 in the crystal causes the reduction to Yb^{2+} to be less effective and so more Yb^{3+} centres form in the crystal growth process [97]. At low Yb concentrations, Yb^{3+} ions have been identified in CaF_2 at cubic and trigonal sites but at concentrations higher than 0.05% the Yb^{3+} ions form clusters [71].

Figure 4.6 XANES edge fit for $NaMgF_3$:0.5%Yb^{2+} using the parameters in table 4.3.

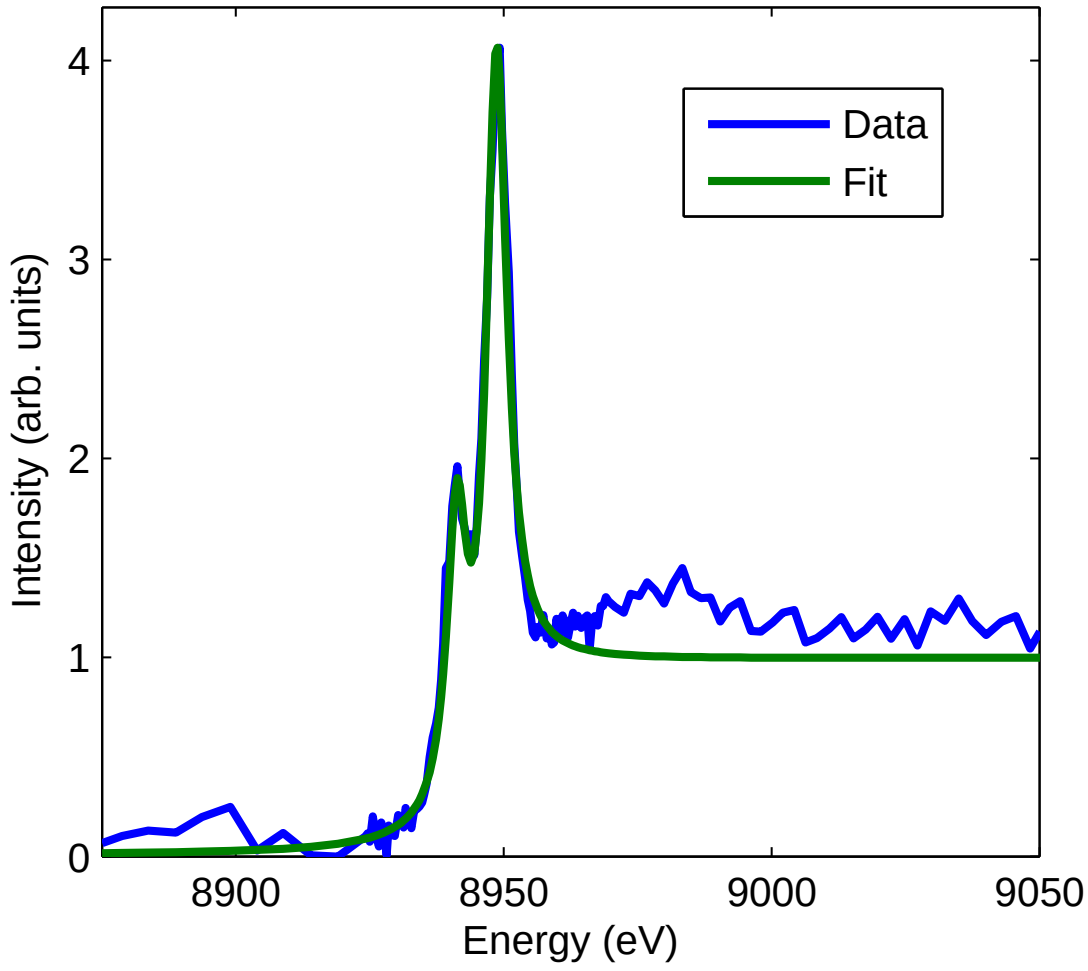

Table 4.3 Parameters for edge fitting XANES data from alkaline earth fluorides doped with ytterbium. Fits are shown in Figures 4.6 and 3.1. Yb^{3+} and Yb^{2+} are Lorentzian functions and edge corresponds to an arctangent function centred at E with width Γ.

		E (eV)	Area	Γ (eV)	$\frac{Area^{3+}}{Area^{2+}}$	$\frac{n^{3+}}{n^{2+}}$
$NaMgF_3$	Yb^{3+}	8948.64 ± 0.18	19.8 ± 1.5	4.73 ± 0.26	-	-
0.6%	Yb^{2+}	8941.1 ± 0.9	8.7 ± 1.1	4.4 ± 0.4	2.3 ± 0.5	1.5 ± 0.3
	Edge	8947.9 ± 1.6	0.88 ± 0.03	2.8 ± 1.4	-	-
CaF_2	Yb^{3+}	8948.93 ± 0.17	30.2 ± 1.2	5.5 ± 1.2	-	-
0.05%	Yb^{2+}	8941.4 ± 0.8	5.6 ± 0.8	4.3 ± 0.3	5.39 ± 0.98	3.5 ± 0.6
	Edge	8948.0 ± 2.4	1.06 ± 0.12	5.5 ± 1.2	-	-
CaF_2	Yb^{3+}	8949.04 ± 0.14	31.3 ± 1.0	5.79 ± 0.09	-	-
0.5%	Edge	8947 ± 3	0.90 ± 0.16	4.0 ± 1.0	-	-
SrF_2	Yb^{3+}	8948.89 ± 0.17	17.1 ± 2.1	5.4 ± 0.4	-	-
0.05%	Yb^{2+}	8941.4 ± 2.0	2.8 ± 1.2	4.5 ± 1.1	6 ± 3	2.2 ± 1.2
	Edge	8947 ± 4	0.55 ± 0.03	2.7 ± 1.5	-	-
SrF_2	Yb^{3+}	8949.02 ± 0.11	39.5 ± 0.9	5.96 ± 0.08	-	
0.5%	Edge	8947.6 ± 2.3	0.96 ± 0.13	3.5 ± 0.8	-	

4.5 Conclusion

This chapter has shown the absorption and emission of the Yb-doped alkaline earth fluorides studied in this thesis. XANES measurements have been used to identify the oxidation state of the Yb dopant. Tables 4.2 and 4.3 give basic optical and oxidation properties of the materials in this thesis and will be used for reference in later chapters.

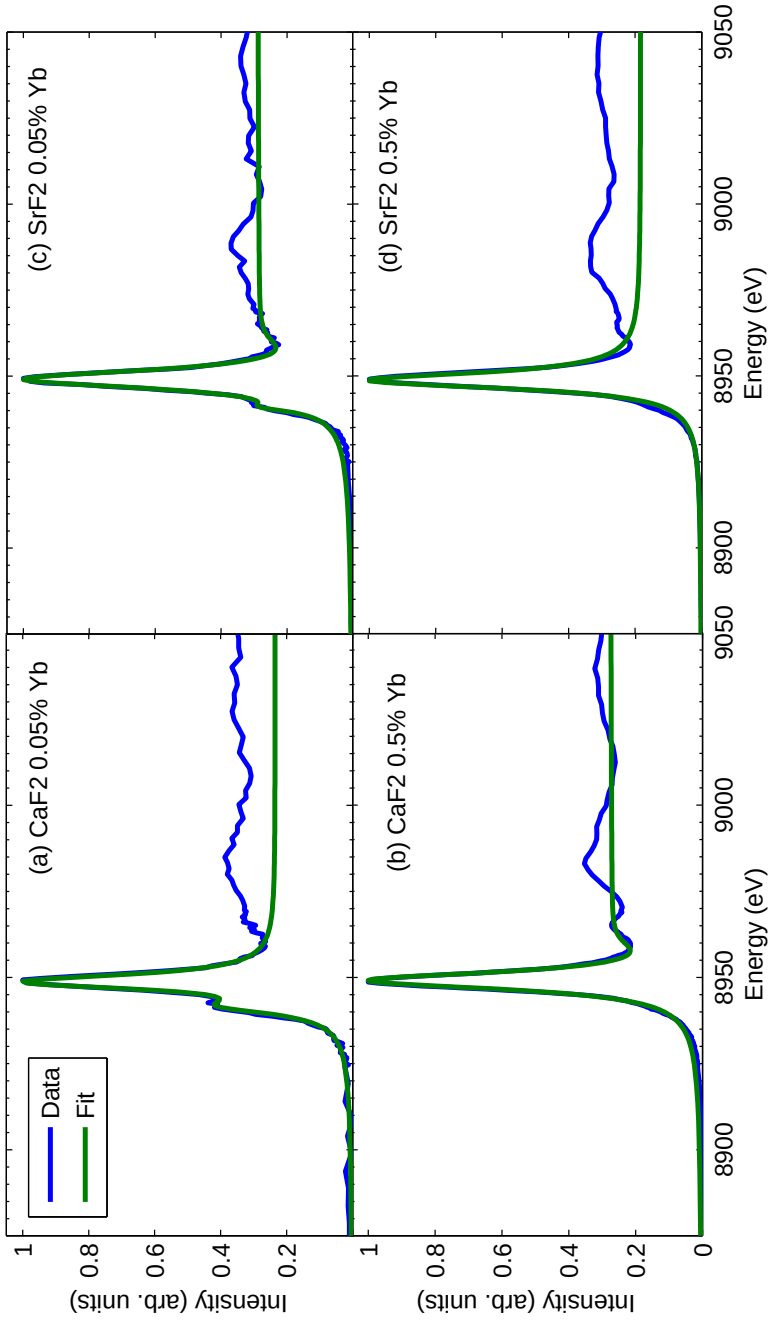

Figure 4.7 XANES edge fit for CaF_2:Yb and SrF_2:Yb at two Yb concentrations using the parameters in table 4.3.

Chapter 5

Site Selective Transient Photoluminescence Enhancement of Impurity-Trapped Excitons in $NaMgF_3$:Yb^{2+}

Fluoride crystals doped with Yb^{2+} are often observed to have wide emission bands and large Stokes shifts compared to the $4f^n \rightarrow 4f^{n-1}5d^1$ transitions. This characteristic "anomalous" emission has been attributed to transitions from impurity-trapped excitons which are bound to the ytterbium ions. Dorenbos has collected 48 Yb^{2+} -doped crystal hosts which are characterised with "anomalous" emission [9].

In Chapter 1, we discussed how it is more difficult to identify $5d$ energy levels than $4f$ levels because they are influenced by the surrounding lattice so $4f^{n-1}5d^1 \rightarrow 4f^n$ transitions are broad. ITEs are even more difficult to characterise as the ITE states are delocalised on surrounding cations. There is a large configurational shift between $5d$ energy levels and ITE states, often causing even greater vibronic broadening of the emission than for $4f^{n-1}5d^1 \rightarrow 4f^n$ transitions. It is also difficult to identify absorption into states which will result in formation of ITEs, due to their proximity to the conduction band, so the energy levels have only been inferred from the broad ITE emission spectra. To construct detailed models of ITEs, indirect methods of probing the ITE states must be employed. For instance, work has been carried out to measure ITE emission at high pressures, as the shift in emission as pressure is increased can be used to construct the configurational coordinate shift between $5d$ impurity states and ITE states [98].

In this chapter a two-colour technique called site-selective transient photoluminesence enhancement (SSTPE) is applied to $NaMgF_3$:Yb^{2+} to study ITEs. By exciting the material with both UV and IR radiation, ITEs can be created and then promoted to excited states. The ITE states are investigated by varying experimental parameters such as temperature, excitation power and wavelength.

5.1 Site-Selective Transient Photoluminescence Enhancement

SSTPE is a pulsed, two-colour excitation technique. The sample is excited with a UV excitation pulse (in this case 33 000 cm^{-1}) from an optical parametric amplifier to populate the ground state of the impurity-trapped exciton which is created subsequent to resonant excitation of the inter-configurational Yb^{2+} $4f^{14} \rightarrow 4f^{13}5d$ absorption. After a variable time delay (on the order of 100 μs) the sample is probed with an IR pulse derived from a free electron laser. The IR pulse excites the impurity-trapped exciton from its ground state into an emitting excited state with a shorter lifetime. As a consequence of the different radiative relaxation rates of the excitonic levels, a temporal enhancement in emission can be detected.

A two-colour experimental technique has been previously employed to probe the ITE energy levels of ytterbium-doped calcium fluoride and strontium fluoride [28] as well as electron trap liberation in ytterbium-doped magnesium fluoride [33]. Here we illustrate that a two-colour technique is also applicable to multi-site crystals.

In $NaMgF_3$:Yb^{2+}, the Yb^{2+} replace Na^+ ions and there are at least two charge-compensation sites available for occupancy as discussed in section 1.2.3. The emission band of $NaMgF_3$:Yb^{2+} is reported to be a convolution of emission from impurity-trapped exciton states of two of the charge-compensating arrangements [9]. By monitoring emission at either extreme of the emission band profile we can discriminate between the two sites.

5.2 Two-Dimensional Spectroscopy

Figure 5.1 shows the time evolution of the emission subsequent to pulsed excitation at 33 000 cm^{-1} (300 nm) and 952 cm^{-1} (10.5 μm), illustrating the ITE emission wavelength dependence of the photoluminescence enhancement. The observed band is the convolution of emission from two charge-compensation sites which have centre wavelengths of 22 000 cm^{-1} (455 nm) and 24 000 cm^{-1} (417 nm) respectively. The two charge-compensation arrangements (labeled site S_a and site S_b) can be spectrally deconvolved — albeit to a lesser degree for the minority arrangement, labeled site S_b. Figure 5.2 shows the emission spectrum of $NaMgF_3$:Yb^{2+} after UV excitation at 300 nm. By monitoring the emission at points on either side of the overall emission band shown in Figure 5.2 the contribution of each site for two emission wavelengths is seen. At 21 000 cm^{-1} (476 nm, labeled emission 1) the emission is entirely from site S_a and at 25 000 cm^{-1} (400 nm,

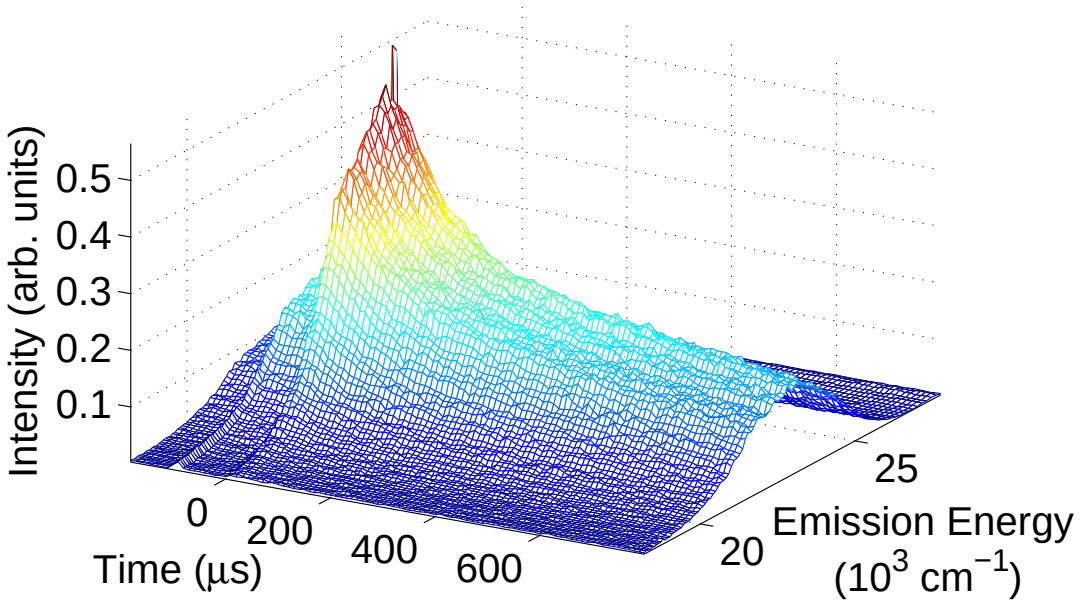

Figure 5.1 8 K emission spectrum of $NaMgF_3$:Yb^{2+} subsequent to excitation at 33 000 cm^{-1}. At t = 0, 952 cm^{-1} excitation occurs triggering the photoluminescence enhancement

labeled emission 2) the emission is predominantly from site S_b. Figure 5.4 illustrates this point, showing the SSTPE IR excitation spectrum for both sites by monitoring emission at the two energies indicated in Figure 5.2.

The emission band widths and therefore bond length changes are very different for the two charge-compensation sites of $NaMgF_3$:Yb^{2+}. The two sites are therefore likely to have significantly different charge-compensation geometries. The emission band widths for $NaMgF_3$:Yb^{2+} are less than in CaF_2:Yb^{2+} and much less than the widths of the $4f^{13}5d^1$ absorption transitions — the lowest energy $4f^{13}5d^1$ absorption transition is 800 cm^{-1} wide in CaF_2:Yb^{2+} (from [26]). The absorption widths are difficult to measure in $NaMgF_3$:Yb^{2+} due to multiple origins at similar energies [8] but the widths are likely to be similar to CaF_2:Yb^{2+}. The transitions from the ITE to the $4f^{14}$ states involve a greater configurational shift than transitions between $4f^{14}$ and $4f^{13}5d^1$ states of Yb^{2+}.

Using a similar method as applied to CaF_2:Yb^{2+} in [28], bond length changes may be estimated for both sites of Yb^{2+} in $NaMgF_3$ from the emission bandwidths in Table 5.1. The width of the emission is related to the Huang-Rhys parameter S. The Huang-Rhys parameter is a measure of the linear vibrational coupling to electronic excitations through

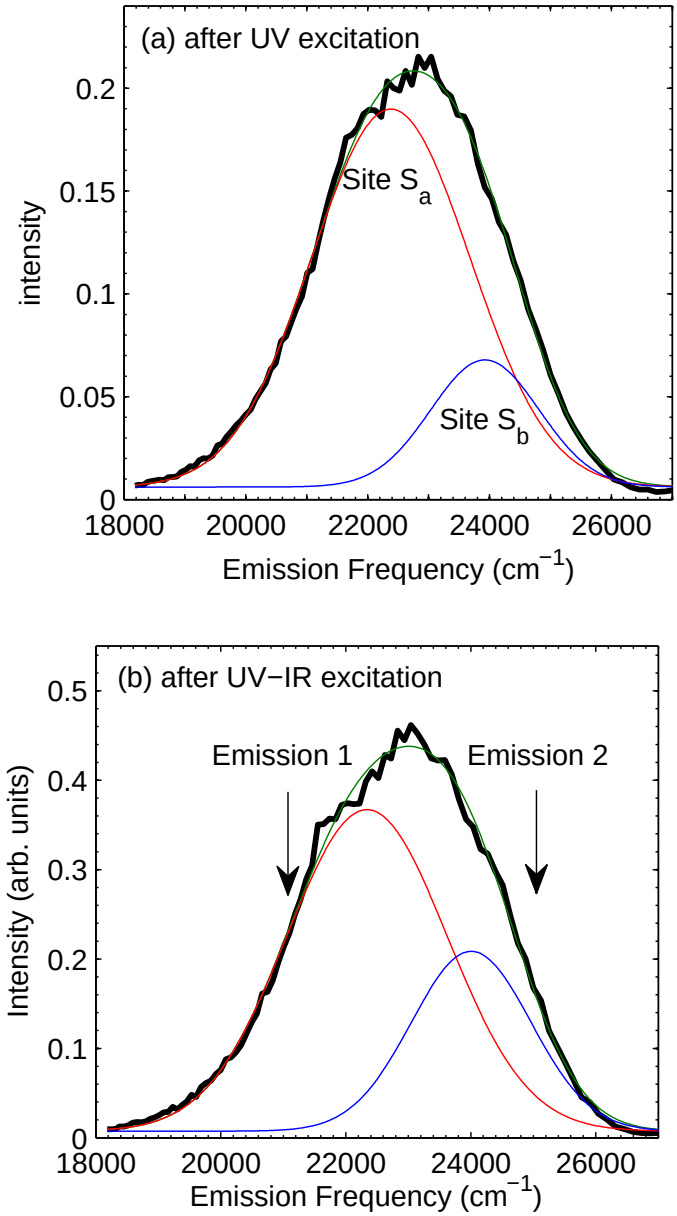

Figure 5.2 8 K emission spectrum of $NaMgF_3:Yb^{2+}$ (a) after UV excitation at 33 000 cm^{-1}. Two charge compensating arrangements are evident with emission bands centred around 22 300 cm^{-1} and 24 000 cm^{-1} respectively. (b) after UV excitation at 33 000 cm^{-1} and IR excitation at 952 cm^{-1}. After excitation with the IR pulse the relative intensity of site S_b compared to site S_a has increased from (a). At 21 000 cm^{-1} (emission 1) practically all the light is from site S_a, but at 25 000 cm^{-1} (emission 2) the ratio of intensity from sites 1 and 2 is approximately 1:2.

Table 5.1 Parameters for Gaussian function fits of the emission bands in Figure 5.2 for (a) UV excitation only and (b) UV-IR excitation. ΔR is the change in bond length associated with the transition. ZPL is the zero phonon line, found by adding the Stokes shift (calculated from the width of the band) to the centre of the emission.

(a) UV excitation

	Center S_a	Center S_b
E_{centre} (cm^{-1})	22400±180	23900±130
Height (arb. units)	0.18±0.02	0.06±0.03
FWHM (cm^{-1})	3100±180	2100±300
ΔR (Å)	-0.13 ±0.01	-0.08 ± 0.01
E_{ZPL} (cm^{-1})	27000±3000	26000±7000

(b) UV-IR excitation

	Center S_a	Center S_b
E_{centre} (cm^{-1})	22300±200	24000±140
Height (arb. units)	0.36±0.04	0.20±0.06
FWHM (cm^{-1})	3000±200	2300±170
ΔR (Å)	-0.12 ± 0.01	-0.09 ± 0.01
E_{ZPL} (cm^{-1})	27000±4000	27000±4000

the difference between ground and excited state geometries.

$$S = \left(\frac{\Gamma}{2.36\,\nu} \right)^2 . \tag{5.1}$$

Since the Huang-Rhys parameter S is related to the difference between ground and excited state geometries. When the value of S is known for a certain transition, it can be used to estimate the change in ligand bond length ΔR if we know the effective phonon frequency ν, reduced ligand mass μ and number of surrounding ligands n_{lig}:

$$\Delta R = \sqrt{\frac{S\hbar}{n_{\text{lig}}\,\pi\,c\,\nu\,\mu}} \tag{5.2}$$

[73, 99] The calculation is approximate because it uses an effective phonon frequency of 325 cm^{-1} which is estimated for CaF_2:Yb^{2+} in [28] and should allow comparison between fluoride systems. The Yb^{2+} site in $NaMgF_3$ is assumed to have a coordination number of 12 [30]. The bond length change between ITE configuration and the $4f^{14}$ ground state remain constant for both sites within uncertainties after IR excitation so the bond lengths of the lower and higher exitonic states are similar.

The width of the emission bands can also be used to calculate the zero phonon line (ZPL) positions [73] for both sites of $NaMgF_3$:Yb^{2+} which are listed in Table 5.1. Notably site S_a actually has a higher energy ZPL than site S_b, although we see lower energy emission from site S_a, due to the greater width of the site S_a emission band.

Two-dimensional representations of the emission enhancement are constructed by scanning across a range of IR wavelengths with the FEL (5-12 μm) and measuring the emission enhancement and decay at each IR wavelength. In Figure 5.3 the sample has been excited with a 300 nm (33 300 cm^{-1}) UV pulse, creating ITEs. The subsequent emission is from two ITE energy levels, described in Table 5.3. The large difference in radiative rates between these energy levels means the ratio of population in either state can be inferred from the dynamic behaviour of the emission. When the temperature of the sample is at 8 K, most of the population is initially in the ITE ground state (with a lifetime of the order of 8 ms). At $t = 0$ an IR pulse excites the impurity-trapped exciton from its ground state into excited ITE states with a shorter lifetime (on the order of 300 μs) which generates an emission enhancement via the population redistribution. When the temperature is increased to 40 K, the higher ITE state becomes thermally populated leaving fewer excitons available for IR excitation directly from the ground state. Figure 5.3 shows the emission

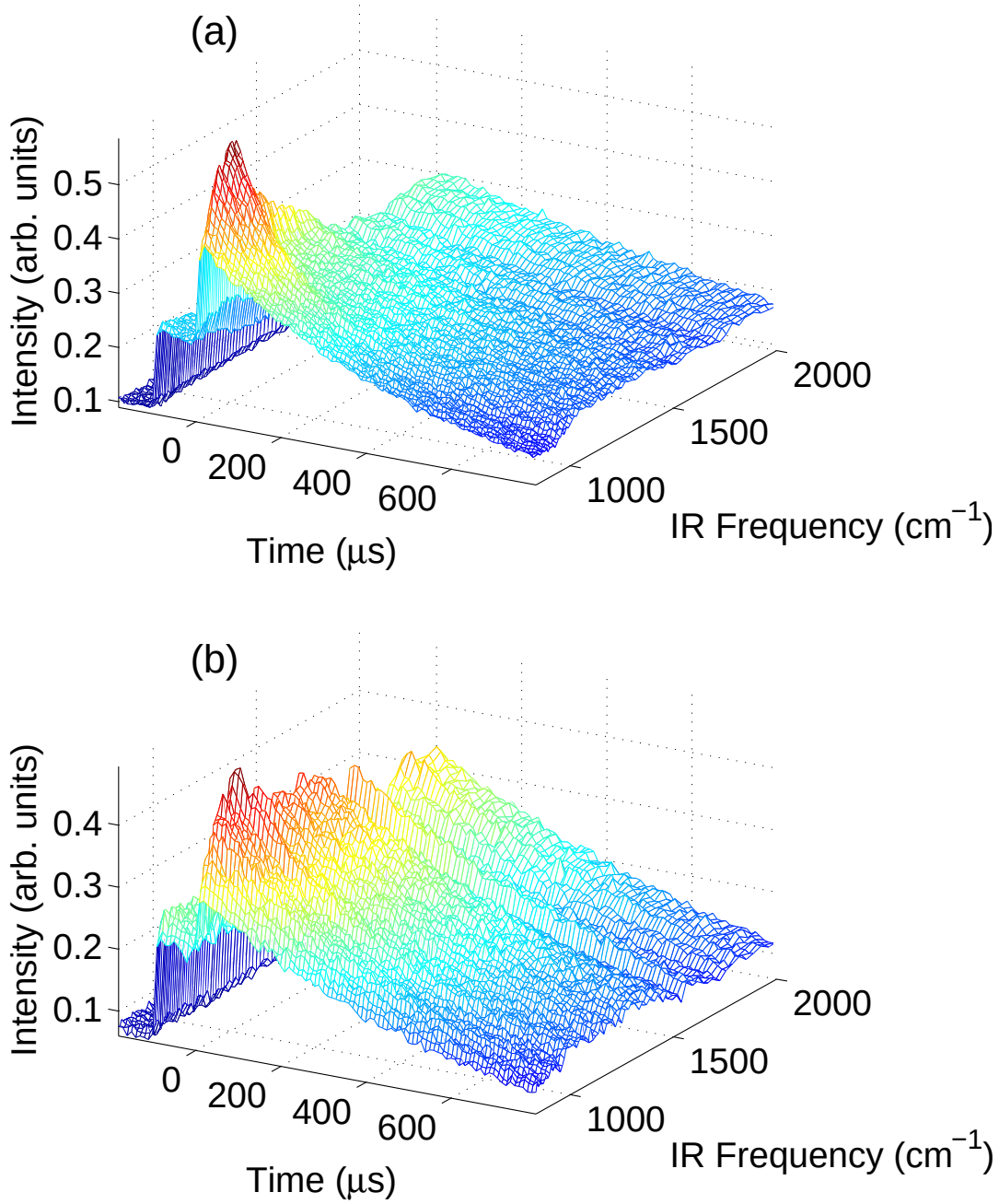

Figure 5.3 Time evolution of the SSTPE excitation spectrum of $NaMgF_3:Yb^{2+}$ subsequent to excitation with a 33 300 cm^{-1} pre-pulse. The IR excitation is 952 cm^{-1} at 0 s. Emission is monitored at 23 300 cm^{-1} (430 nm). (a) 8 K and (b) 40 K. The peak centreed at 950 cm^{-1} is from intra-excitonic transitions.

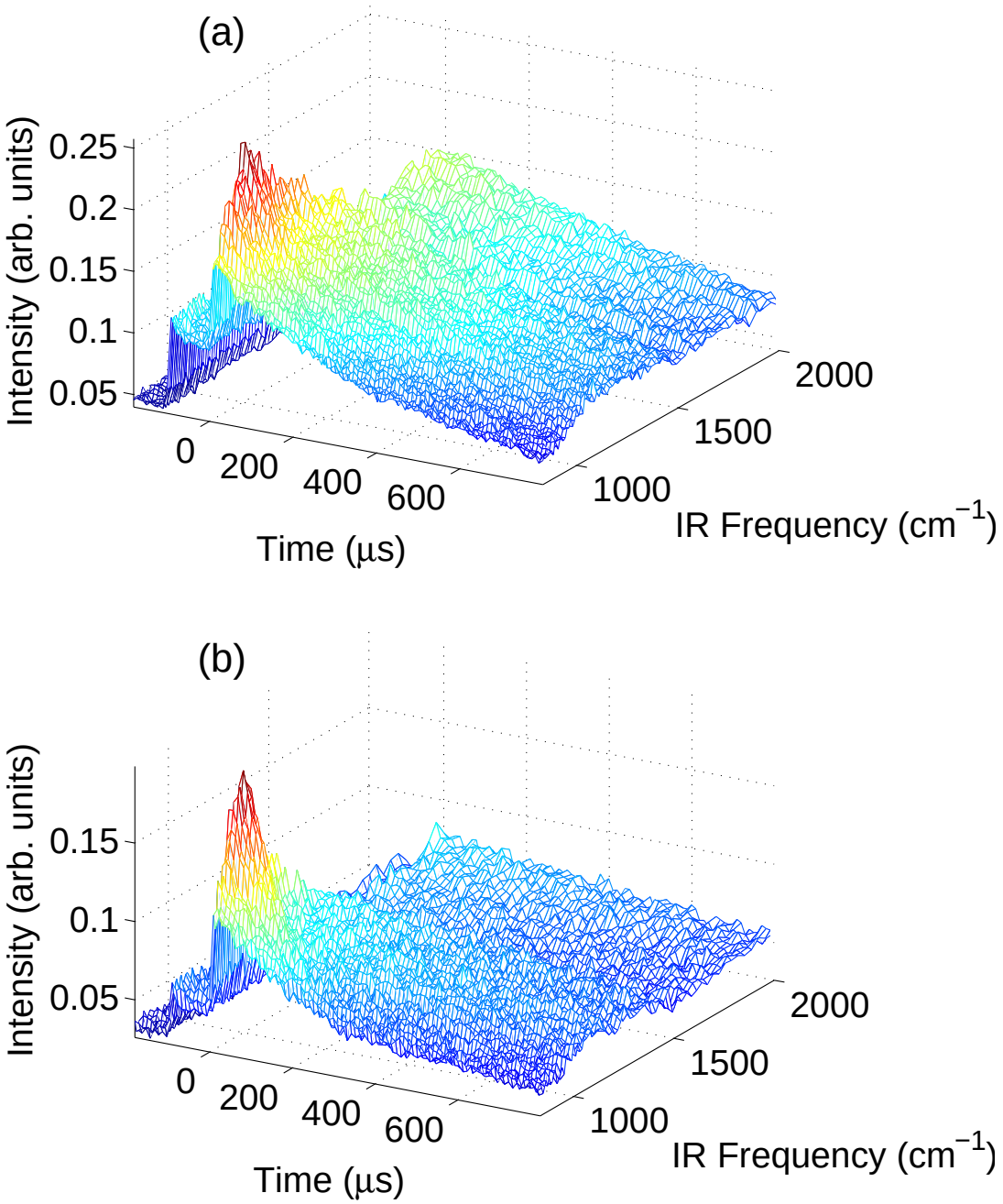

Figure 5.4 8 K site-selective excitation spectra of $NaMgF_3:Yb^{2+}$ after excitation with a 33 300 cm^{-1} pre-pulse at a temperature of 8 K. The IR excitation is 952 cm^{-1} at 0 s (a) Emission at 21 000 cm^{-1} (emisson 1 in Figure 5.2) shows dynamics of site S_a. (b) Emission at 25 000 cm^{-1} (emisson 2 in Figure 5.2) shows dynamics of site S_b.

Table 5.2 The postitions and widths of the peaks in Figure 5.5.

	Centre (cm^{-1})	Width (cm^{-1})
Emission 1	9600	270
Emission 2	9500	180

monitored at the centre of the band in Figure 5.2(a), that is a mixture of emission from sites S_a and S_b. Figure 5.4 shows the SSTPE IR excitation spectrum for both sites by monitoring emission at the two energies indicated in Figure 5.2(b).

5.3 Intra-Excitonic Absorption

The excitation spectrum of the IR enhancement from both sites in $NaMgF_3$:Yb^{2+} shows a distinct peak at 950 cm^{-1}. The excitation spectrum (Figure 5.5) is constructed by integrating the emission in Figures 5.3 and 5.4 over the first 50 μs after the IR excitation. Two separate emission scans monitored at the emission peak 23 300 cm^{-1} (430 nm) – one from 500 to 900 cm^{-1} and another from 830 to 2000 cm^{-1} – are plotted together in Figure 5.5. The curves are all normalized to the emission at 2000 cm^{-1}.

As previously discussed, the peak at 950 cm^{-1} cannot be due to heating, since emission predominantly from site S_b increases more than emission from site S_a despite site S_a having a smaller energy difference between ITE levels than site S_b.

The widths of the peaks listed in Table 5.2 are difficult to estimate because there is a step function associated with the trap liberation that makes the background intensity higher on the high energy side of the peaks in Figure 5.5. The widths are the full width half maximum from the parts of the peak which have an intensity higher than one, i.e. the background is taken from the higher energy side of the peak. The configurational shift between ITE states is small since the widths of the peaks listed are much narrower than the exciton emission bands in Table 5.1 or the (approximately) 1200 cm^{-1} wide Yb^{2+} $4f^{14} \rightarrow 4f^{13}5d$ absorption peaks [8].

The temporal analysis in the following section allows us to confidently determine that the excitation peak at approximately 950 cm^{-1} in Figure 5.5 indicates the FEL is being resonantly absorbed into the higher exciton state, so there are excited ITE states 950 cm^{-1} above the ITE ground state.

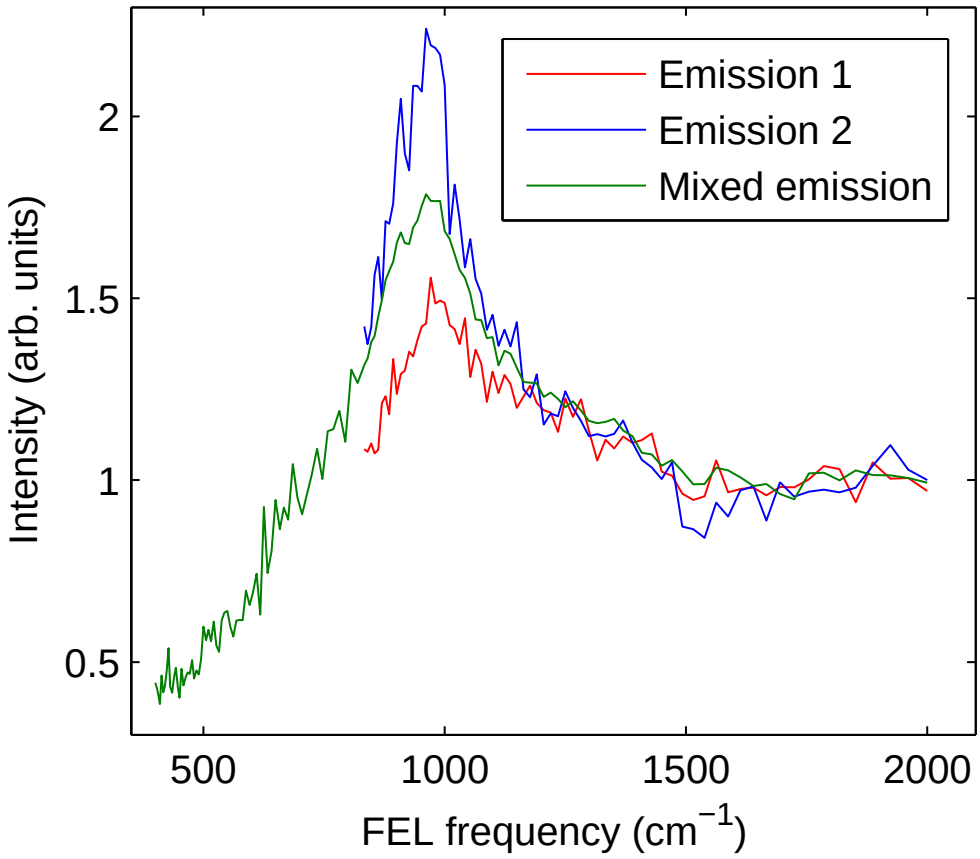

Figure 5.5 Emission of $NaMgF_3:Yb^{2+}$ shown in Figure 5.4 at a sample temperature of 8 K integrated over the first 50 μs after the IR excitation and monitored in the middle and at either side of the emission band in Figure 5.2. Mixed emission refers to the signal monitored at the centre of the emission band at 23 300 cm^{-1}. This emission has been seperately measured for a lower-energy region (from 500 to 900 cm^{-1}) and normalized. The excitation peak indicates the position of the excited ITE energy levels.

5.4 Analysis of Emission Dynamics

The large difference between the radiative rates of the two emitting ITE levels means that the relative population distribution between these states can easily be inferred from the temporal behaviour of the emission. Figure 5.4 shows an initial emission enhancement caused by the IR pulse and a subsequent decay, suggesting IR excitation into a shorter-lifetime radiative state. At some wavelengths the intensity of the emission after hundreds of microseconds is greater than before the IR pulse, which indicates the IR pulse is liberating electron traps to provide extra population to the ITE states.

The temporal transients are modelled with a system of rate equations as discussed in Chapter 2. These represent the multi-level exciton and trap liberation. In the model, the UV pulse generates the exciton ground state as well as free carriers in the conduction band which subsequently fall into shallow traps. The IR pulse causes intra-excitonic transitions and liberates carriers from traps, some portion of which ultimately populate the exciton ground state.

The energy levels shown in Figure 5.6 are:

1 The ground state of divalent ytterbium.

2 The ground state of the impurity trapped exciton, with radiative rate A_{21}

3 A state of the impurity trapped exciton with, radiative rate $A_{31} > A_{21}$

4 A higher-energy exciton state.

C The conduction band, populated by electron trap liberation.

There are two processes being modeled. The first is the IR pulse exciting excitons from the ground exciton state (2) to a higher exciton state (4) where they decay to the second exciton state (3) and radiatively decay to the ytterbium ground state (1). The second process is the IR pulse liberating electrons from trap states to the conduction band (C) where they recombine with ytterbium ions to form impurity-trapped excitons in the lower exciton state (2) which radiates to the ytterbium ground state (1). The change in population of the above states are modeled with the following rate equations:

$$\frac{dN_1}{dt} = A_{21}N_2 + A_{31}N_3 + W_{41}N_4 + W_{C1}N_5 \tag{5.3}$$

$$\frac{dN_2}{dt} = -(A_{21} + W_{23} + F_{24})N_2 + W_{32}N_3 + W_{C2}N_C \tag{5.4}$$

$$\frac{dN_3}{dt} = W_{23}N_2 - (A_{31} + W_{32})N_3 + W_{43}N_4 \tag{5.5}$$

$$\frac{dN_4}{dt} = F_{24}N_2 - (W_{41} + W_{43})N_4 \tag{5.6}$$

$$\frac{dN_C}{dt} = F_{TC} - (W_{C1} + W_{C2})N_C \tag{5.7}$$

The initial population distribution is at thermal equilbrium, and the assigned temperature is the same as at several hundred μs after the IR excitation. The pumping term F_{24} is the rate of population transfer from the lower to higher excitonic states. F_{TC} is proportional to the number of electrons released from traps. W_{C2} is the rate at which population that has been added to the system from liberated electron traps (determined by F_{TC}) recombines with ytterbium ions to form ITEs in their ground state. A better fit to the experimental data was achieved when the parameter W_{53} representing ITEs forming in their excited state was zero. W_{C2} represents electron recombination to ITEs, and the non-radiative rates between the ITE states 2 and 3 control the distribution of these new oscillators within the ITE levels. W_{43} is the non-radiative rate between higher excitonic states and the second excitonic state (3 on Figure 2.1). W_{41} and W_{C1} are rates of population loss from the higher excitonic states and the conduction band respectively to the ground state. A_{21} and A_{31} are the radiative rates from the exciton levels.

The population in the higher excitonic state 4 that does not transition to the upper ITE state is modeled as only going to the ground state in a rate W_{41}. The model can be modified so this population goes instead to the lowest ITE state in a rate W_{42}. If W_{42} is used instead of W_{41}, more oscillators remain in the ITE system after the IR excitation and to balance this the rate of oscillators entering the system via trap liberation F_{TC} is less. It is still neccessary to have trap liberation to explain the intensity hundreds of microseconds after IR excitation. Since there is no way of determining the ratio between the rates W_{41} and W_{42}, in the model presented here W_{42} is assumed to be zero which gives a better fit than assuming W_{41} is zero.

To ensure thermal equilbrium, the non-radiative rates between the exciton states 2 and 3 are related by a Boltzmann factor:

$$W_{23} = W_{32}\frac{g_3}{g_2}\exp\left(\frac{-\Delta E_{23}}{kT}\right), \tag{5.8}$$

where g_2 and g_3 are the energy level degeneracies, ΔE_{23} is the energy gap separating the exciton energy levels 2 and 3, T is temperature and k is Boltzmann's constant. The level degeneracies are set to $g_2 = 1$ and $g_3 = 3$. Since the structure of $NaMgF_3$ is approximately octahedral, as in the case of the systems analysed by Moine et al. [26] the exciton energy levels will be the result of coupling a doubly-degenerate delocalised ^2s state with a doubly-degenerate $4f^{13}$ state. The level degeneracies do not denote triplet and singlet states: As stated in Moine et al. energy levels 2 and 3 are a mixture of triplet and singlet states. The assignment $g_2 = 1$ and $g_3 = 3$ is made to be consistent with the work of Moine et al.

The non-radiative relaxation rates between the exciton energy levels 2 and 3 and the ground state (1) have not been taken into account because they are negligible in comparison to the radiative rates A_{21} and A_{31} at temperatures below 50 K [8].

The radiative rates and energy level gap between the excitonic states have been previously calculated from the temperature dependence of the total emission lifetime [8]. The parameters in Table 5.3 were found by fitting the lifetime data to a two-level model as follows:

$$\tau = \frac{g_2 + g_3 e^{-\Delta E/kT}}{g_2 A_2 + g_3 A_3 e^{-\Delta E/kT}} \tag{5.9}$$

Equation 5.9 is derived from the statements $A = \frac{n_2}{n_2+n_3}A_2 + \frac{n_3}{n_2+n_3}A_3$, that the total radiative rate is the combination of the radiative rates from levels 2 and 3, and that the populations of these levels are related by a Bolzmann distribution: $\frac{n_3}{n_2} = g_3 g_2 \exp -\Delta E/k_B T$.

The uncertainties in Table 5.3 are the square root of the covariance matrix, except in the case of the rate A_{31} for site S_b, where the square root of the covariance term gave an uncertainty of over 100%. In that case, an estimate is given based on varying the parameter until the fit is noticeably incorrect by eye.

Note the radiative rates and energy level gaps are not the same as Lizzo's values [8] because Lizzo et al. chose the degeneracies of the energy levels as $g_2 = g_3 = 1$ whereas we chose $g_3 = 3, g_2 = 1$ as discussed above [26].

The energy difference between the ITE states is less for site S_a than it is for site S_b,

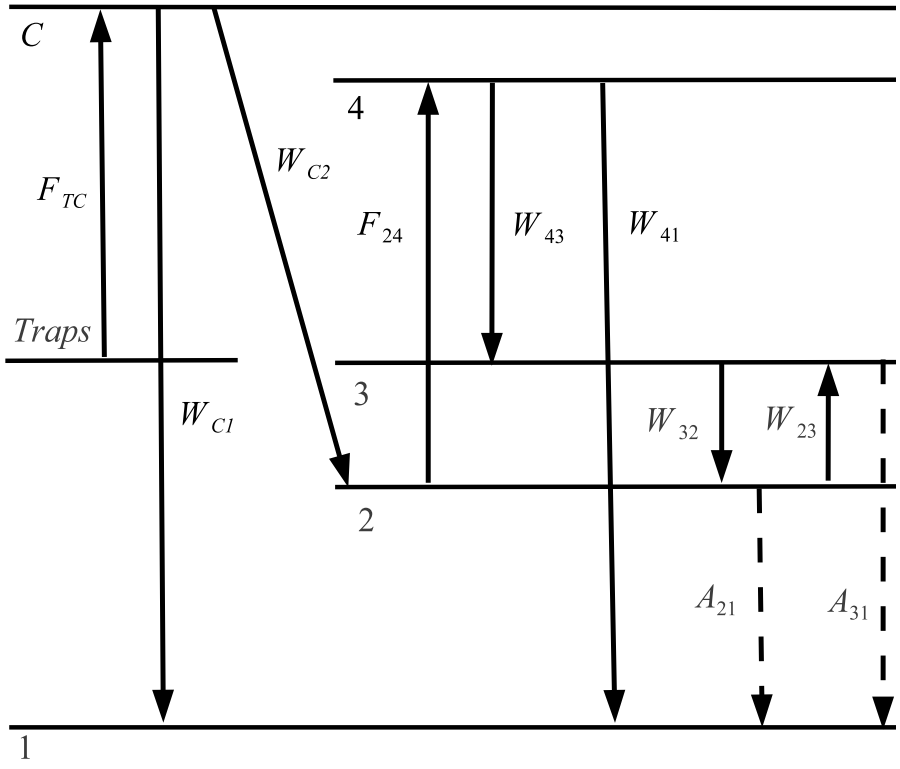

Figure 5.6 The energy level transitions involved in the dynamic behaviour of $NaMgF_3:Yb^{2+}$ after IR excitation. The transitions are labeled with the rates used in Equations 5.3-5.7. W terms represent rates of non-radiative transitions. F terms are mechanisms driven by the IR pulse, which are the population transfer from the lower to higher excitonic states (F_{24}) and electrons released from traps (F_{TC}). A_{21} and A_{31} are the radiative rates from the ITE levels.

Table 5.3 Parameter values for modeling $NaMgF_3$:Yb^{2+} emission. These rates are used throughout the analysis whereas other rates shown in Figure 5.6 are varied to model different power, temperature and excitation wavelengths. The values in brackets are the radiative lifetimes corresponding to the rates. The radiative rates and ITE energy level differences were calculated from the temperature dependence of the total emission lifetime [8].

	Site S_a	Site S_b
A_{21} (s^{-1})	132 ± 7 (7.6 ms)	113 ± 8 (8.8 ms)
A_{31} (s^{-1})	2100 ± 400 (480 μs)	2800 ± 500 (350 μs)
ΔE_{23} (cm^{-1})	24 ± 2	62 ± 18
g_2	1	1
g_3	3	3
W_{42} (s^{-1})	5.0×10^5	5.0×10^5

which is demonstrated in Table 5.3. This variation in energy difference means that if the temperature of the system is increased from 8 K, the intensity of emission from site S_a should increase more than from site S_b. From Figure 5.2, we see that when the system is excited with IR radiation the opposite occurs — emission from site S_b increases more than emission from site S_a. This site-dependent mechanism and the varying lifetimes of the IR-induced emission enhancement indicates the IR pulse is having some effect other than simply heating the sample.

In the following analysis the parameters in Equations 5.3–5.7 (shown in Figure 5.6) are used to accurately simulate the emission enhancement as it varies with temperature, power and IR wavelength. In addition, IR excitation yields a modest heating-related enhancement to the non-radiative rates. In all cases we use $W_{42} = 5.0 \times 10^5\,s^{-1}$, which is determined by fitting the off-resonance enhancement in Figure 5.11.

5.4.1 IR Power Dependence

The characteristics of the dynamics for a range of IR excitation powers are seen in Figure 5.7. In all cases there is an initial emission enhancement associated with excitation to ITE level 3 and subsequent decay with a lifetime around 70 μs. Since this initial decay is faster than either of the radiative rates of the ITE energy levels (which are around 400 μs and 8 ms) it must be directly related to the predominantly non-radiative relaxation of ITE level 3 to 2 (W_{32}). After about 200 μs, the levels are in thermal equilibrium. For the purposes of comparing the magnitude of enhancement, all of the transients presented

Table 5.4 Comparison of indicated and modeled temperature for a range of IR powers.

IR power ($J\,cm^{-2}$)	0.2	0.3	1.7	5.1	8.5	17
Site S_a model temperature (K)	8	8	9	10	11	13
Site S_b model temperature (K)	8	8	14	14	16	17

in Figures 5.7–5.11 have been normalized so that the emission intensity prior to the IR pulse is the same.

Since the spectral deconvolution in Figure 5.2 shows emission from site S_b is less intense than from site S_a, the contribution of emission from site S_a at emission 2 must be taken into account when analysing the dynamics of site S_b. To model the IR-induced enhancement at emission 2 (400 nm) in Figures 5.7–5.11 the intensity is calculated as 64% from site S_b and 36% from site S_a.

Figure 5.7 shows the variation of the photoluminescence enhancement as the time-averaged 952 cm^{-1} IR energy density is varied from 0.2–17 $J\,cm^{-2}$. After more than about 200 μs the decay can be described by a single exponential function with a lifetime that is proportional to the relative population in the higher and lower ITE states (2) and (3). Increased population in the higher exciton state is then caused by an overall increase in lattice temperature leading to an increase in the non-radiative rate beween the lower and higher exciton states (W_{23} increases). The temperature of the site can be found from the radiative lifetime of the emission after 200 μs assuming radiative rates and energy level difference calculated from temperature dependence of lifetime are correct. The temperature is found to increase with increasing IR power (see Table 5.4) so the IR pulse must heat the sample. The change in temperature is different for the two sites, so the heating is local and depends on the charge-compensation geometry.

At very low IR power, the difference between the indicated and predicted temperatures is due to imprecision in the physical temperature measurement. In our experimental setup it is not practical to measure the temperature of the samples directly so the nominal temperatures listed in Table 5.7 are measured at the top of the cryostat cold-finger. The temperature at the top of the cold-finger does not exactly correspond to the temperature of the sample. At 5 K there is a difference between the top of the cold-finger and the sample of 3 K. As nominal temperature increases, this offset between the top of the cold finger and the sample diminishes.

The rate equation model was allowed to run on all the experimental transients where IR

energy density was varied. Optimum values of the rate equation parameters were obtained from the fits with F_{25}, F_{TC} and W_{32} being allowed to vary. The optimal values of the varied parameters are shown in Figure 5.8. By considering a parameter dependence on IR energy density that makes physical sense a series of phenomenological equations were developed. They are Equations 5.10–5.12.

The parameter F_{24} increases linearly with IR energy density, as expected since F_{24} is a mechanism driven by the IR excitation.

$$F_{24} = F_{24}^{m} \frac{P}{P_{\max}}, \tag{5.10}$$

where P represents the time-averaged IR energy density. $P_{\max}$ is the maximum IR energy density, 17 $\mathrm{J\,cm^{-2}}$.

F_{TC} becomes saturated with IR energy density, indicating that the IR excitation creates close to the maximum amount of excitons from trap liberation even at low powers.

$$F_{TC} = F_{TC}^{i} \left(1 - \exp\left(-\xi_{TC} \frac{P}{P_{\max}}\right)\right). \tag{5.11}$$

The emission decay in the first 100 μs after the IR pulse is noticeably faster as the IR energy density is decreased. To model this, the non-radiative rate between the higher and lower excitonic states W_{32} decreases as power is increased. This is unusual in light of the increase in lattice temperature. It can be modelled in terms of the model temperature T_m:

$$W_{32} = W_{32}^{0} \exp\left(-\delta_{32} T_m\right) + c_{32}. \tag{5.12}$$

Table 5.5 lists the values used in eqns 5.10–5.12 to generate parameters for the rate equations used to calculate the black transients in Figure 5.7. ξ_{TC} is greater for centre S_b which means that the rate at which saturation occurs is faster for the centre S_b configuration. There are many types of electron traps in $NaMgF_3$ so it is possible that the electrons that create ITEs are liberated from different types of traps, or the configuration of centre S_b is such that more liberated electrons combine with centre S_b impurities as IR power is increased than at centre S_a impurities. To study the details of electron traps in $NaMgF_3$ very precise temperature dependencies are needed and the details of the centre configuration also require careful analysis.

W_{32}^{0} is higher for centre S_a than centre S_b, but both values are very large. The slow rate of thermal equilibrium between the two ITE levels could be because there are few phonons at the low energy between levels 2 and 3.

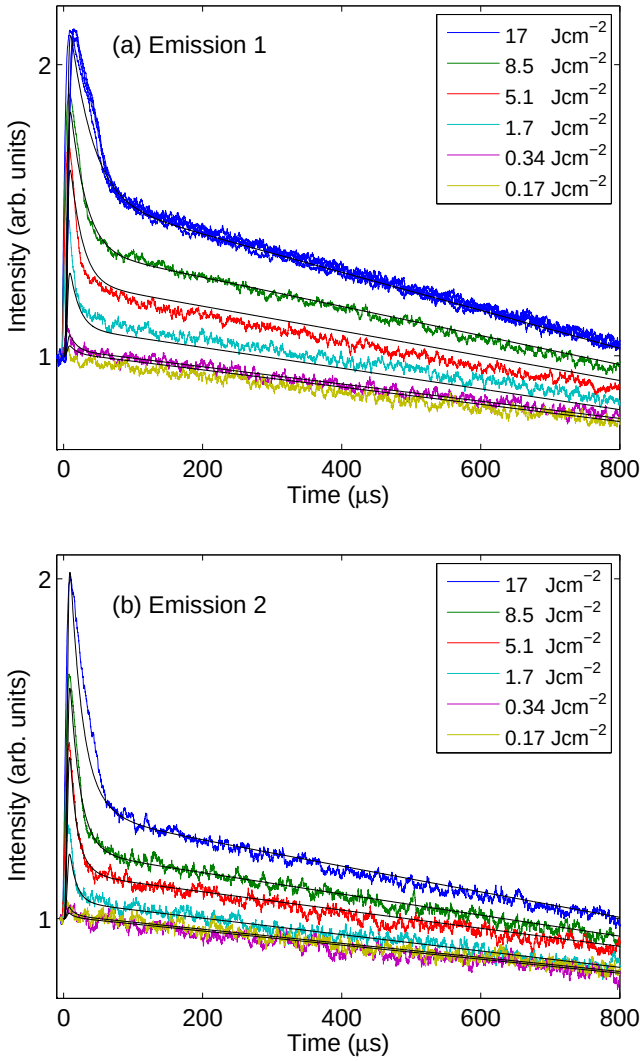

Figure 5.7 IR power-dependent dynamics of the IR enhancement of two sites of $NaMgF_3:Yb^{2+}$ already excited with a 300 nm pre-pulse at a nominal temperature of 5 K. The IR excitation is 952 cm^{-1} at 0 s. The black lines are calculated from the rate equation model with parameters listed in Table 5.5.(a) Emission monitored at 21 000 cm^{-1} and entirely from site S_a. There are 3 blue lines, taken at different times but with the same temperature, UV and IR power, showing the variation in signal over the course of the experiment. (b) Emission monitored at 25 000 cm^{-1} and predominantly from site S_b.

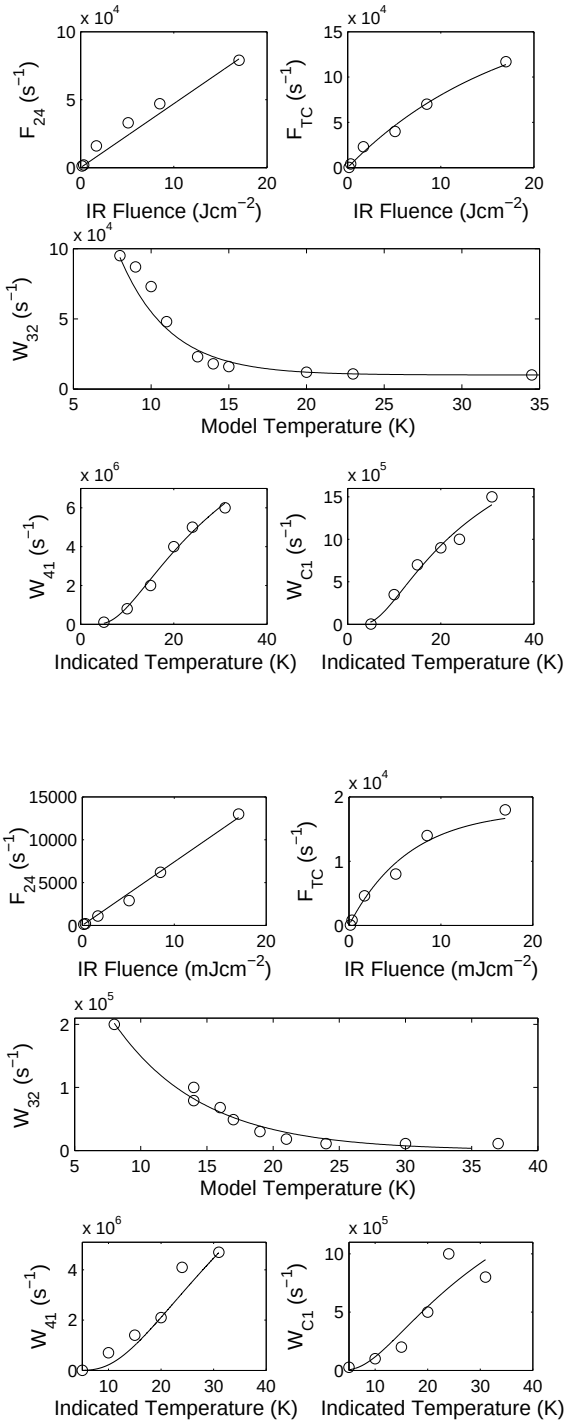

Figure 5.8 The parameter values for the transients varying with IR fluence and temperature. The circles are the optimal values of the parameters used to model the transients in Figs. 5.7 and 5.9 and the lines are the fits to those values, described in the Equations5.10–5.14.

Table 5.5 The values for Equations 5.10–5.12 that were found by fitting the change optimal rate equation parameters with IR fluence in figure Figure 5.8.

	Center S_a	Center S_b
F^i_{TC} (s^{-1})	$(1.80 \pm 0.01) \times 10^5$	$(1.8 \pm 0.1) \times 10^4$
ξ_{TC}	1.00 ± 0.08	2.6 ± 0.1
W_{C1} (s^{-1})	$(2.7 \pm 0.1) \times 10^4$	$(2.5 \pm 0.1) \times 10^3$
F^m_{24} (s^{-1})	$(8.00 \pm 0.04) \times 10^4$	$(1.4 \pm 0.3) \times 10^4$
W_{41} (s^{-1})	$(1.10 \pm 0.06) \times 10^5$	$(2.5 \pm 0.2) \times 10^3$
W^0_{32} (s^{-1})	$(1.0 \pm 0.3) \times 10^6$	$(6.7 \pm 0.5) \times 10^5$
δ_{32} (K^{-1})	0.31 ± 0.04	0.15 ± 0.05
c_{32} (s^{-1})	$(1.0 \pm 0.4) \times 10^4$	$((0 \pm 2) \times 10^3)$

Table 5.6 Comparison of the modeled temperatures used to calculate the emission dynamics for a range of indicated temperatures (shown in Figure 5.9). Uncertainties in model temperature are approximately 0.5 K.

Indicated temperature (K)	4.9	10	15	20	24	31
Center S_a model temperature (K)	13	14	15	20	23	34
Center S_b model temperature (K)	17	19	21	24	30	37

5.4.2 Temperature Dependence

As the temperature is increased there is less enhancement in emission, since there is more population in the upper ITE state and the IR pulse redistributes less population. In Figure 5.9 the increase in temperature causes a decrease in initial enhancement and an increase in the slope after 200 μs.

Table 5.6 compares the temperature indicated in the experiment to the temperature used in the rate equation model to generate the black transients in Figure 5.9. The model temperature is determined by the decay rate of the transient more than 200 μs after the IR excitation. When the indicated crystal temperature is 4.9 K, centre S_b has a model temperature of 17 K. This 12 K offset is consistent with the apparent strong IR absorption for this configuration. This absorption is characterised by a large rise in the model temperature with higher average IR energy density.

Equations 5.13–5.14 describe the trends in the rate equation parameters that vary with temperature. The rate of non-radiative loss from the higher excitonic levels W_{41} increases

Table 5.7 The values for Equations 5.13–5.14 that were found by fitting the change optimal rate equation parameters with temperature in figure Figure 5.8.

	Center S_a	Center S_b
F_{TC} (s^{-1})	$(1.2\pm0.1) \times 10^5$	$(2.8\pm0.8) \times 10^4$
W^0_{C1} (s^{-1})	$(3.00\pm0.05) \times 10^6$	$(2.6\pm0.2) \times 10^6$
ϵ_{C1} (cm^{-1})	17.0 ± 0.2	22.0 ± 0.1
F_{24} (s^{-1})	$(7.90\pm0.04) \times 10^4$	$(1.3\pm0.4) \times 10^4$
W^0_{41} (s^{-1})	$(1.6\pm0.2) \times 10^7$	$(2.0\pm0.3) \times 10^7$
ϵ_{41} (cm^{-1})	20.0 ± 0.3	31 ± 3

with temperature. The thermal barrier is modeled with an Arrhenius function:

$$W_{41} = W^0_{41} \exp\left(\frac{-\epsilon_{41}}{kT_i}\right), \tag{5.13}$$

where T_i represents the indicated temperature. T_i is used rather than the model temperature because the conduction band will be at the temperature of the bulk crystal rather than the local temperature of the ITEs. Similarly there is non-radiative loss in the trap process W_{C1}.

$$W_{C1} = W^0_{C1} \exp\left(\frac{-\epsilon_{C1}}{kT_i}\right). \tag{5.14}$$

Table 5.7 lists the values found by fitting the Equations 5.13–5.14 to the optimal parameters for the rate equations, used to calculate the black transients in Figure 5.9.

The parameter F_{24} remains constant because the IR energy density is constant. The non-radiative rate between the excitonic states W_{32} decreases with increasing model temperature, following the dependence on model temperature as in equation 5.12. This trend is consistent with the results obtained when varying the IR energy density illustrated in Equation 5.12.

To test the model, emission was also measured over the same range of temperatures for a lower IR power (5.1 $J\,cm^{-2}$) in Figure 5.10. The temperatures were fitted from the decay rate after 300 μs and parameters calculated from equations 5.13–5.14. The predicted dynamics in Figure 5.10 reasonably match the recorded emission decay. There is some discrepancy in Figure 5.10(a) between 10 and 20 K, but the model predictions match well for the lowest and highest temperatures, indicating the trends are roughly correct with some fine detail of the dynamical processes not taken into account by the model.

In Senanayake's work on the dynamics of ITE levels in SrF_2:Yb^{2+}, [29] a more complex

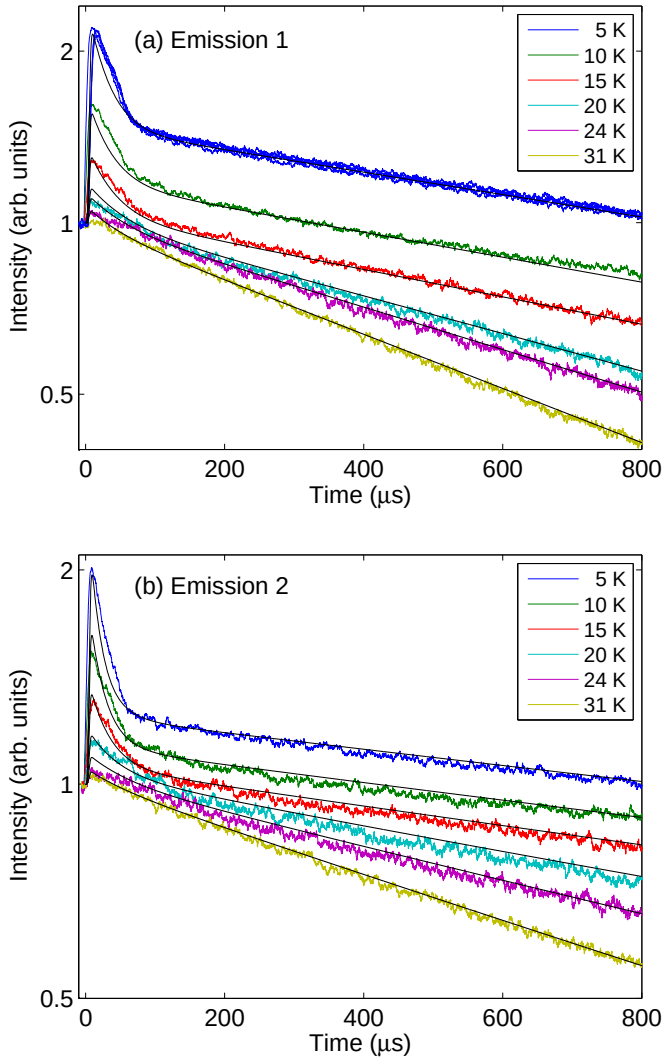

Figure 5.9 Temperature-dependent dynamics of the IR enhancement of two sites of $NaMgF_3$:Yb^{2+} already excited with a 33 000 cm^{-1} pre-pulse. The IR excitation is 17 J cm^{-2} and 952 cm^{-1} at 0 s. The black lines are calculated from the rate equation model with parameters listed in Table 5.7. (a) Emission monitored at 21 000 cm^{-1} and entirely from site S_a. There are 3 blue lines, taken at different times but with the same temperature, UV and IR power, showing the variation in signal over the course of the experiment. (b) Emission monitored at 25 000 cm^{-1} and predominantly from site S_b.

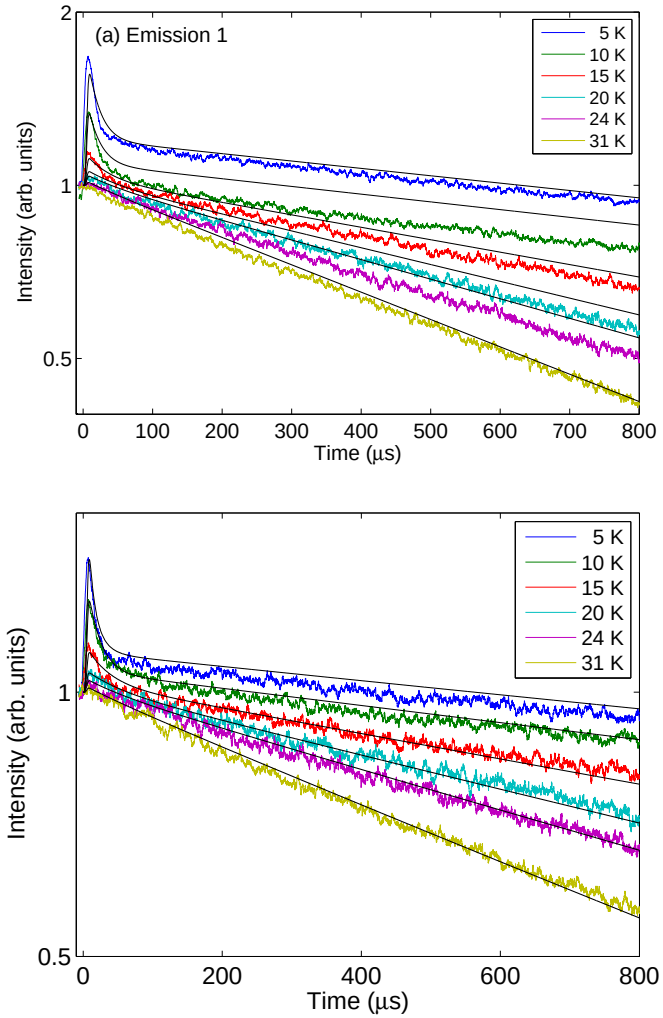

Figure 5.10 Temperature-dependent dynamics of the IR enhancement of two sites of $NaMgF_3$:Yb^{2+} already excited with a 33 000 cm^{-1} pre-pulse. The IR excitation is 5.1 J cm^{-2} and 952 cm^{-1} at 0 s. The black lines are calculated from the rate equation model with parameters listed in Table 5.7. (a) Emission monitored at 21 000 cm^{-1} and entirely from site S_a. (b) Emission monitored at 25 000 cm^{-1} and predominantly from site S_b.

heating model was used. This model was applied to $NaMgF_3$:Yb^{2+} but was not able to explain the emission seen in Figures 5.7–5.10 as accurately as the model presented above.

Senanayake's heating model involves calculating the temperature of the Yb^{2+} site at every point in time, and then adjusting the temperature-dependant rates accordingly. The heat equation must be solved iteratively, with the correct heat capacity c and thermal conductivity k for the material at the previous temperature. In the temperature range of the experiments (5 K–30 K) the values of c and k vary dramatically with temperature, so having accurate temperature dependence of c and k for the material is very important. Unfortunately these properties have not been published for $NaMgF_3$. The model was applied to $NaMgF_3$:Yb^{2+} with values of c and k for SrF_2 and CaF_2, but in order to achieve a temperature that gave the correct slope several hundred μs after the IR excitation, the temperature would be too high tens of μs after the IR excitation and cause the initial decay to be too long.

The success of assuming a constant temperature indicates that the heating effect of IR absorption is cumulative over many IR pulses.

5.4.3 Wavelength Dependence

Figure 5.11 shows the photoluminescence enhancement as a function of IR excitation wavelength between 5-12 μm. When the IR wavelength is 5 μm there is no intra-excitonic excitation, so there is no fast emission from the higher exciton state. As the IR wavelength is increased it becomes resonant with a difference in energy levels of the exciton and the enhancement caused by IR excitation increases. To model this resonance, the rate of trap liberation and the rate that the higher energy exciton level is populated increase with decreasing wavelength – shown in Table 5.8. As the IR wavelength is moved off the peak of the enhancement, the lifetime of the fast decay component becomes shorter.

In the model, the temperature is 20 K for site S_a and 25 K for site S_b. The emission in Figure 5.11 was measured in unavoidably different experimental conditions from Figures 5.7 and 5.9. Since the IR beam will illuminate a different area of the sample the amount of heating the IR excitation causes will be affected. The temperature is higher for site S_b than for site S_a, which is consistent with the site-dependent trends in heating given in Table 5.4. The rates that are not in Table 5.8 do not change with IR wavelength and have the same values as used for modeling the 5 K full IR power curve (listed in Table 5.5).

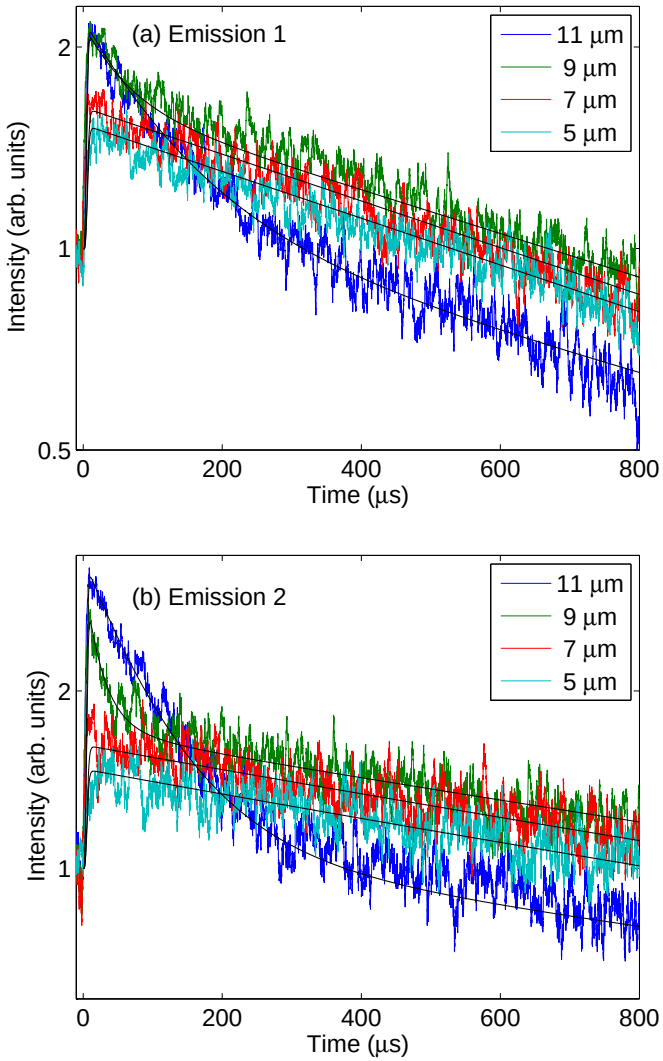

Figure 5.11 Infrared wavelength dependence of the photoluminescence enhancement at 8 K. The black lines are calculated from the rate equation model with parameters listed in Table 5.8. (a) Emission monitored at 21 000 cm^{-1} and entirely from site S_a. (b) Emission monitored at 25 000 cm^{-1} and predominantly from site S_b.

Table 5.8 Parameter values for the rate equation model as a function of IR wavelength. The emission calculated from these parameters is shown in Figure 5.11.

Site S_a			
IR Wavelength (μm)	F_{T4} (s^{-1})	W_{32} (s^{-1})	F_{25} (s^{-1})
11	1.2×10^5	4.0×10^3	2.5×10^5
9	2.5×10^5	1.0×10^4	2.0×10^5
7	1.8×10^5	1.0×10^6	1.0×10^4
5	1.5×10^5	1.1×10^6	1.0×10^4
Site S_b			
IR Wavelength (μm)	F_{T4} (s^{-1})	W_{32} (s^{-1})	F_{25} (s^{-1})
11	5.0×10^4	7.0×10^3	1.0×10^4
9	2.0×10^5	3.0×10^4	1.0×10^4
7	1.8×10^5	1.0×10^6	2.4×10^4
5	1.3×10^5	1.0×10^6	4.2×10^4

5.4.4 UV Power Dependence

The photoluminescence enhancement was also studied as the UV excitation energy was reduced from 70 to 5 mJ cm^{-2}. After normalising the intensity of the transient to a point just before the IR enhancement, we see that the IR-induced photoluminescence enhancement does not have a strong dependence on the UV excitation density. In Figure 5.12 the UV power is reduced by an order of magnitude but the normalised enhancement is only decreased by 20%.

5.4.5 Trap Liberation

The trap liberation term F_{T4} in the model is essential to fitting the experimental data. The fractional contribution to the total emission induced by the trap liberation process can be estimated from the spectrum by taking the difference between the intensity just before the IR pulse (I_i) and at a long time (8 ms) after the IR pulse (I_f). We must also subtract the number of photons emitted from the excitonic states in this time period, which will be equal to the integral of the intensity between I_i and I_f. This calculation assumes that the temperature (and so the relative population of the ITE states 2 and 3) is the same before and several hundred microseconds after the IR pulse as the site heating is a cumulative effect over many IR pulses. Some additional population is lost from the

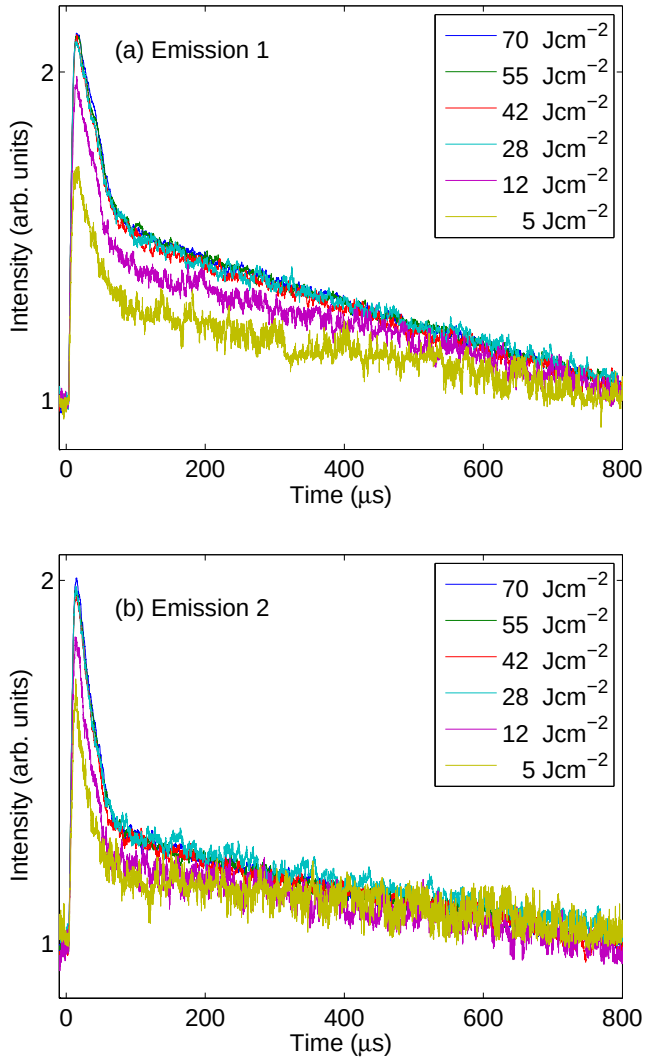

Figure 5.12 The photoluminescence enhancement of $NaMgF_3$:Yb^{2+} as the power of the ultraviolet 33 000 cm^{-1} pre-pulse is changed. The sample temperature is 8 K. IR excitation is at 952 cm^{-1}. The traces have been normalized for the UV power difference (a) Emission monitored at 21 000 cm^{-1} and entirely from site S_a. (b) Emission monitored at 25 000 cm^{-1} and predominantly from site S_b.

non-radiative decay from the upper ITE levels W_{51}, but it is negligible compared to the radiative loss.

$$\frac{I_{\text{trap}}}{I_2} = I_f - I_i - \int_{I_i}^{I_f} I dt \tag{5.15}$$

The estimated trap population over the wavelength range calculated from Equation 5.15 is shown in Figure 5.13. All three emission wavelengths have similar trap liberation spectra so the trap distribution must be similar at both sites. The same shape is seen in the long time emission intensity and the integrated intensity for both sites. The trap population calculated from the mixed emission at 23 300 cm^{-1} consists of two overlapping regions, calculated from two seperate emission scans (one from 500 to 900 cm^{-1} and another from 830 to 2000 cm^{-1}) normalized and plotted together. The wider range of excitation energies for the 23 300 cm^{-1} peak shows emission continuing to decrease as the excitation energy is lowered.

The trap liberation spectrum of $NaMgF_3$:Yb^{2+} is different from that of MgF_2:Yb^{2+} [33]. In MgF_2:Yb^{2+} the integrated emission remains constant with IR frequency and only reduces at high frequencies when FEL power drops. This indicates that the traps are different from those formed in MgF_2. The trap liberation spectrum of $NaMgF_3$:Yb^{2+} is similar to that of CaF_2:Yb^{2+} [28] but the traps are deeper. Figure 5.13 indicates the traps in $NaMgF_3$:Yb^{2+} have an approximate depth of 800 cm^{-1} compared to 400 cm^{-1} in CaF_2 and SrF_2 [100].

5.5 Conclusion

Site-selective transient photoluminescence enhancement has been measured in multi-site $NaMgF_3$:Yb^{2+}. Enhanced emission from impurity-trapped exciton states and electron trap liberation in both sites of $NaMgF_3$:Yb^{2+} is observed. The dynamics of the emission have been analysed in terms of a multi-level rate equation model and compared for both sites. The dominant process that contributes to the dynamical behaviour is intra-excitonic absorption and relaxation between three ITE levels. The exciton energy levels have been determined – two are only tens of wavenumbers apart and one is 950 cm^{-1} from the exciton ground state. The model shows electron trap liberation is an important menchanism to increase population. The electron trap depth is found to be approximately 800 cm^{-1} by analysing the difference in emission intensity before and after the IR pulse. A moderate

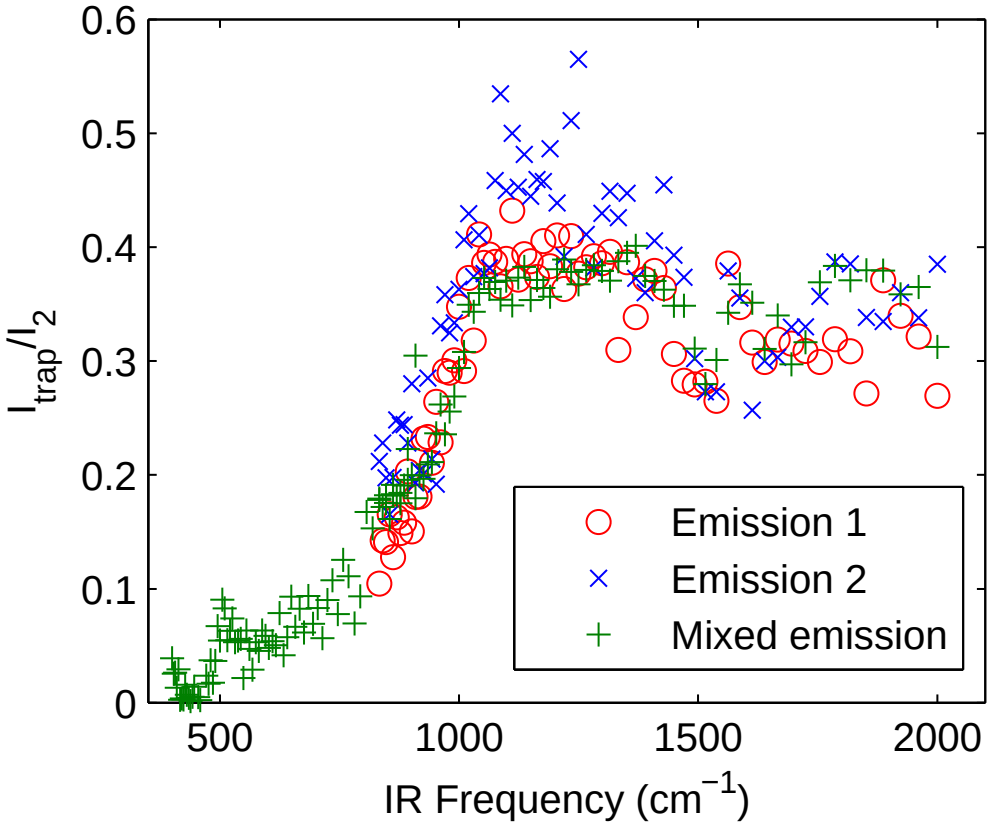

Figure 5.13 The trap population calculated from Equation 5.15 for three emission energies. The green points are from signal monitored in the middle of the emission band at 23 300 cm^{-1}. The emission at 23 300 cm^{-1} has been separately measured for a lower energy region (from 500 to 900 cm^{-1}) and normalized. Mixed emission refers to the signal monitored at the centre of the emission band at 23 300 cm^{-1}.

increase in lattice temperature is inferred from the modelling. The detailed analysis of the temporal emission is relevant to understanding the dynamical behaviour of impurity-trapped excitons in many scintillator materials.

Chapter 6

Vacuum Ultraviolet Spectroscopy

The fluoride materials described in earlier chapters all have bandgaps of the order of ten electron volts, which is in the vacuum ultraviolet (VUV) energy range. This chapter presents the results of time-resolved spectroscopic experiments performed upon excitation of CaF_2:Yb, $NaMgF_3$:Yb and MgF_2:Yb single crystals with UV-VUV synchrotron radiation at the SUPERLUMI station at Hamburger Synchrotronstrahlungslabor (HASYLAB) in Hamburg, Germany [81]. The bandgap spectroscopy of insulating crystals such as these have not been well-investigated due to the limited number of available excitation sources with the necessary energy range.

The theory of excitons is well-developed for loosely-bound Wannier-Mott excitons which form in semiconductor materials. Wannier-Mott excitons have binding energies of the order 100 cm^{-1} and typically occur in materials with bandgaps of a few thousand cm^{-1}. Systematic studies of visible spectroscopy have been performed for these kind of intrinsic excitons in semiconductors [101]. Conversely, the tightly-bound Frenkel excitons which occur in insulators require high energy excitation in the VUV region. VUV lasers have only recently been developed [102] and the only other sources of intense VUV light are synchrotrons with VUV beamlines [81]. Because of this, less systematic studies of excitons in insulating materials have been achieved compared to semiconductor excitons.

In this thesis SUPERLUMI is utilised as a tunable VUV excitation source to excite intrinsic excitons in fluoride materials. The excitation and emission spectra of the crystals are presented, giving information on the energy of the intrinsic excitons and the self-trapped exciton states that subsequently form. The spectra are compared to give insight into the formation and decay of Frenkel excitons in different fluoride crystals.

In all three materials, excitation into the $4f^{13}5d$ states of Yb^{2+} in the crystals results in emission from ITE or $4f^{13}5d$ configurations. For $NaMgF_3$:Yb^{2+} the excitation measurements are interpreted using a semi-empirical crystal field model. Excitation into the

fundamental absorption band of the crystals results in emission from intrinsic states and Yb impurity centres. The interplay between intrinsic distortions and Yb impurity centres is observed and analysed with changing excitation energy and temperature.

6.1 CaF_2:Yb

CaF_2 is a commonly used optical material. It has a very low dispersion and is characterised by outstanding radiation hardness, making it useful for lenses and windows [103]. It also has an extremely large bandgap, which makes it a suitable host for studying the excited state structure of lanthanide dopants. As with many metal halides excited with high energy radiation, CaF_2 forms free excitons that are captured within picoseconds to become STEs [10]. The STEs can decay radiatively or non-radiatively. The non-radiative decay of an STE can be associated with the transferal of the STE to a permanent defect, or energy transfer to an impurity ion. The subsequent relaxation of the impurity ion is an internal process that is dependent on electronic structure of the ion, absolute location of its energy levels relative to the conduction band and valence band, temperature, energy of the lattice phonons and concentration of the ions. In the case of CaF_2:Yb the most probable path for relaxation of excited states of Yb^{2+} ions is the formation of an ITE. The existence of both ITE and STE emission from the crystal allows a comparative study of spectroscopic and dynamic properties of two fundamentally different types of exciton.

This section gives results of time-resolved spectroscopic experiments performed upon excitation of a CaF_2:Yb single crystal with UV-VUV synchrotron radiation, both below and above the CaF_2 band edge. Excitation into the Yb^{2+} $4f^{13}5d$ states results in ITE emission. For high energy excitation around the band edge, STE emission is observed. Evidence of energy transfer from the STE to the ITE, possibly via the Yb^{2+} $4f^{13}5d$ states, is presented.

6.1.1 Emission and Excitation Measurements of CaF_2

Figure 6.1 shows the 8 K time-integrated and time-resolved emission spectra of CaF_2:0.05%Yb^{2+} recorded upon selective excitation at 101 000, 57 100, and 87 700 cm^{-1}. Excitation above the bandgap (at 101 000 cm^{-1}) results in emission centred near 34 400 cm^{-1}, which originates from radiative relaxation from STE states [48]. When exciting into a $5d$ state well below the bandgap (in this case at 57 100 cm^{-1}), the dominant feature in emission is a

broad band occuring between 15 000 to 22 000 cm^{-1}, previously identified as ITE emission [26]. At 87 700 cm^{-1} excitation the ITE and STE emission bands are both present.

The peak at 87 700 cm^{-1} in the excitation spectrum (see below) corresponds to the optical formation of free excitons in CaF_2. The free exciton decays into a STE within picoseconds [10]. For 87 700 cm^{-1} excitation, the observation of emission from both the ITE and STE indicates the existence of energy transfer between host electronic excitations and the ITE that is associated with the presence of Yb^{2+}. Since the lifetime of the free exciton is of the order of picoseconds, it seems unlikely that the free exciton can travel to an Yb impurity to create an ITE, so all free excitons must decay to STEs and then some fraction of the STEs will be close enough to Yb^{2+} ions to transfer energy to Yb^{2+} ions and create ITEs. Figure 6.2 shows a schematic of this energy transfer mechanism. We expect a greater emission intensity from the STE band than the ITE band as an ITE must be localised around an H-F pair close to an impurity. Thus most STEs will radiatively recombine rather than relaxing to an ITE.

In Figure 6.3 the ITE emission in CaF_2:Yb^{2+} quenches when the sample is excited in the VUV at room temperature. The ITE emission is known to quench when excited into a Yb^{2+} $5d$ level at temperatures higher than 200 K [26]. The change in shape of the higher energy band with temperature indicates that the singlet emission from the STE is also quenched at room temperature.

The time-resolved spectra demonstrate spectrally-separated components of STE emission (Figure 6.1(c)). The spectrum recorded within the slow time gate contains an emission band centred near 35 500 cm^{-1} that closely follows the time-integrated spectrum and corresponds to the triplet state of STE. In turn, the spectrum recorded within the fast time gate demonstrates an emission band shifted towards lower energy by about 4000 cm^{-1}. The lower energy emission band corresponds to radiative relaxation of the STE singlet state [55]. The decay of the singlet STE state is shown in the inset to Figure 6.1(b). The measured decay is non-exponential, however an effective lifetime of $\tau \approx 10$ ns can be estimated. The lifetime of the triplet state is much longer than the time between synchrotron bunches (480 ns).

Figure 6.4 shows the 8 K excitation spectra recorded monitoring the ITE and STE emission peaks in Figure 6.1. The spectra indicate STE emission is excited with two features. The feature at 87 000 cm^{-1} represents the free exciton absorption and at 94 000 cm^{-1} is the onset of intra-band absorption. The peak at 87 000 cm^{-1} is at a lower energy than the free exciton peak in reflection measurements, measured to be at 90 300 cm^{-1}

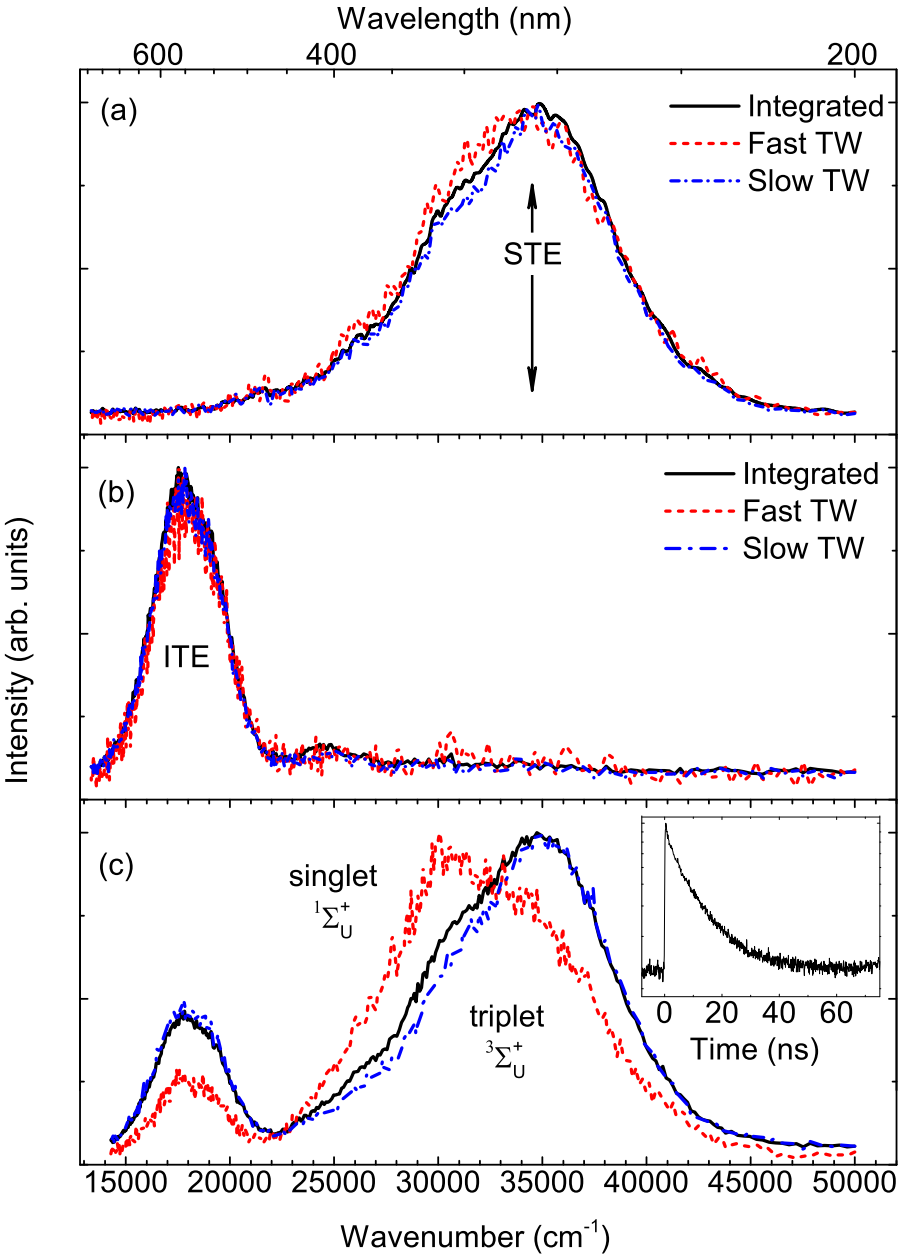

Figure 6.1 Emission from CaF_2:0.1%Yb at a sample temperature of 8 K. (a) Above bandgap excitation at 101 000 cm^{-1}, (b) excitation into a Yb^{2+} excited state at 57 100 cm^{-1}, (c) excitation into the free exciton peak at 87 700 cm^{-1}. Inset shows the log of the intensity of 28 600 cm^{-1} emission after excitation at 87 700 cm^{-1}. The measured decay is non-exponential and prodominantly from the STE singlet state. Dotted red lines are integrated over the fast time window (2–9 ns) and blue lines are integrated over the slow time window (46–70 ns).

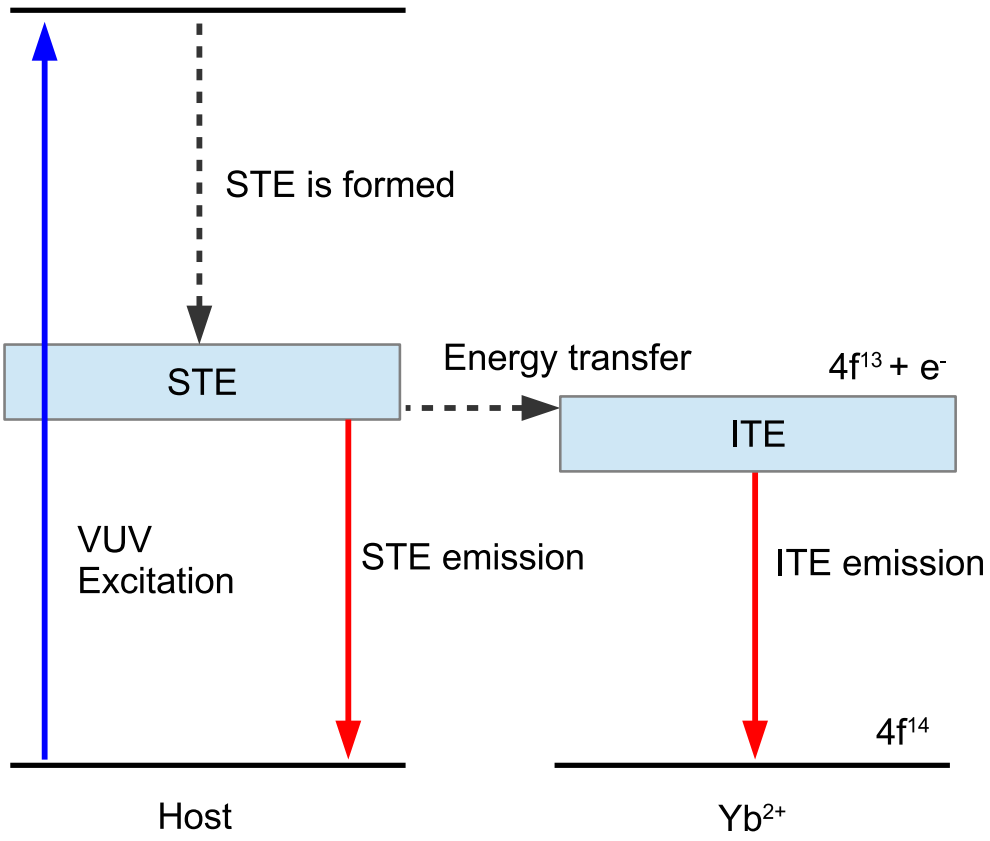

Figure 6.2 Schematic of the VUV spectroscopy measurement. The VUV excitation creates a self-trapped exciton, which we observe decaying radiatively or transferring energy to an impurity-trapped exciton state.

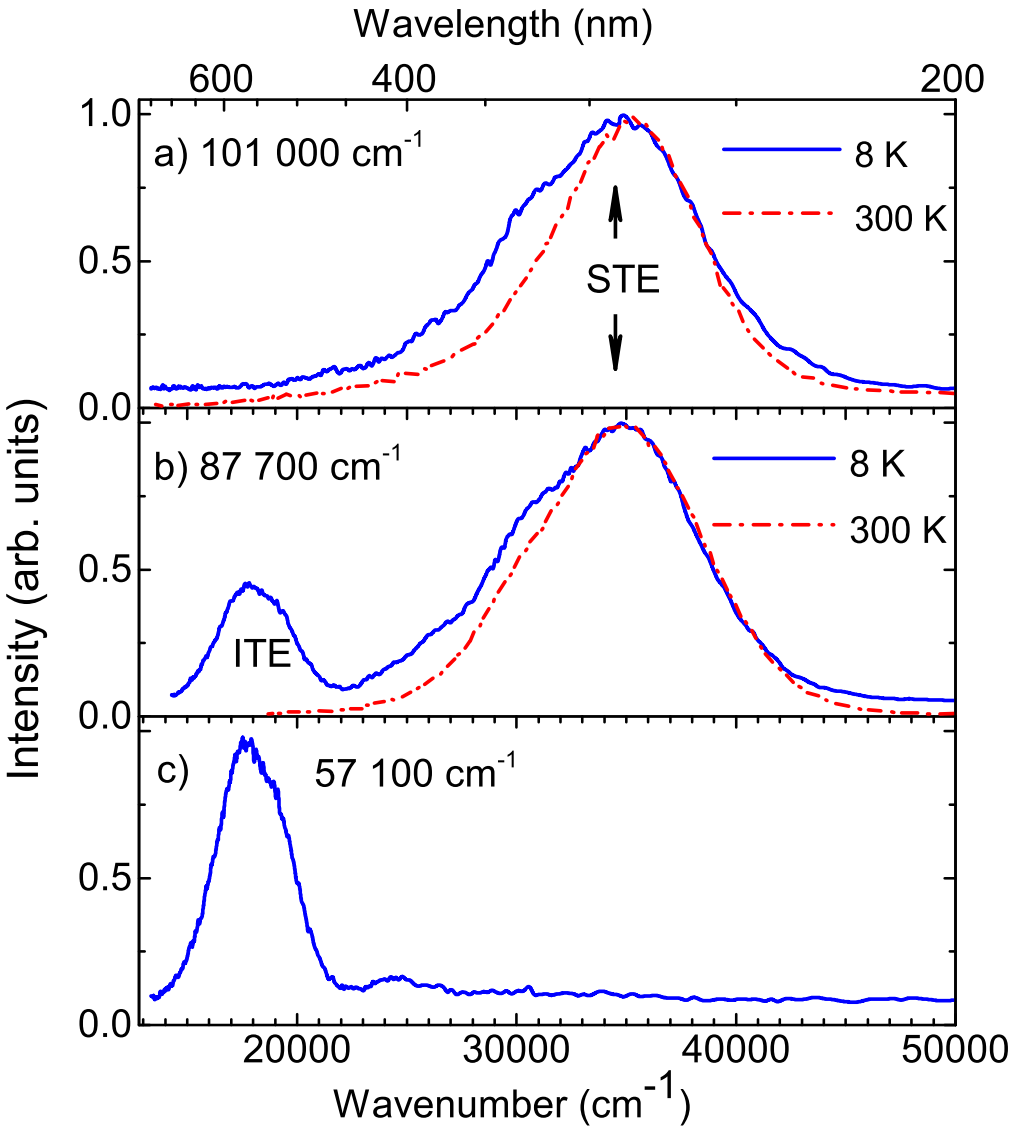

Figure 6.3 Emission from CaF_2:0.1%Yb at a sample temperature of 8 K and 300 K. (a) Above bandgap excitation at 101 000 cm^{-1}, (b) excitation into the free exciton peak at 87 700 cm^{-1}. (c) below bandgap excitation at 57 100 cm^{-1}. No signal was found for this excitation frequency when the sample temperature was 300 K.

[104, 105], but corresponds well with the free exciton excitation transition for undoped CaF_2 at 85 K [106]. It it noteworthy that the emission intensity is severely attenuated for excitation energy above 100 000 cm^{-1}. This is due to the very high absorption coefficient of band-to-band transitions, resulting in excitons prodominantly created near the surface and thus subject to quenching from surface defects preventing STEs being formed. Such surface effects have been recognized in STE emission by Denks et al. who observed similar attenuation for interband excitation [106].

As indicated by the peaks below 60 000 cm^{-1} in the black spectrum in Figure 6.4, emission from the ITE is observed upon excitation into the $4f^{13}5d^1$ states of the Yb^{2+} ion in a resonant process. The peak around 90 300 cm^{-1} in the black spectrum in Figure 6.4 indicates that ITE states can be populated from host ionic states although there is a 1500 cm^{-1} red shift for the free exciton transition compared to the STE detection (see inset). The bulk free exciton transition can be seen as a shoulder on the edge of the ITE emission. Since the free exciton lifetime is very short, it is reasonable to assume that free excitons must be generated in the physical region of the Yb^{2+} impurity in order to decay into ITE systems. Thus it is likely that there is a perturbed crystal enviroment sufficient to slightly change the energy of the resonant transition of the free exciton absorption. The presence of the shoulder at the "bulk" free exciton energy indicates the process of ITE generation through the path of "free exciton to STE to ITE" occurs.

An alternative explanation of this small shift in the excitation spectra might be associated with saturation of available Yb^{2+} impurity sites arising from the very small penetration depths in this excitation region. As the penetration depth decreases drastically at the onset of free exciton absorption, Yb^{2+} sites within range of free excitons decrease, leading to quenching of the saturated ITE emission and the red shift of the free exciton peak when monitoring ITE emission.

The excitation spectrum that was recorded monitoring emission from the ITE shows a peak at 75 000 cm^{-1}, just below the free exciton absorption. This peak is not a high-energy Yb^{2+} level, as the crystal field analysis shows there are no such states, nor is it likely to be related to the intrinsic CaF_2 exciton. The peak at 75 000 cm^{-1} is most likely to be a Yb^{3+} charge transfer band. An absorption peak due to charge transfer from Yb^{3+} to F^- has been identified at 70 200 cm^{-1} for a CaF_2:Yb^{3+} sample at room temperature, and would be expected to shift to higher energy at a lower temperature [34, 107].

The excitation features of CaF_2:Yb depend on the concentration of Yb dopant, as shown in Figure 6.5 where ITE emission is monitored at a sample temperature of 8 K. The

excitation peaks are distorted as Yb concentration is increased from 0.01% to 2%. The intrinsic exciton peak at 87 000 cm^{-1} broadens and decreases in intensity compared to the intra-configurational Yb transitions below 60 000 cm^{-1}. In Figure 6.6 STE emission is quenched with increased concentration. The increase in concentration of Yb centres means that the intrinsic excitons are much more likely to relax into STE states near Yb ions and transfer energy to ITEs.

6.1.2 Temperature Dependence of CaF_2 Free Exciton Peak

Figure 6.7 shows the position of the free exciton excitation peak as a function of temperature, obtained by monitoring the ITE and STE emission. The free exciton peak is clearly observed to be red-shifted as the temperature increases. We interpret this in terms of a model developed to describe the shift in bandgap of semiconductors, Viña's equation. Viña's equation is an alternative to the commonly used Varshni's equation as it has a more physical basis and has been shown to better fit the low temperature behaviour of semiconductors [108, 109]. Viña's equation is given as [110]:

$$E_{\mathrm{g}}(T) = E_{\mathrm{p}}(0) - \frac{\alpha\theta}{\exp(\theta/T) - 1}, \tag{6.1}$$

where $E_{\mathrm{p}}(0)$ is usually the bandgap at absolute zero, but in our case is the STE peak emission energy at absolute zero; θ is the mean phonon temperature; and α is related to the electron-phonon interaction. The data and best fits are shown in Figure 6.8. We determine best fit values of $E_{\mathrm{p}}(0) = 87\,200$ cm^{-1}, $\alpha = 15$ $cm^{-1}K^{-1}$ and $\theta = 306$ K. An identical effect is observed when monitoring the ITE emission peak albeit over a limited range of temperatures owing to the thermal quenching of the ITE emission. The best fit values from fitting the ITE emission are $E_{\mathrm{p}}(0) = 86\,200$ cm^{-1}, $\alpha = 10$ $cm^{-1}K^{-1}$ and $\theta =$ 131 K. θ is determined by the host material and should not change between ITE and STE emission.

The change in θ is not simply a fitting effect, as demonstrated in Figure 6.8. The curve which is constructed using the parameters fitted to the STE data does not fit the ITE data when $E_{\mathrm{p}}(0)$ is reduced without changing θ. The difference in the θ between the two emission energies supports the theory discussed above, that the peak position is not the true absorption maximum due to surface quenching effects.

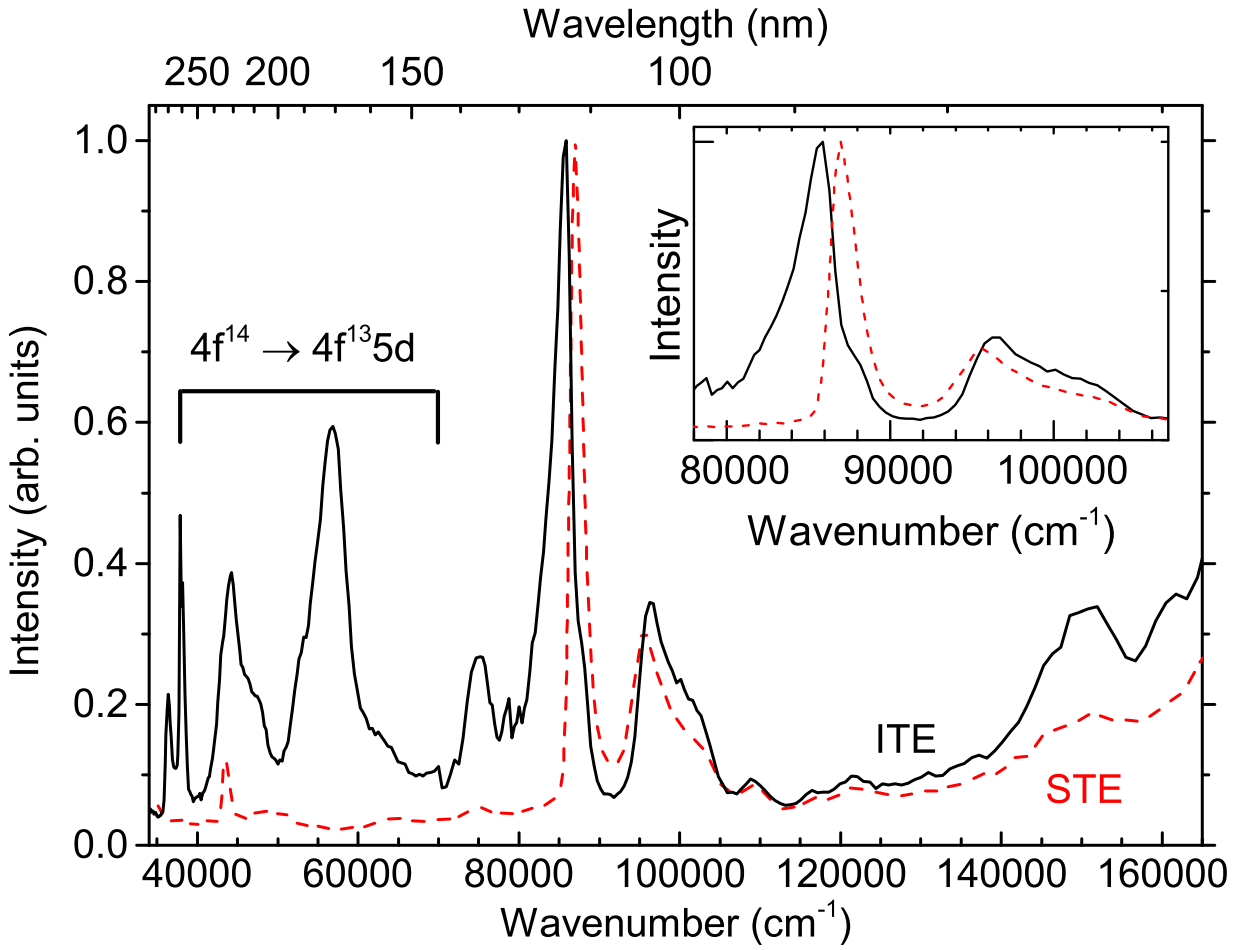

Figure 6.4 Excitation spectra of CaF_2:0.05%Yb^{2+} obtained at a sample temperature of 8 K monitoring the peak ITE emission energy at 18 200 cm^{-1} and the peak STE emission at 34 500 cm^{-1}. The peak at 43 000 cm^{-1} is a second-order artifact of the main peak. The inset shows an expanded region around the energy of the free exciton transition.

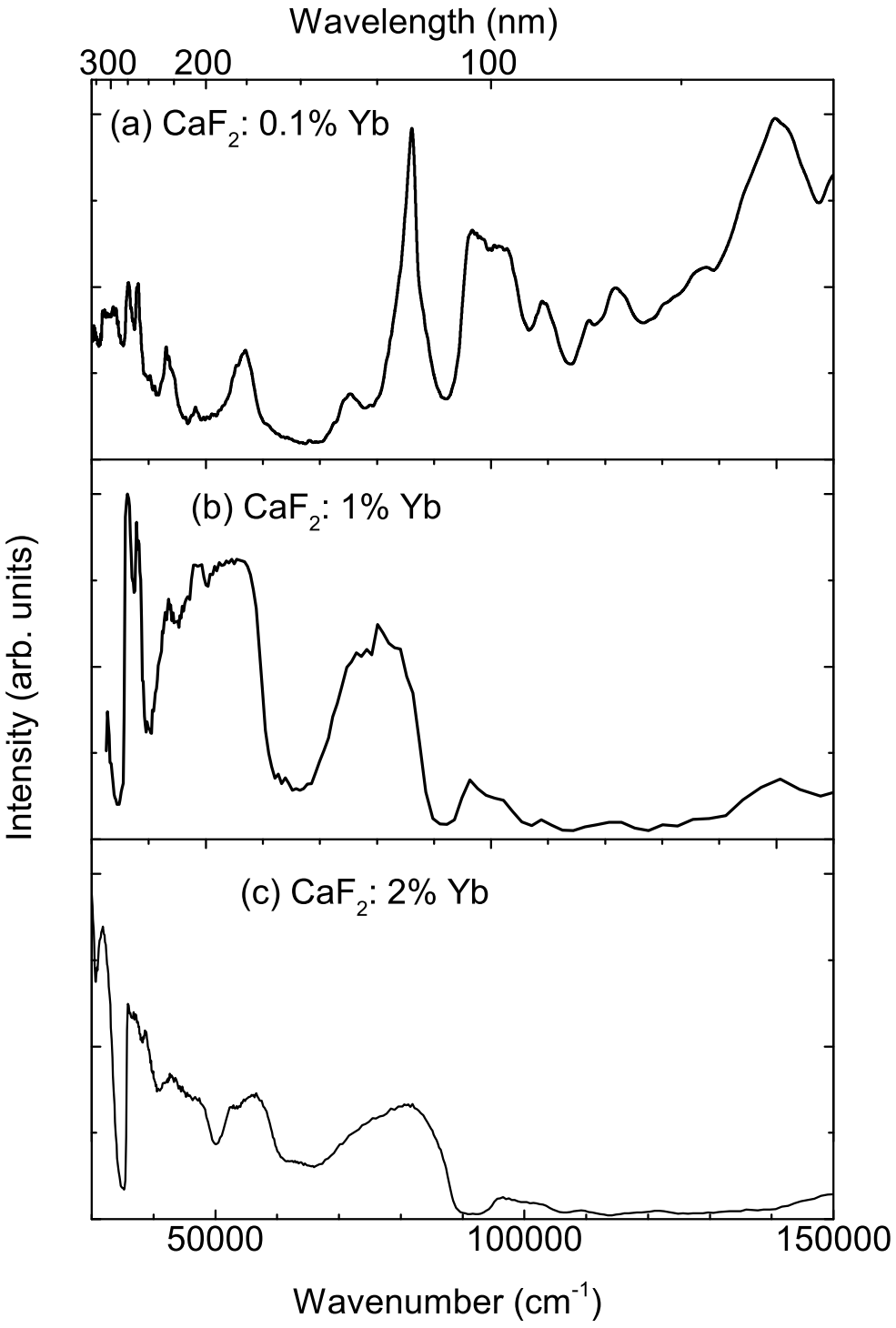

Figure 6.5 Excitation spectra of CaF_2:Yb at a sample temperature of 8 K monitoring emission at the ITE peak emission energy of 18 200 cm^{-1} for various concentrations of Yb doping: (a) 0.1% Yb (b) 1% Yb and (c) 2% Yb.

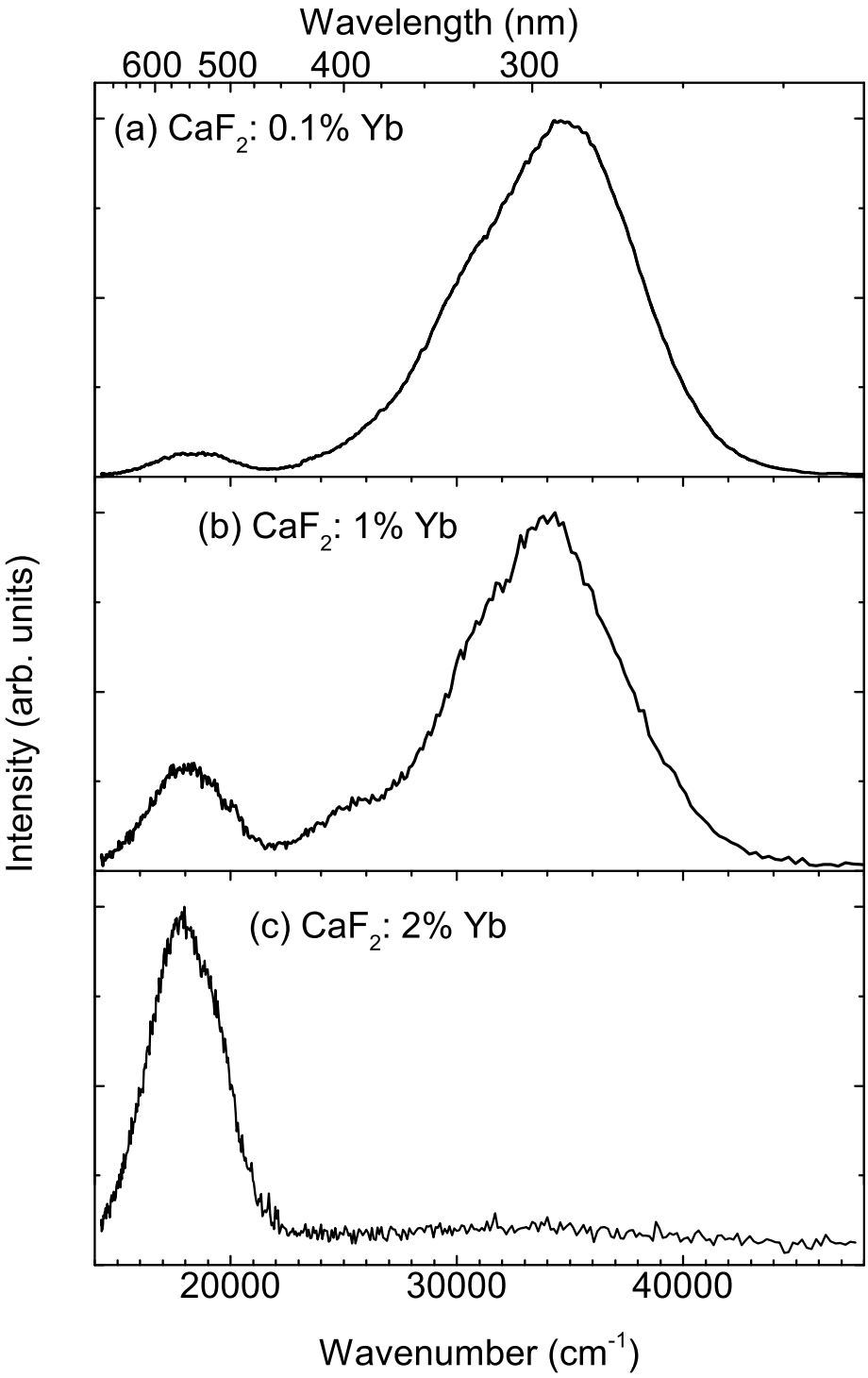

Figure 6.6 Emission spectra of CaF_2:Yb at a sample temperature of 8 K excited into the intrinsic exciton peak at 87 700 cm^{-1} for various concentrations of Yb doping: (a) 0.01%Yb (b) 1%Yb and (c) 2% Yb.

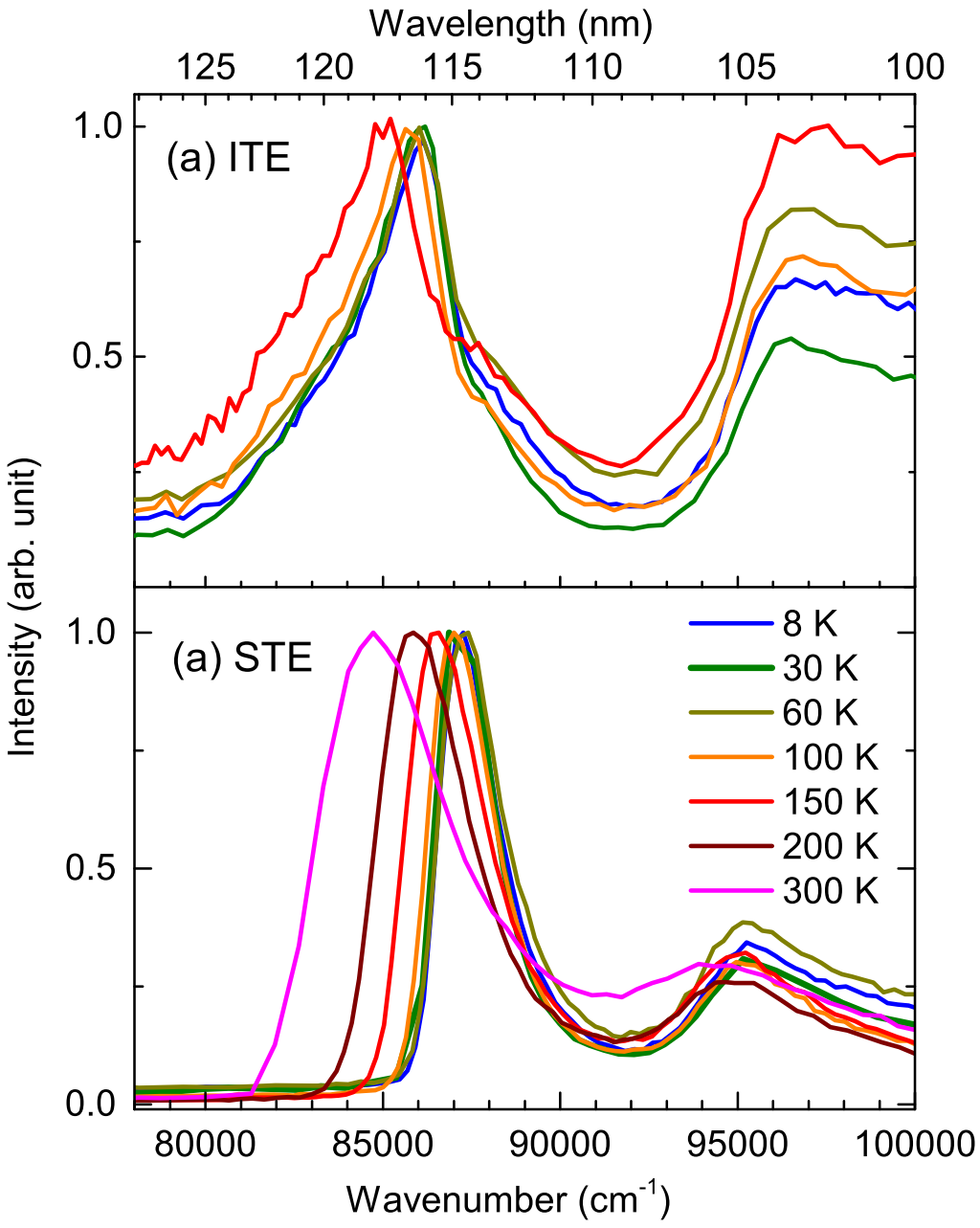

Figure 6.7 The energy shift of the free exciton excitation peak in CaF_2:Yb as a function of temperature monitored at (a) the STE peak emission energy, 34 500 cm^{-1} and (b) the ITE peak emission energy, 18 200 cm^{-1}

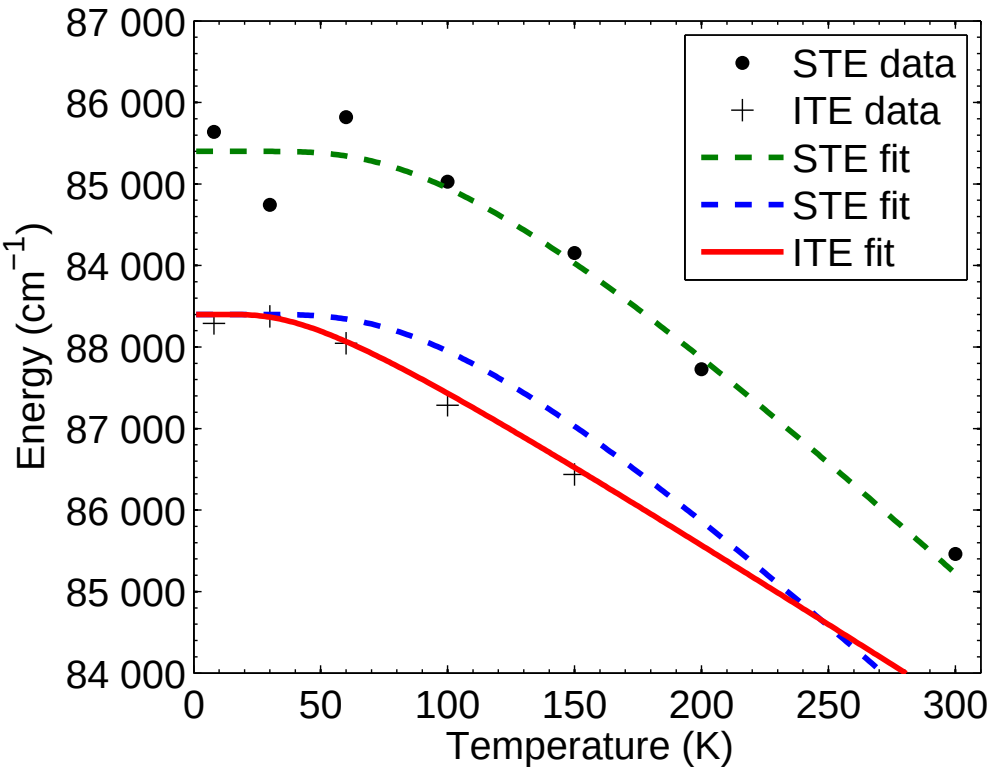

Figure 6.8 The energy shift of the free exciton excitation peak in CaF_2 as a function of temperature. The dots are monitored at the STE peak emission energy, 34 500 cm^{-1} and the crosses are monitored at the ITE peak emission energy, 18 200 cm^{-1}. The dotted lines are a line of best fit to the STE data with two values of $E_p(0)$. The blue line has a value of $E_p(0) = 86\,200$ cm^{-1}. The green line has a value of $E_p(0) = 87\,200$ cm^{-1}. The solid line is the best fit to the ITE data.

6.2 $NaMgF_3$:Yb

$NaMgF_3$ has been investigated as a host material for dosimetry as its effective atomic number is similar to human tissue. Due to its luminescence properties when doped with certain rare-earth ions $NaMgF_3$ can be used as a material for optically stimulated luminescence (OSL) dosimetry, a verstile alternative to thermoluminescence (TL) dosimetry. OSL measurements have been performed on $NaMgF_3$ doped with divalent europium [111] and trivalent cerium [112]. Finding new materials for applications such as OSL dosimetry is aided by greater understanding of the nature of the phenomena which lead to luminescence in the materials.

Here we present results of time-resolved spectroscopic experiments on $NaMgF_3$:Yb single crystals performed upon excitation with UV-VUV synchrotron radiation, both below and above the $NaMgF_3$ band edge. We observe excitation into the Yb^{2+} $4f^{13}5d$ states with subsequent ITE emission. For high energy excitation around the band edge, STE emission is observed. Evidence of energy transfer from the intrinsic excitons to the ITE is presented.

6.2.1 Emission and Excitation Measurements of $NaMgF_3$:Yb

The convolution of the two Yb^{2+} ITE centres appear as an emission band from 20 000–25 000 cm^{-1}, as discussed in Chapter 5. When the material is excited at energies lower than the conduction band the emission is only from the Yb^{2+} ITE [8]. When the material is excited at energies near to the conduction band, the material will emit from both the Yb ITE and the STE [88]. The STE in $NaMgF_3$ emits in a band from 25 000 to 35 000 cm^{-1} so the total emission from the ITE and STE combined is a wide band from 20 000 to 35 000 cm^{-1}, as shown in Figure **??**.

Figure 6.10 shows the 8 K excitation spectra monitoring the emission at the peak energies of the ITE and STE emission peaks in Figure 6.11. As indicated in the figure, emission from the ITE is observed upon excitation into the $4f^{13}5d$ states of the Yb^{2+} ion as well as the host excitonic states. Meanwhile, the STE emission can only be excited via formation of free excitons or upon higher energy excitation that corresponds to generation of separate electron-hole pairs. The peak at 90 000 cm^{-1} is the free exciton peak. This peak is reported in reflectance measurements to be 94 400 cm^{-1} [113]. The excitation spectrum shows the peak at a lower energy because the exciton emission is quenched by surface effects.

Figure 6.9 Emission from $NaMgF_3$:Yb. At higher excitation energies the emission is a convolution of Yb ITE emission from 20 000–25 000 cm^{-1} and self-trapped exciton emission at 25 000–35 000 cm^{-1}. The STE emission is quenched at excitation energies much lower than the conduction band of $NaMgF_3$.

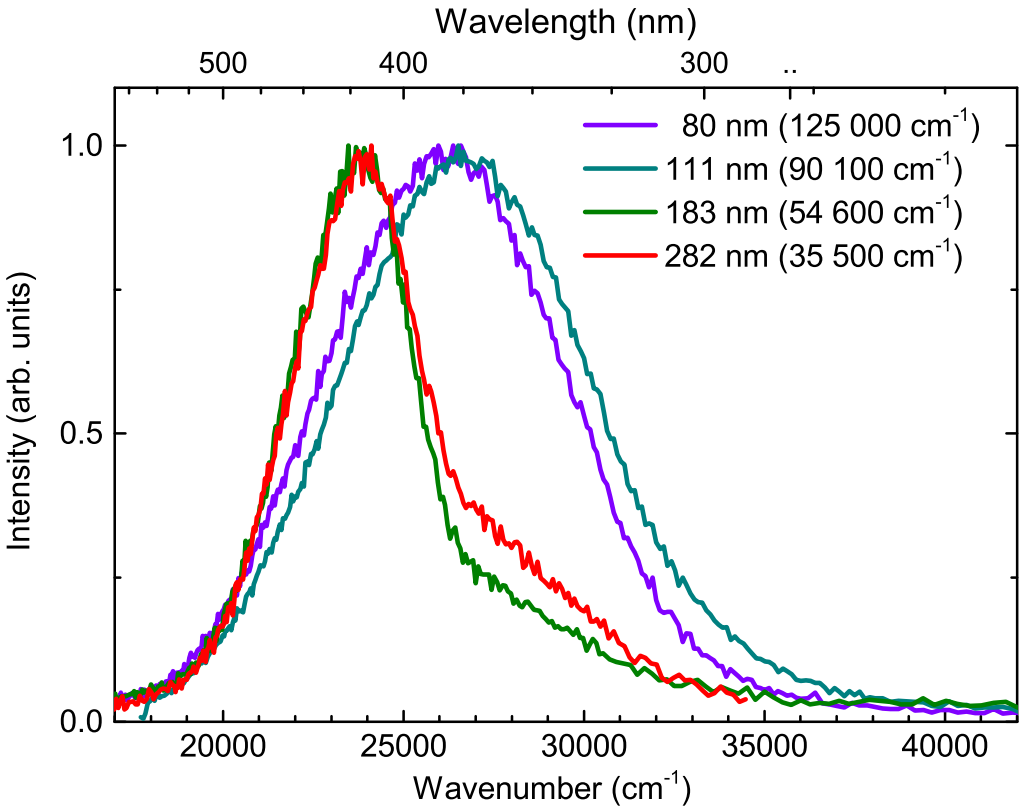

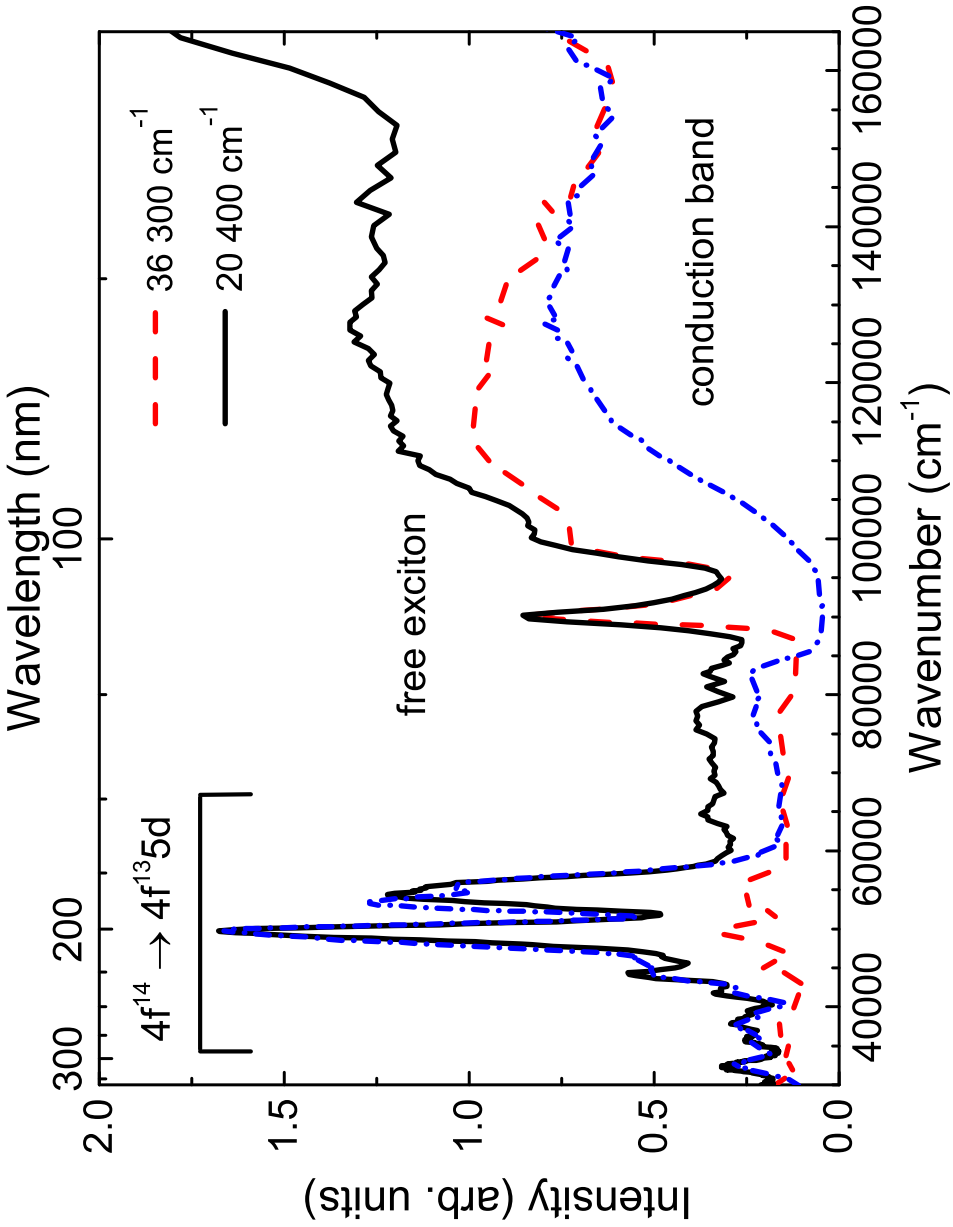

Figure 6.10 Excitation spectra of $NaMgF_3$:0.6%Yb at a sample temperature of 8 K. At 20 400 cm^{-1} the emission is mostly from ITEs, and at 26 300 cm^{-1} the emission is mostly from STEs.

Energy transfer between intrinsic excitons and Yb^{2+} ions is evident from the presence of the excitonic peak observed at 90 000 cm^{-1} when ITE emission is monitored. The most likely path from the formation of free excitons to ITE emission is formation of STEs and energy transfer from the STEs to Yb ions. Energy transfer from STEs to luminescent centres has been shown in other materials [114, 115].

Figure 6.11 shows how the same shift from ITE to STE emission can be achieved with changing excitation energy and temperature. At 50 000 cm^{-1} the emission is all from the Yb ITE. The emission remains constant with temperature because the $4f^{n-1}5d^1 \rightarrow 4f^n$ absorption at 50 000 cm^{-1} remains constant with temperature. At excitation into the free exciton and conduction band, the emission shifts to lower energy at high temperature because the STE emission is quenched whereas the ITE emission is not. The STE emission is quenched by thermally induced non-radiative transistions from the radiative STE state to the ground state [10].

To deconvolve the two emission bands from each other we can model the 8 K spectrum in Figure 6.12 with two Gaussian functions. Since the 300 K data is predominantly ITE emission we can first fit the 300 K data to a Gaussian function. Then we scale this Gaussian function and add it to another Gaussian function at a higher energy, representing the STE emission. The result of this fitting is shown in Figure 6.12 and the parameters of the functions are given in Table 6.1.

We can estimate the total intensity of the emission from the ITE compared to the STE by taking the ratio of the areas under the two Gaussian functions given in Table 6.1. When the excitation is into the free exciton peak, there is approximately 4 times as much emission from STE states as ITE states. When the excitation is into the conduction band, there is about 2 times as much. This relative increase in the ITE emission indicates that there is a pathway for free exciton creation to ITE emission which does not involve an STE being created.

6.2.2 Intraconfigurational Transistions of $NaMgF_3$:Yb

Vacuum ultraviolet spectroscopy extends excitation spectra to higher energies, which makes more $4f^n$–$4f^{n-1}5d$ transitions identifiable. Since the entire $4f^{n-1}5d$ energy range can be covered, all excitation energies which give radiative emission are measured. This broad energy range is excellent for constructing an accurate semi-empirical model of the crystal field effects on the Yb^{2+} ions in the material, as described in Chapter 2.

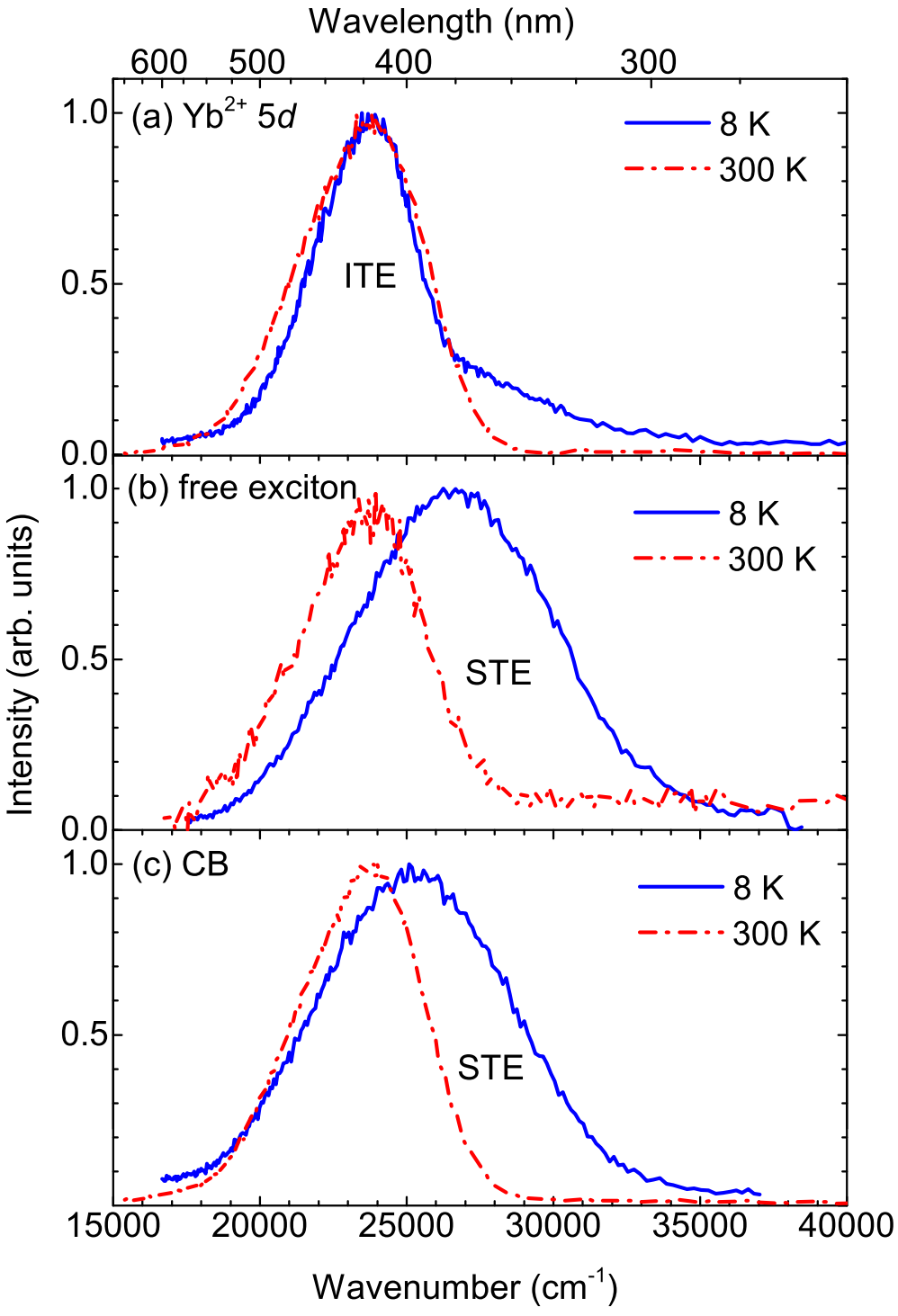

Figure 6.11 Emission from $NaMgF_3$:0.6%Yb at a sample temperature of 8 K and 300 K. (a) Below bandgap excitation into a Yb^{2+} $5d$ level at 54 600 cm^{-1} for 8 K and 49 800 cm^{-1} for 300 K, (b) Excitation into the free exciton peak at 90 100 cm^{-1} for 8 K and 87 000 cm^{-1} for 300 K, (c) Above bandgap excitation at 118 000 cm^{-1} for both temperatures. Dotted red lines are integrated over the fast time window (2–9 ns) and blue lines are integrated over the slow time window (46–70 ns).

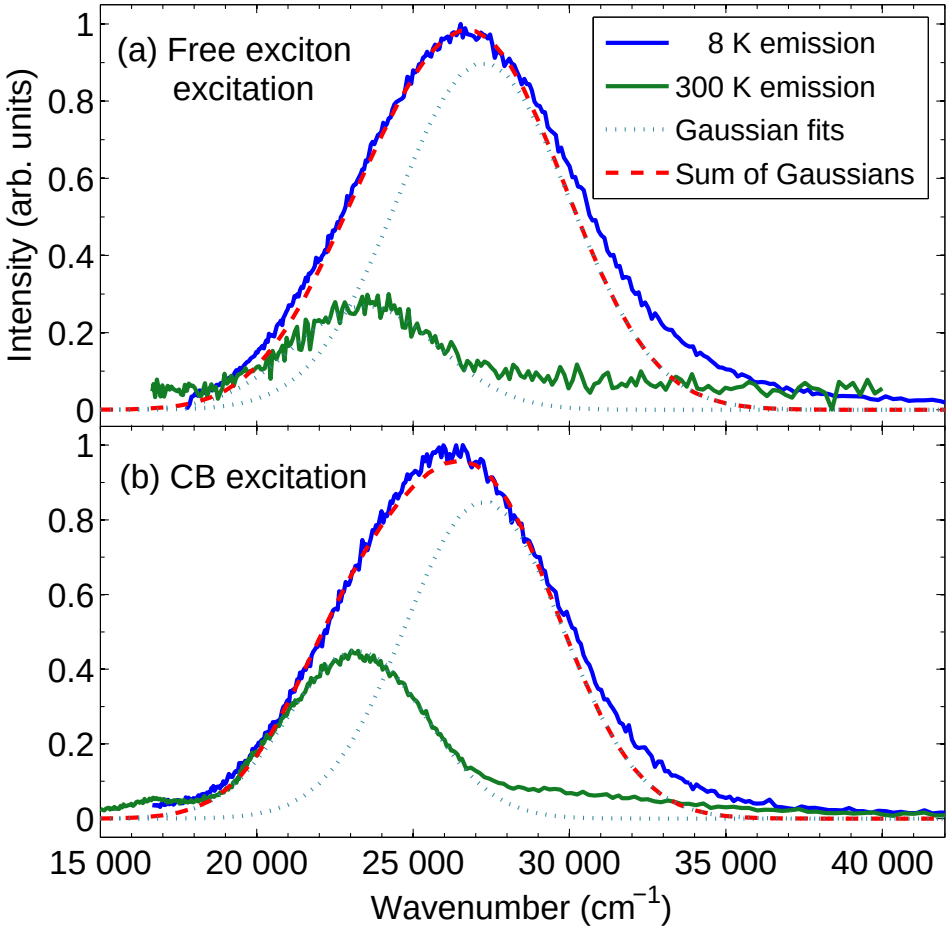

Figure 6.12 Emission from $NaMgF_3$:0.6%Yb (a) after excitation into the free exciton peak at 90 100 cm^{-1} for 8 K (solid blue line) and 87 000 cm^{-1} for 300 K (solid green line). (b) after excitation into the conduction band at 118 000 cm^{-1} for 8 K (solid blue line) and 300 K (solid green line). The blue dotted lines are Gaussian functions modeling the ITE emission and the STE emission. The red dashed line shows the sum of both Gaussian functions.

Table 6.1 The approximate positions and full widths at half maximum of the Gaussian functions simulating the peaks of the ITE and STE emission bands shown in Figure 6.12.

(a) Excitation into free exciton		
	ITE Emission	STE Emission
Centre (cm^{-1})	23 500	27 250
Width (cm^{-1})	2300	2750
Height (arb. units)	0.27	0.90
Area	15 570	62 040
Normalised Area	0.20	0.80
(b) Excitation into conduction band		
	ITE Emission	STE Emission
Centre (cm^{-1})	23 200	27 250
Width (cm^{-1})	2200	2500
Height (arb. units)	0.45	0.85
Area	24 810	53 270
Normalised Area	0.32	0.68

Which crystal field parameters are included in the parameterised model in what ratio depends on the geometry of the crystal field. In order to select relevant crystal field parameters, we must assume a structure for the Yb^{2+} site.

The structure of $NaMgF_3$ is much more complex than CaF_2 or SrF_2 and the site symmetry of Yb sites in $NaMgF_3$ is unknown. The Yb ions could replace either Mg^{2+} or a Na^+ ions. If Yb^{2+} replaces Na^+ there will have to be some mechanism of charge compensation in the form of a positive ion vacancy or subsitution to balance the overall charge.

The position of F^- ions in relation to Yb^{2+} were estimated with density functional theory (DFT) calculations by Jun Wen at the University of Science and Technology of China. Several geometries were tested, with the Yb^{2+} either replacing a Mg^{2+} ion or a Na^+ ion. The site geometry that was calculated to have the lowest total system energy was when the Yb^{2+} replaced a Na^+ and the charge compensation was achieved with a Na^+ vacancy, if the Na^+ site which was vacant was the nearest to the Yb^{2+} ion. The bond lengths and ligand positions for this most likely case are given in Table 6.2. The ligand positions are shown in Figure 6.13. The ligands do not have an obvious simple symmetry.

The Yb site symmetry was approximated to be tetragonal with latitudinal elongation, i.e. 3 pairs of ligands along the x, y and z axes, centred at (0,0,0) with the distance between

Table 6.2 Calculated coordinates of nearby F^- ions for Yb^{2+} in $NaMgF_3$ when the Yb^{2+} ion replaces a Na^+ ion, and there is a Na^+ ion vacancy at the nearest neighbour.

	bond length (Å)	bond angle θ (°)	bond angle ϕ (°)
F_1	2.277	90.0	193.8
F_2	2.282	49.1	302.8
F_3	2.282	130.9	302.8
F_4	2.318	90.0	107.2
F_5	2.355	51.3	40.9
F_6	2.355	128.7	40.9

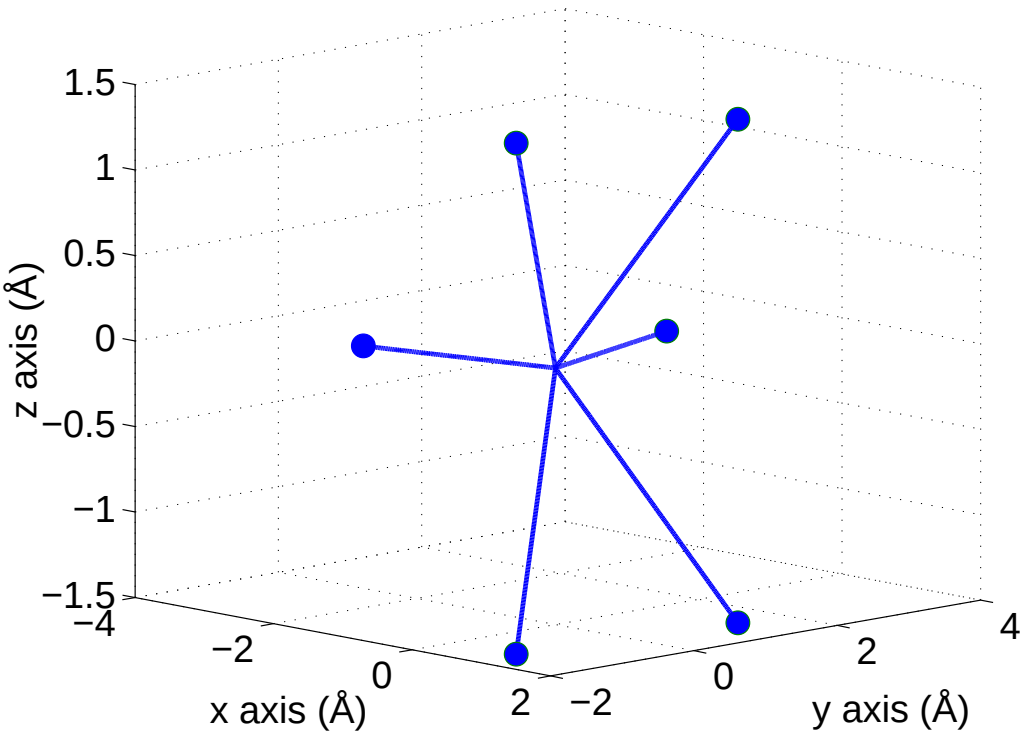

Figure 6.13 The nearby F^- ions around Yb^{2+} in $NaMgF_3$ when the Yb^{2+} ion replaces a Na^+ ion, and there is a Na^+ ion vacancy at the nearest neighbour, from Table 6.2.

the ligands equal for the pairs along the x and y axes, and a greater distance between the pair along the z axis, as shown in Figure 6.14. The tetragonal symmetry is represented by crystal field parameters B^4 and B^6 with a ratio with $B_4^4 = \sqrt{\frac{15}{4}} B_0^4$ and $B_4^6 = \sqrt{\frac{15}{4}} B_0^6$. The latitudinal elongation is represented by the parameter B_0^2.

Figure 6.14 Tetragonal site with lateral elongation used to approximate the crystal field acting on Yb^{2+} for $NaMgF_3$:Yb^{2+}.

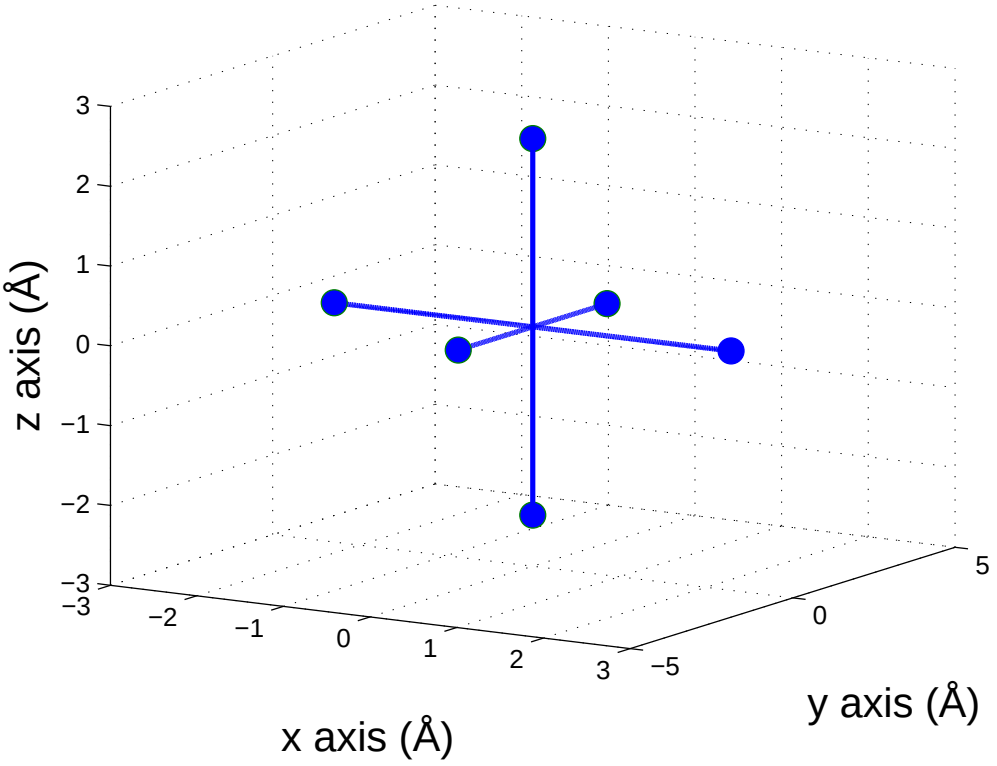

Figure 6.15 shows the $4f^n$–$4f^{n-1}5d$ transitions in $NaMgF_3$:Yb^{2+} along with a simulated spectrum calculated with the semi-empirical crystal field model. The crystal field parameters were qualitatively fitted to the VUV excitation spectrum.

Table 6.3 contains the values of the crystal field parameters calculated from their definitions for the free Yb^{2+} ion; those fitted to $SrCl_2$:Yb^{2+} and CaF_2:Yb^{2+} using a $4f^{14}$+$4f^{13}5d$ effective Hamiltonian; and the values of parameters fitted here. The Coulomb parameters have little effect on the spectrum, and are kept at the same value for all three crystal environments. The value of the B^4 and B^6 parameters for $NaMgF_3$:Yb are smaller than in CaF_2:Yb. A discussion of the physical meaning of the parameters is given in Chapter 2.

Figure 6.15 (a) Simulated spectrum of $NaMgF_3:Yb^{2+}$ calculated with a semi-empirical crystal field model. The red lines are the zero-phonon lines (ZPLs) of the transitions and the blue line is a Gaussian convolution of the ZPLs. (b) Excitation spectrum of $NaMgF_3$:Yb at 8 K with $\lambda_{em} = 25\,000$ cm^{-1}

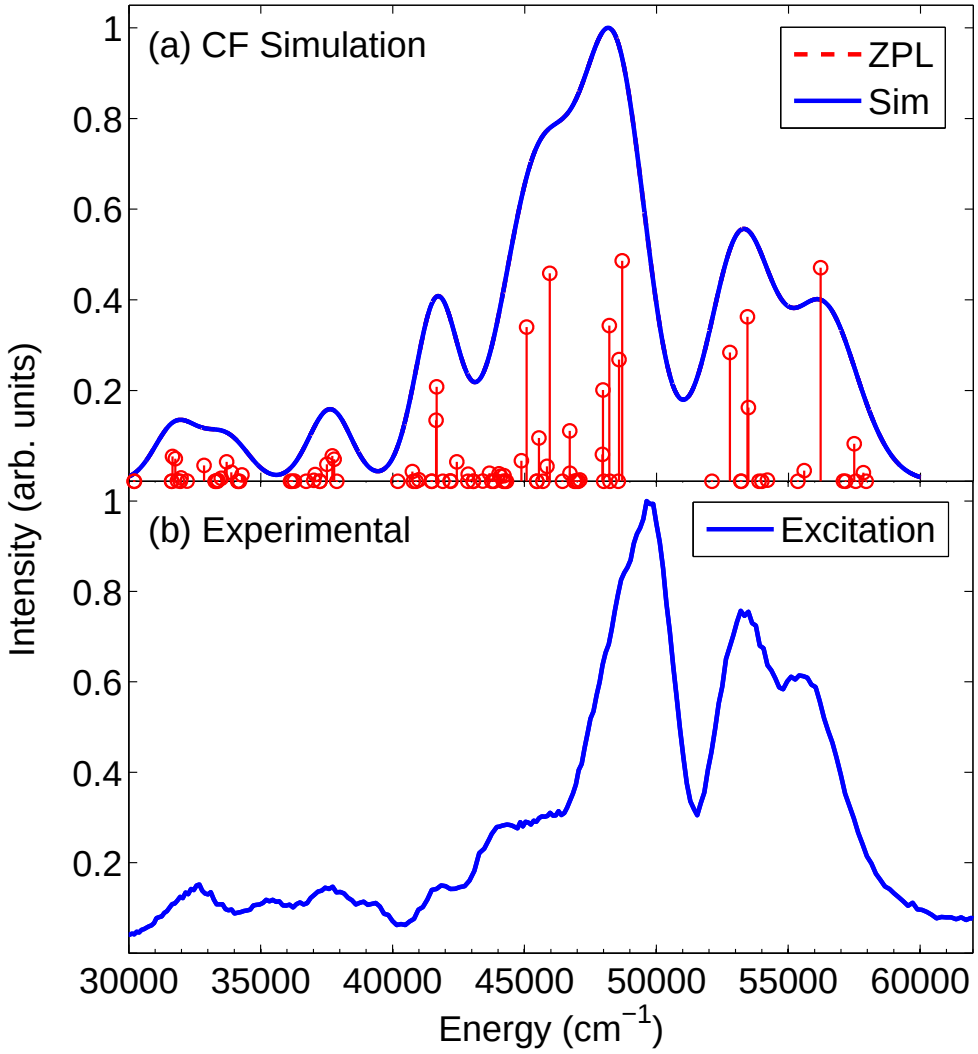

Table 6.3 Final values of parameters for the crystal field fit of Yb^{2+} in $NaMgF_3$ and MgF_2.

Parameter	Free Yb^{2+} ion [a]	$SrCl_2$:Yb^{2+} [b]	CaF_2:Yb^{2+} [c]	$NaMgF_3$:Yb^{2+}	MgF_2:Yb^{2+}
$\Delta E_{(fd)}$		38 382	42 700	42 800	42 000
$\zeta_{(ff)}$	1290	1211	1204	2000	3000
$\zeta_{(dd)}$	2899	2950	2950	2700	1000
$F^2_{(fd)}$	23 210	14 355	14 355	14 355 [d]	14 355 [d]
$F^4_{(fd)}$	10 646	7222	7222	7222 [d]	7222 [d]
$G^1_{(fd)}$	10 059	4693	4693	4693 [d]	4693 [d]
$G^3_{(fd)}$	8046	5382	5382	5382 [d]	5382 [d]
$G^5_{(fd)}$	6085	4349	4349	4349 [d]	4349 [d]
$B^2_{(ff)}$				-700	-1000
$B^4_{(ff)}$ [e]		-725	-2036	500	1000
$B^6_{(ff)}$ [f]		292	821	-200	-200
$B^2_{(dd)}$ [e]				-6000	8000
$B^4_{(dd)}$ [e]		$-20\,442$	$-37\,726$	22 000	40 000

[a] Ref. [116] [b] Ref. [117] [c] Ref. [75] [d] Not fitted here. Held at the values determined by Ref. [117]. [e] $B^4_0 = B^4$, $B^4_{\pm 4} = \sqrt{\frac{5}{14}} B^4$. [f] $B^6_0 = B^6$, $B^6_{\pm 4} = -\sqrt{\frac{7}{2}} B^6$.

6.3 MgF_2:Yb

Figure 6.16 shows the 8 K emission spectra of MgF_2:Yb at various excitation energies corresponding to features shown in the excitation spectrum, Figure 6.17. When the Yb^{2+} ions are excited into a $5d$ state below the bandgap, the emission is at 19 000–23 000 cm^{-1}, previously identified as emission from $4f^{13}5d \rightarrow f^{14}$ transitions of the Yb^{2+} ion [8]. When the crystal is excited into a higher peak in the excitation spectrum (see below), the emission shifts to higher energy. The shift occurs because the emission shifts predominantly from radiative recombination of MgF_2 STEs from their triplet state [60]. The emission is similar when the crystal is excited into the conduction band.

Figure 6.17 shows the 8 K excitation spectra monitoring at the intraconfigurational Yb emission and STE emission peaks in Figure 6.1. The peak at 90 000 cm^{-1} is the free exciton peak [60]. There is a peak at 69 400 cm^{-1} with a fast component when monitoring the STE emission. This peak has been identified in absorption as a defect band caused by intestitial fluoride ions, sometimes called an "I centre" [118, 119].

Figure 6.18 shows the emission spectra of MgF_2:Yb after excitation into the conduction band. As temperature is increased, two peaks appear in the fast time gate at 22 000 and 30 000 cm^{-1} respectively. The origin of these two peaks is unknown.

The $4f^{n-1}5d^1 \rightarrow 4f^n$ transitions of MgF_2:Yb^{2+} can be modeled with a semi-empirical model of the crystal field. As for $NaMgF_3$:Yb^{2+}, site symmetry was assumed to be tetragonal with latitudinal distortion. A VUV absorption spectrum has been measured by Kück et al. [120]. The absorption spectrum has substantially different relative intensities between peaks when compared to the excitation spectrum, indicating that absorption into some Yb^{2+} $5d$ levels does not result in efficient ITE radiative relaxation. Figure 6.19 shows the $4f^n$–$4f^{n-1}5d$ transitions in MgF_2:Yb^{2+} along with a simulated spectrum calculated with the semi-empirical crystal field model. Since the calculation models the absorption process, the crystal field parameters were qualitatively fitted to the absorption spectrum rather than the excitation spectrum. The values of the crystal field parameters are given in Table 6.3 above.

Again the values of the Coulomb parameters have little effect on the spectrum, and are kept the same as they were for previous Yb^{2+} calculations. The value of the B^4 and B^6 parameters for MgF_2:Yb are larger than in CaF_2:Yb and $NaMgF_3$:Yb. The $B_0^2(dd)$ parameter has a positive sign, which according to superposition theory means the tetragonal distortion is a contraction rather than an elongation.

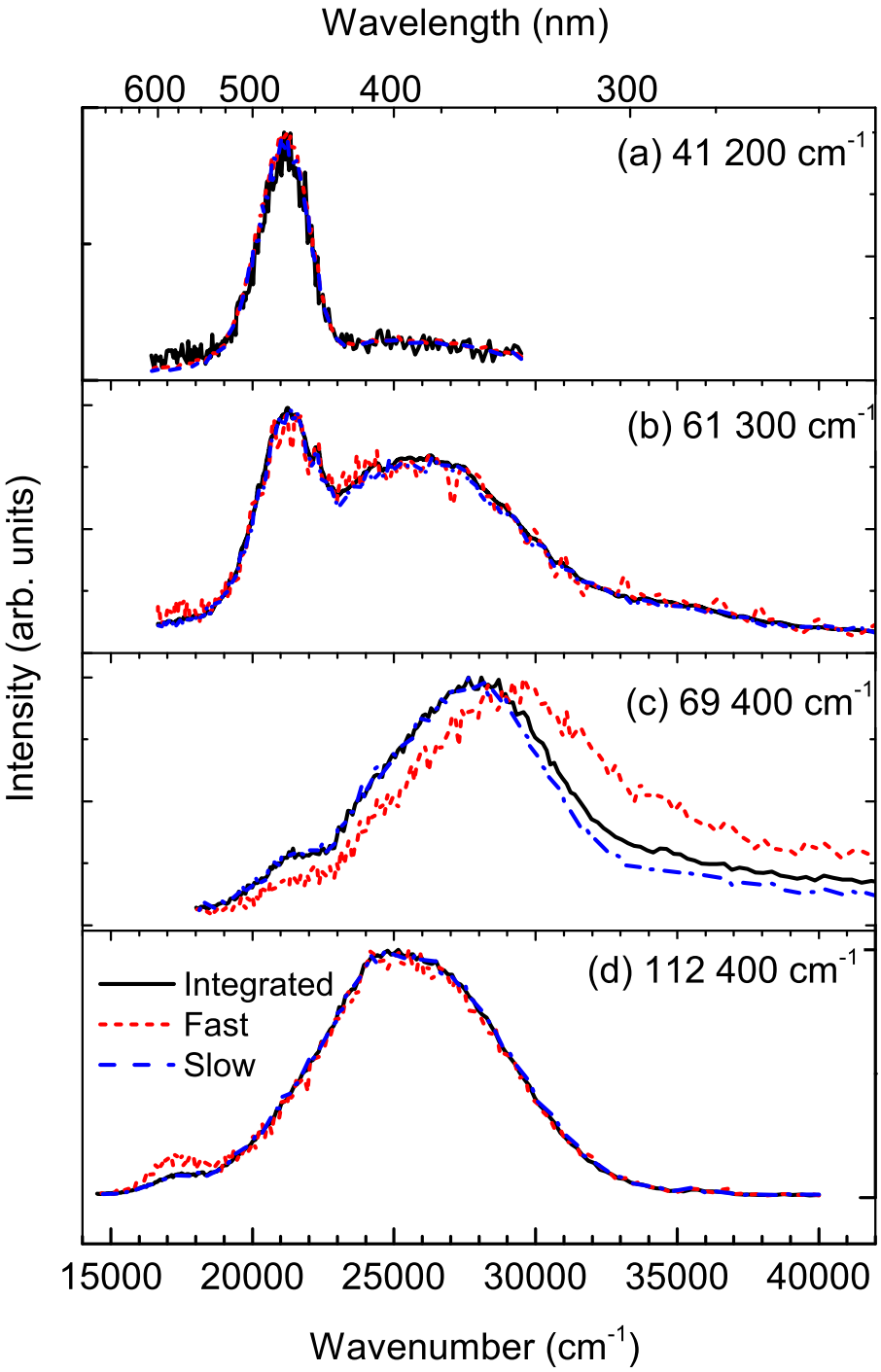

Figure 6.16 Emission from MgF_2:Yb at a sample temperature of 8 K. (a) Below bandgap excitation into a Yb^{2+} 5*d* level at 41 200 cm^{-1}. (b) Excitation at 61 300 cm^{-1}. (c) Excitation into the peak at 69 400 cm^{-1}. (d) Above bandgap excitation at 112 400 cm^{-1} for both temperatures. Dotted red lines are integrated over the fast time window (2–9 ns) and blue lines are integrated over the slow time window (46–70 ns).

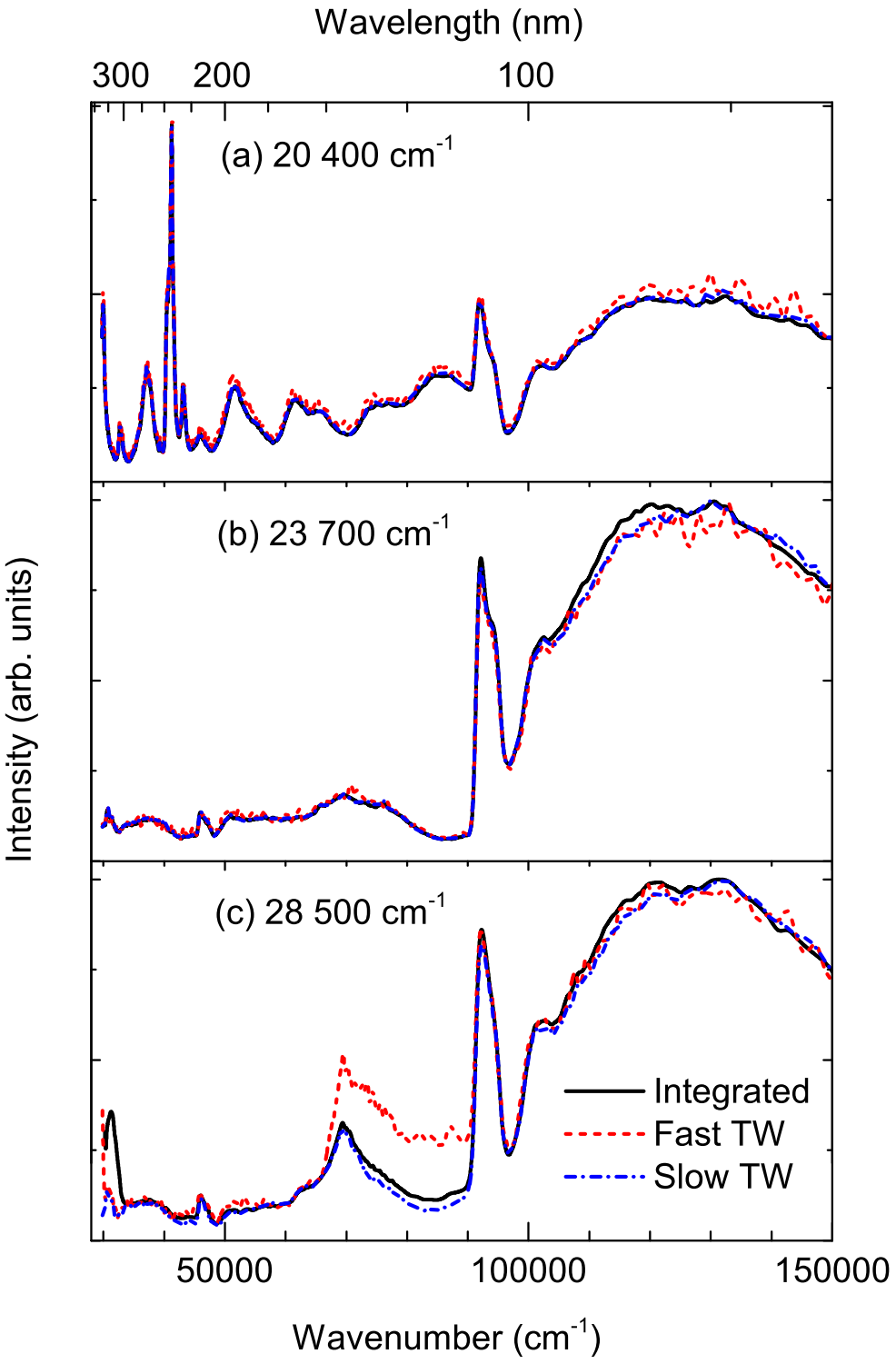

Figure 6.17 Excitation spectra of MgF_3:Yb at a sample temperature of 8 K monitoring three emission frequencies. At 20 400 cm^{-1} the emission is mostly from ITEs, and at 23 700 cm^{-1} and 28 500 cm^{-1} the emission is mostly from STEs. Dotted red lines are integrated over the fast time window (2–9 ns) and blue lines are integrated over the slow time window (46–70 ns).

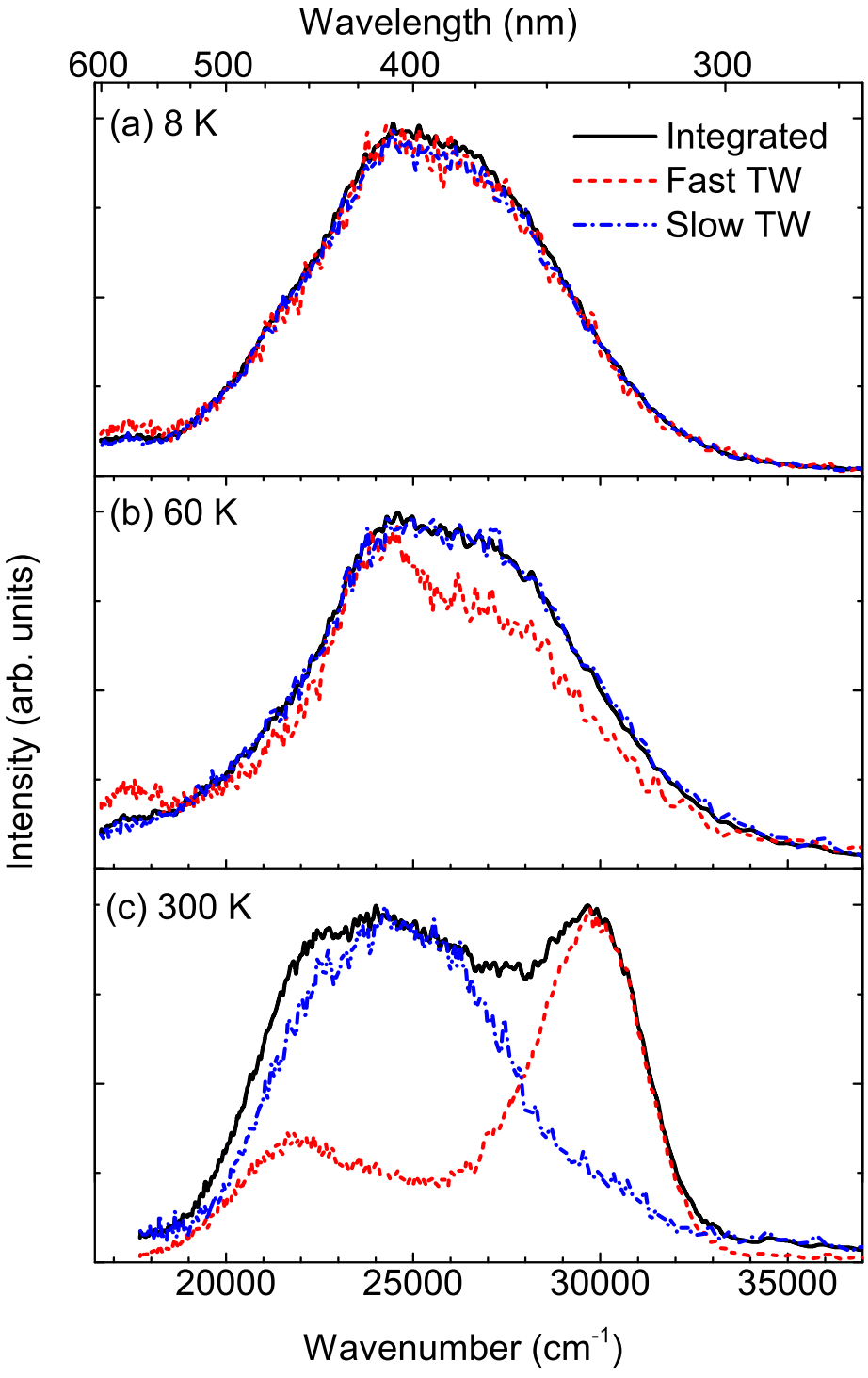

Figure 6.18 Emission from MgF_2:Yb after above-bandgap excitation at (a) 125 000 cm^{-1} and a sample temperature of 8 K (b) 125 000 cm^{-1} and a sample temperature of 60 K (c) 132 000 cm^{-1} and a sample temperature of 300 K . Dotted red lines are integrated over the fast time window (2–9 ns) and blue lines are integrated over the slow time window (46–70 ns).

Figure 6.19 (a) Simulated spectrum of MgF_2:Yb calculated with a semi-empirical crystal field model. The red lines are the zero-phonon lines (ZPLs) of the transitions and the blue line is a Gaussian convolution of the ZPLs. (b) Excitation spectrum of MgF_2:Yb at a sample temperature of 8 K with $\lambda_{em} = 20\,400$ cm^{-1} and the room temperature absorption spectrum reported by Kück et al. [120].

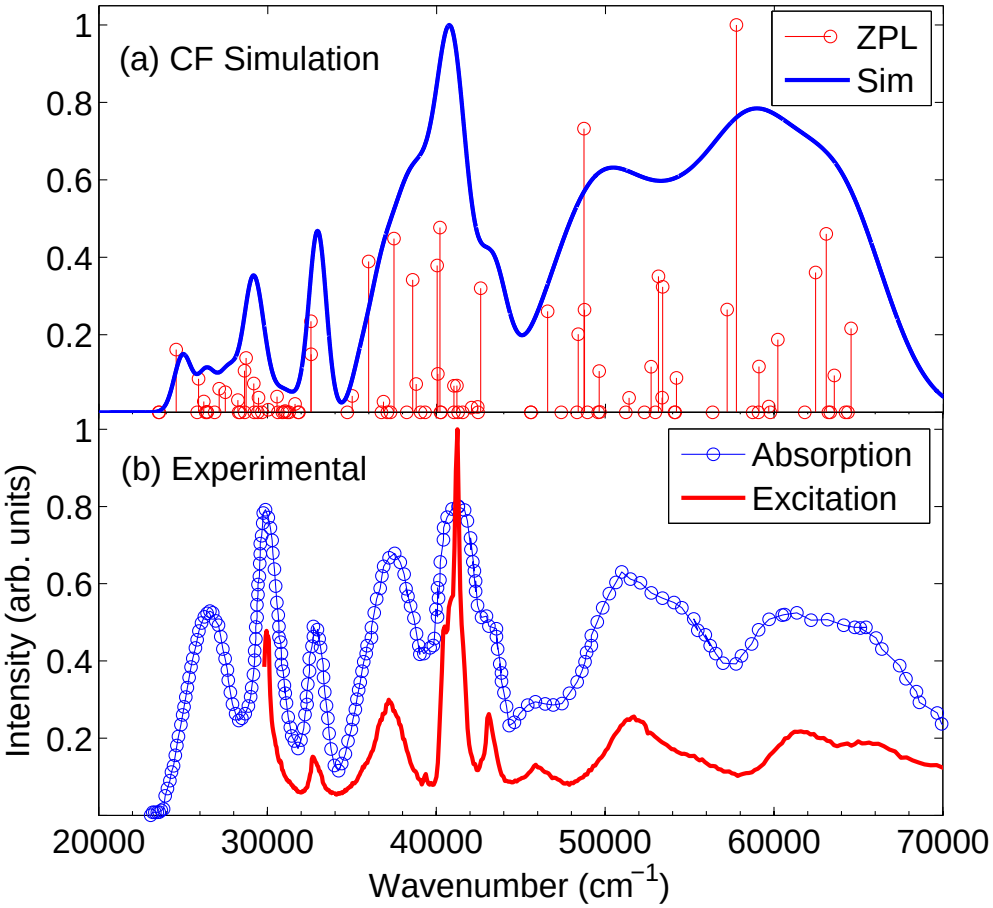

Table 6.4 Value of intrinsic parameters for CaF_2:Yb^{2+}, $NaMgF_3$:Yb^{2+} and MgF_2:Yb^{2+} at $R_0 = 2.366$ Å.

	$\bar{B}^4(R_0)$	$\bar{B}^2(R_0)$
CaF_2:Yb	11 608	
$NaMgF_3$:Yb	5714	23 222
MgF_2:Yb	6763	61 390

Since the Yb^{2+} ion site geometries are very different in CaF_2:Yb^{2+}, $NaMgF_3$:Yb^{2+} and MgF_2:Yb^{2+} it is difficult to make a direct comparison of these parameters. To minimise geometric effects we can compare the intrinsic crystal field parameters.

The ligand positions in Table 6.2 are used to calculate the intrinsic crystal field coordinates from the crystal field parameters for comparison in Table 6.4. These represent the interaction between the ligands and the Yb^{2+} ion when the ligands are rotatated and translated to be at the same distance along the z-axis. The CaF_2:Yb^{2+} intrinsic parameters were calculated assuming the Yb^{2+} ion replaces the Ca^{2+} ion, so the Yb^{2+} ion is surrounded 8 fluoride ligands, with each ligand at the edge of a cube with bond lengths of 2.366 Å [121]. For $NaMgF_3$:Yb^{2+}, the intrinsic parameters were calculated assuming the Yb^{2+} ion is at a tetragonal site with a longitudial elongation as shown in Figure 6.14. The ligand lengths along both the x and y axes are 2.29 Å and the length along the z axis is 2.36 Å. Similarly for MgF_2:Yb^{2+}, the intrinsic parameters were calculated assuming the Yb^{2+} ion is at a tetragonal site with a longitudial contraction. The ligand lengths along the x and y axes are 2.18 Å and the length along the z axis is 2.16 Å.

From the results for Yb^{2+} in $NaMgF_3$ and MgF_2, it appears that the ligands along the z-axis exert a much stronger field than the other ligands. However, the site geometries of $NaMgF_3$:Yb^{2+} and MgF_2:Yb^{2+} have been simplified in order to fit the crystal field parameters, so the parameters in Table 6.4 are a first approximation.

Table 6.5 Bandgap and free exciton energies for alkali fluorides measured by reflection. The binding energy is given as the difference in energy between the lowest exciton state and the band edge.

	Bandgap (cm^{-1})	Exciton energy (cm^{-1})	Binding energy (cm^{-1})
CaF_2:Yb [a]	97 600	90 200	7400
$NaMgF_3$:Yb [b]	104 100	94 400	9700
MgF_2:Yb	101 000 [c]	95 200 [d]	5800

[a] Ref. [105] [b] Ref. [113] [c] Ref. [123] [d] Ref. [124]

6.4 Comparisons Between Materials

Now we can compare the spectra of the materials presented above and discuss the differences between them. In Figure 6.20 the energy of the self-trapped exciton excitation peak increases from CaF_2 to $NaMgF_3$ to MgF_2. This is to do with the difference in bandgap between the materials but also the difference in binding energy of the free excitons. The values of the bandgaps and binding energies are given in Table 6.5 for reference. The bandgap of materials increases as the overlap between orbitals from neighbouring ions increases [105]. The size of the bandgap increases with decreasing lattice constants from CaF_2 to MgF_2 to $NaMgF_3$. However, the excitation peak associated with the self-trapped exciton is higher for MgF_2 than $NaMgF_3$. The binding energy of the exciton increases with the size of the ionic radii of cations in the lattice. The radius of Na^+ ions is 116 pm, Ca^{2+} is 114 pm, and Mg^{2+} is 86 pm [122] and the binding energy of the free exciton follows this trend.

The excitation peak associated with free exciton of CaF_2:Yb in Figure 6.20(a) shifts to higher energy when Yb ITE emission (rather than STE) is monitored, while for $NaMgF_3$:Yb and MgF_2:Yb the excitation peak is the same whether we are monitoring emission from Yb or STE states. This is because the overlap in emission for $NaMgF_3$:Yb and MgF_2 makes it hard to isolate emission originating from either STE or ITE states. Comparing the emission spectrum when each crystal is excited into the free exciton peak, Figure 6.21 shows that the ITE emission from CaF_2:Yb^{2+} does not overlap the CaF_2 STE emission, but the $NaMgF_3$:Yb and MgF_2:Yb emission have both bands merged.

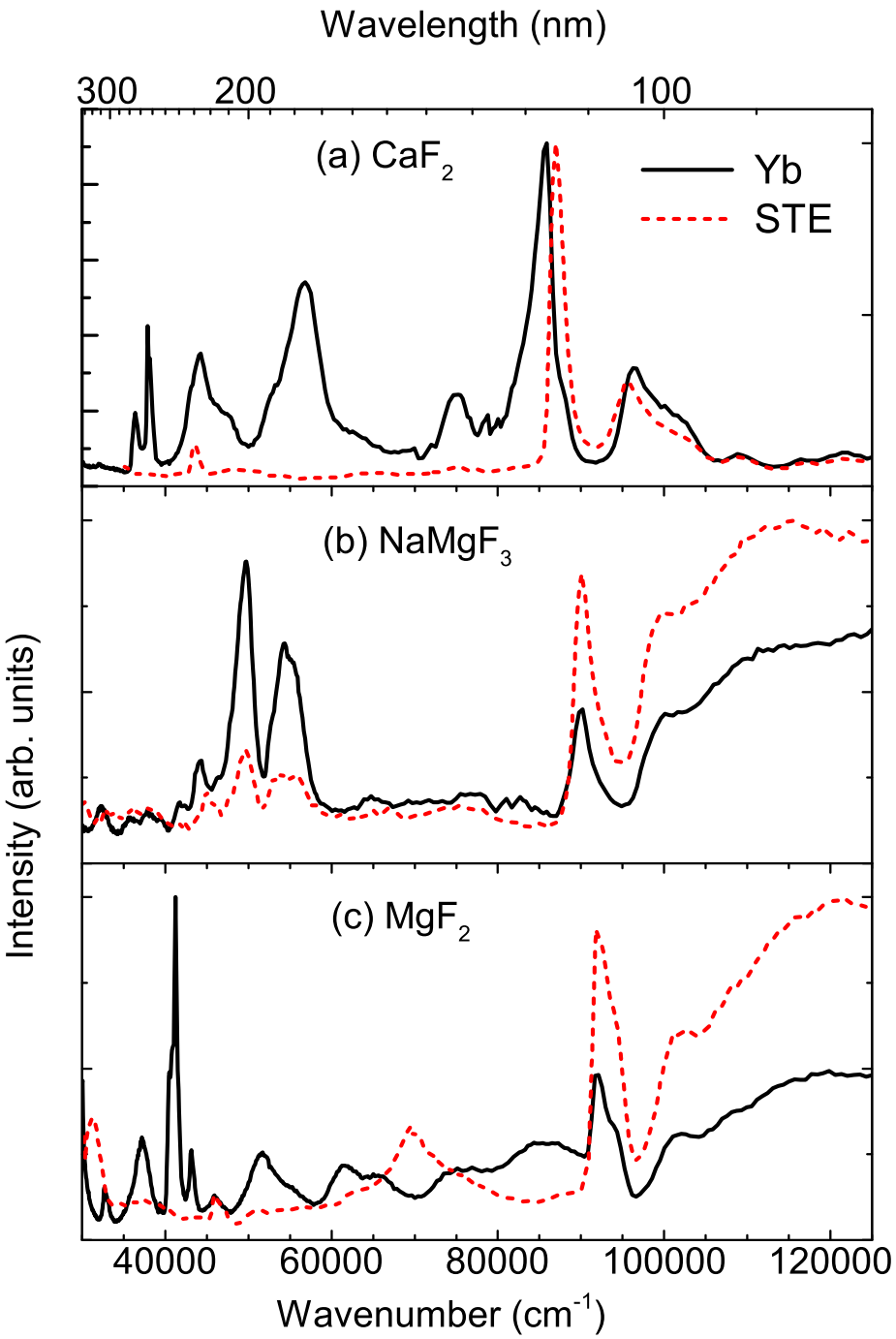

Figure 6.20 Comparison between excitation spectra of Yb in CaF_2, MgF_2, and $NaMgF_3$ at a sample temperature of 8 K, monitoring emission corresponding to both Yb transitions and to STE recombination luminescence.

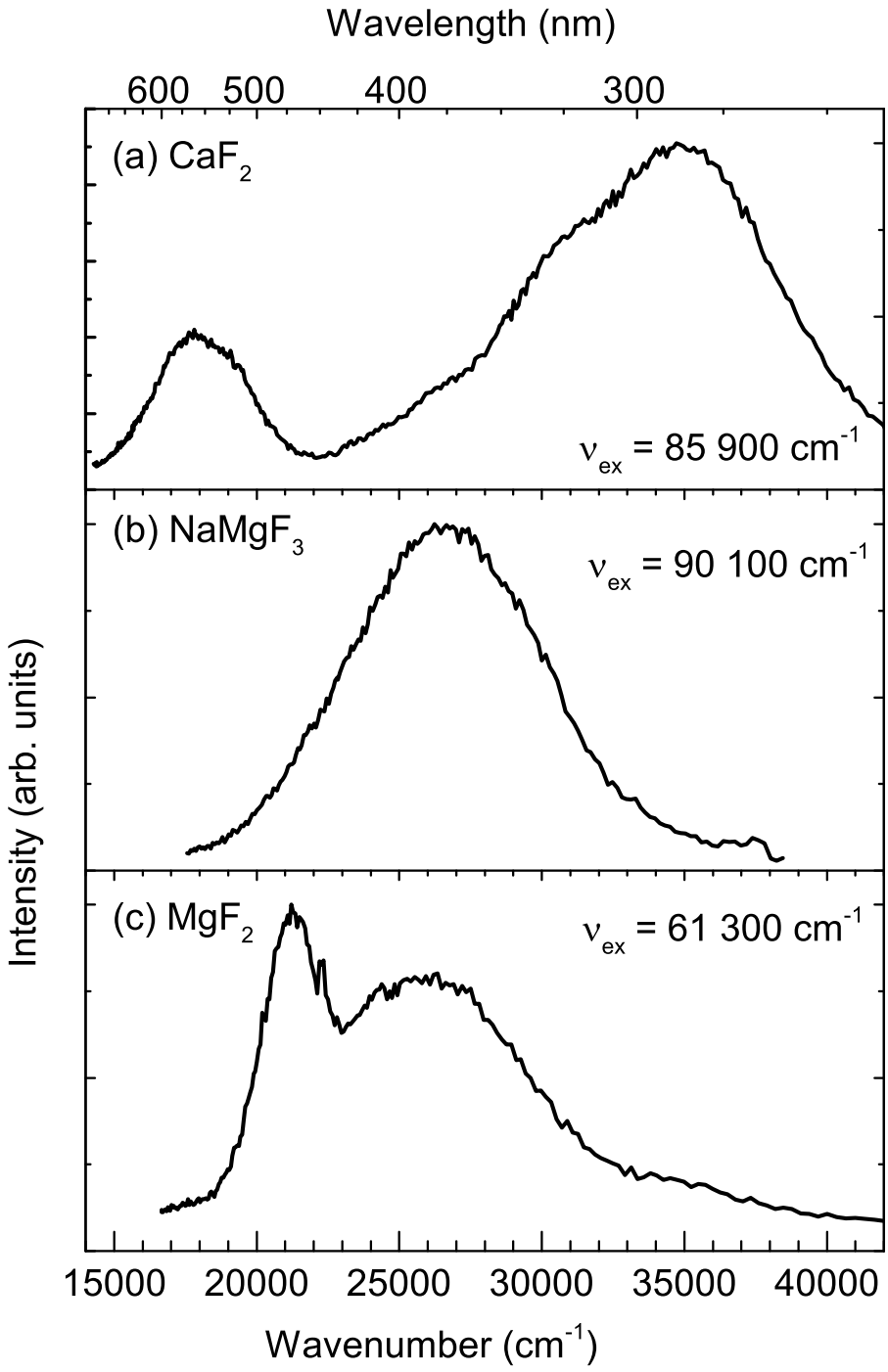

Figure 6.21 Emission of Yb-doped CaF_2, MgF_2, and $NaMgF_3$ at a sample temperature of 8 K, showing the energy overlap between Yb emission and STE recombination luminescence. The CaF_2:Yb is excited at 85 900 cm^{-1}, $NaMgF_3$:Yb is excited at 90 100 cm^{-1}, MgF_2:Yb is excited at 61 300 cm^{-1}.

6.5 Conclusion

The excitation of single crystals of CaF_2:Yb, $NaMgF_3$:Yb and MgF_2:Yb by UV-VUV synchrotron radiation excitation has been presented. Emission from ITE or $4f^{13}5d$ configurations has been identified in all three materials. Excitation into the fundamental absorption band of the crystals results in emission from intrinsic states and Yb^{2+} impurity centres. The interplay between intrinsic distortions and Yb^{2+} impurity centres is observed and analysed with changing excitation energy and temperature.

When the CaF_2:Yb crystal was excited at an energy to optimally create free excitons, emission bands due to both ITE and STE states are observed, suggesting that the free excitons become trapped as STEs, which then go on to relax radiatively or create ITEs via energy transfer to the Yb^{2+} impurity centres. The temperature dependence of the peak resonant absorption of the free exciton has been measured and is explained by considering the change in bandgap with temperature through Viña's equation.

$NaMgF_3$:Yb was also excited into its peak free exciton resonance with similar results to CaF_2:Yb. Again emission bands due to both ITE and STE states are observed, so in $NaMgF_3$:Yb^{2+} free excitons decay to STEs, which then go on to relax radiatively or excite Yb^{2+} ions to ITE states. Unlike CaF_2:Yb where the ITE and STE emission bands are seperated by a few thousand wavenumbers, in $NaMgF_3$:Yb the emission bands from ITE and STE states overlap each other. The emission bands were deconvolved by being modeled as Gaussian functions, and the comparitive emission intensity from each band was estimated. The ITE emission approximately doubles in comparison to STE emission as the excitation energy is increased from the intrinsic exciton resonance peak to the conduction band. Along with room temperature excitation measurements this is evidence that emitting ITE states are also created through energy transfer from conduction band states which does not involve STE states.

The lower-energy section of the excitation spectrum of $NaMgF_3$:Yb consists of the Yb^{2+} $4f^{n-1}5d^1 \rightarrow 4f^n$ transitions. This spectrum was qualitatively fitted to a semi-emperical crystal field model where the Yb^{2+} site geometry was assumed to be a latitudinally-distorted tetragonal symmetry. The crystal field parameters were compared to previous work on CaF_2 and $SrCl_2$. The B^4 parameter is almost half the value found for CaF_2 and has the opposite sign.

CaF_2:Yb, $NaMgF_3$:Yb and MgF_2:Yb excitation spectra were compared. The increased peak energy of the free exciton peak from CaF_2 to $NaMgF_3$ to MgF_2 is caused by the com-

bination of the influence of the changing bandgap between the materials, which increases with decreasing lattice constants from CaF_2 to MgF_2 to $NaMgF_3$, and the difference in binding energy of the free excitons, which increases with the size of the ionic radii of cations in the lattice from $NaMgF_3$ to CaF_2 to MgF_2.

The difference in free exciton peak position between CaF_2 monitored at the peak ITE emission and STE emission is 1500 cm^{-1}. This difference is not seen for $NaMgF_3$ or MgF_2, which is likely due to the overlap between the ITE and STE emission bands making it difficult to distinguish emission from either excitation for $NaMgF_3$ and MgF_2.

Chapter 7

CdF_2-CaF_2 Superlattices

Superlattices are structures with periodic nanometer layers of materials such as in Figure 7.1. In the last two decades, nanofabrication techniques have drastically improved and we are now able to create nearly ideal layered crystalline structures on the nanoscale [125–128] which have found applications in areas such as quantum electronics, high-speed and high-density three-dimensional integrated optoelectronic devices, intelligent sensors, and lasers.

Superlattices represent a sequence of quantum wells and barriers. The scale of the layers induces the appearance of new optical properties such as enhanced and shifted emission intensity, which as well as being useful for applications also allow new insights into the fundamental behaviour of electrons in a confined crystalline environment. Quantization effects are significant for superlattices with monolayers (MLs) of a few nanometers where the critical dimensions are comparable to typical electron wavelengths or migration ranges of mobile electronic excitations such as excitons.

Although significant efforts have been made so far to understand these processes in heterostructures and superlattices based on semiconductors (see [129] for example), nanolayered structures based on wide bandgap materials are lacking systematic investigation.

In this chapter results on VUV spectroscopy of 5 ML and 3 ML CdF_2–CaF_2 superlattices to show the change in behaviour of the STE in CdF_2 when it is confined and give an indication of the radius of the exciton.

7.1 Background Work

CdF_2 and CaF_2 have the same cubic crystal structure and similar lattice constants so they are able to be grown on top of each other without significant lattice distortion, making them suitable for superlattice growth. CaF_2 has already been discussed extensively in

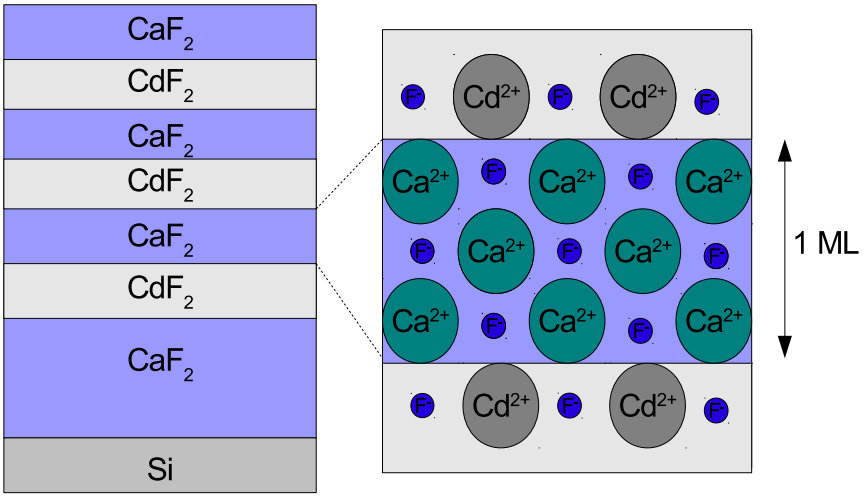

Figure 7.1 Schematic of the CdF_2–CaF_2 superlattice structure.

Chapter 6 of this thesis.

7.1.1 Cadmium Fluoride

CdF_2 has a cubic structure and a wide band gap of approximately 65 000 cm^{-1} [130]. The electronic and optical properties of CdF_2 differ significantly from CaF_2. Despite CdF_2 being an insulator, simple modifications result in vast changes to its electrical properties. Particularly, in spite of a large bandgap appropriately co-doped and annealed CdF_2 can have n-type semiconductor properties. In addition CdF_2 is known to demonstrate an efficient electroluminescence [131, 132] and due to its high density (6.38 g cm^{-3}) and relatively fast intrinsic emission decay time can be used as a scintillator [133, 134]. The CdF_2 lattice is well-matched to silicon, so allows for good epitaxial growth.

Limited research has been done towards an understanding of nature of CdF_2 intrinsic emission. Emission from bulk CdF_2 appears as a band from 19 000 to 34 000 cm^{-1}. Benci et al. [135] assigned it to recombination of a self-trapped hole (STH) with an electron. To establish the formation of STHs in CdF_2 further comprehensive study including EPR analysis is required. However, from the literature available we can assume the emission is excitonic in nature.

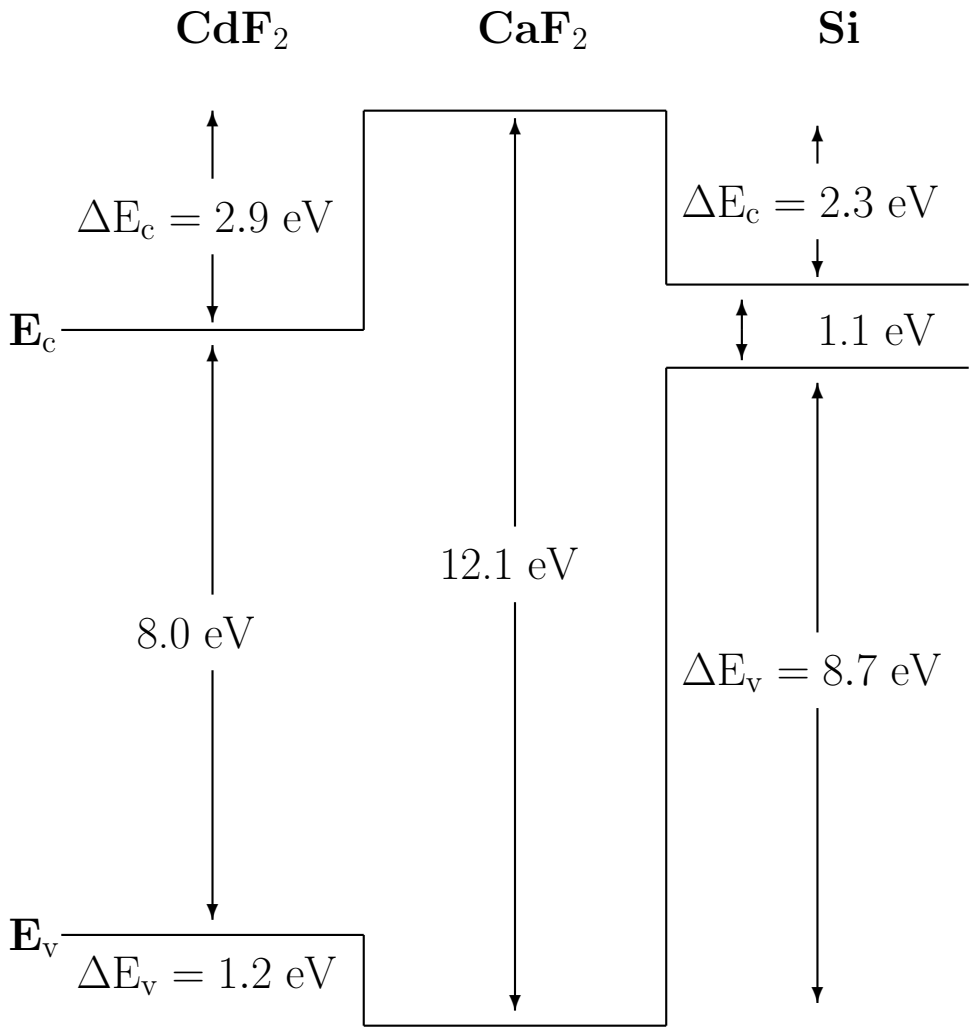

Figure 7.2 Energy-band diagram for the CdF_2-CaF_2-Si(111) heterostructure found by XPS [139].

7.1.2 Previous work on CdF_2-CaF_2 Superlattices

CdF_2–CaF_2 superlattices and heterostructures have been a subject of research for the last 20 years because of their potential for application in quantum devices such as resonant tunnelling diodes and quantum cascade lasers. A lot of work has gone into MBE fabrication techniques [127, 136–138]. In 1995, the energy-band offsets were measured with X-ray photoelectron spectroscopy by Izumi et al. [139] and are shown in Figure 7.2. There is a large conduction band discontinuity of the CdF_2-CaF_2 interface. Optical measurements in 1999 [128] showed a shift to higher energies prescribed to the interface mixing at the CaF_2-CdF_2 boundary [128].

Luminescence spectroscopic properties of Eu^{2+} and Eu^{3+} ions doped into CaF_2 mono-

layers (MLs) of CdF_2–CaF_2 and site symmetry characteristics for the dopant ions have been recently studied [77, 140]. The Eu ions act as optical probes in the superlattices. A 1999 study found experimental verification of a mechanism for interface tunelling related to Eu impurities [141] and bleaching of Eu^{2+} emission caused by tunneling-assisted photoionization of Eu has been investigated [142]. Stark energy levels of Eu^{3+} ions have been measured in Eu-doped CaF_2 MLs [143] and two distinctive Eu centers were observed [144].

7.2 Results

Figure 7.3 shows the time-integrated emission spectra of 5 ML and 3 ML CdF_2–CaF_2 superlattices recorded upon excitation at 62 500 cm^{-1} at temperatures 8, 60 and 200 K. At T = 8 K the spectra are represented by broad emission bands centred at 26 700 cm^{-1} for 5 ML and 28 200 cm^{-1} for 3 ML superlattices respectively. FWHM of emission bands for both 5 ML and 3 ML superlattices at T = 8 K is nearly the same at 6100 cm^{-1}. The intensity of emission from the superlattices dramatically decreases as temperature increases. Emission quenches above 200 K. Both 5 ML and 3 ML superlattices demonstrate a shift of emission band maxima towards lower energy for about 800 cm^{-1}, and broadening by about 15% when temperature increases from 8 to 200 K. Spectra recorded within slow and fast time gates closely follow the time-integrated spectra for both 5 ML and 3 ML superlattices, so they are not shown.

The top panel of Figure 7.3 displays the emission spectra of bulk CaF_2 and CdF_2 crystals for comparison. The time-integrated spectrum of CaF_2 was recorded at T = 8 K upon excitation at a frequency of 87 700 cm^{-1} that corresponds to maximum of excitonic absorption in CaF_2. The spectrum shows a broad band centred at about 34 800 cm^{-1} which corresponds to the STE emission discussed in Chapter 6. The STE emission band of CaF_2 experiences an insignificant (240 cm^{-1}) peak shift towards higher energy at T = 300 K due to the quenching of emission from the singlet component of the STE. Emission spectra of CdF_2 excited at X-ray and VUV energies at about 80 K were taken from published sources [145] using graph digitizing software.

Table 7.1(a) gives the peaks of the emission spectra presented in Figure 7.3. The spectral position and bandwidth of the emission observed from superlattices is very close to the intrinsic emission band reported for CdF_2. This is especially true for 5 ML superlattice if compared with the CdF_2 X-ray emission spectra.

The emission spectra of superlattices did not show any noticeable variation of the shape when taken under excitation at higher energy up to 170 000 cm^{-1}, suggesting that the STE emission of CaF_2 is quenched or not excited at all by VUV radiation in the superlattices studied. Thus, the emission spectra of the superlattices are determined by intrinsic emission of CdF_2 layers.

The 5 ML superlattice has emission which matches bulk CdF_2. The peak emission from the 3 ML sample has been shifted to a higher energy by about 1600 cm^{-1}. It is well known that confinement phenomena due to physical size and shape of the material strongly influence the nature and dynamics of electronic excitation. In particular, it has been shown that the energy of excitons in semiconductor nanoclusters increases as the size of the cluster decreases when the cluster size is of the same order as the excitations occuring in the material [146]. The shift in exciton emission indicates that the size of the bound e-h pair is similar to the size of the quantum well which contains it.

Previous work CdF_2–CaF_2 superlattices with thicker layers (2 nm and 20 nm, so around 6 ML and 60 ML respectively) showed a shift to higher energies prescribed to the mixing of CaF_2 and CdF_2 STE wavefunctions [128]. The results in Table 7.1 do not appear to show emission from CaF_2 STEs at all, and the change in peak energy is similar to the change in STE emission energy when decreasing the size of insulating nanoparticles [147].

Work on confined STEs in SiO_2 showed that the relationship between the energy of STE emission and confinement size could be approximated with a model based on Mott-Wannier excitons: [147]

$$\Delta E(D) = \frac{2\hbar^2\pi^2}{m^*_{\mathrm{e-h}} D^2}, \tag{7.1}$$

$$m^*_{\mathrm{e-h}} = \frac{m^*_{\mathrm{e}}\, m^*_{\mathrm{h}}}{m^*_{\mathrm{e}} + m^*_{\mathrm{h}}}, \tag{7.2}$$

where D is the exciton diameter and m^*_{e} and m^*_{h} are the reduced masses of the electrons and holes. Since the data available is so limited and the shift can only be estimated, it is not possible to calculate an accurate reduced mass. Fitting the 2 data points to Equation 7.1 gave a value of 2.5×10^{-28} kg. This value is clearly erroneous as it is much greater than the mass of an electron.

Figure 7.4 shows the excitation spectra for both superlattices. The top panels of Figure 7.4 show the excitation and reflection spectra of CdF_2 and CaF_2 single crystals for comparison

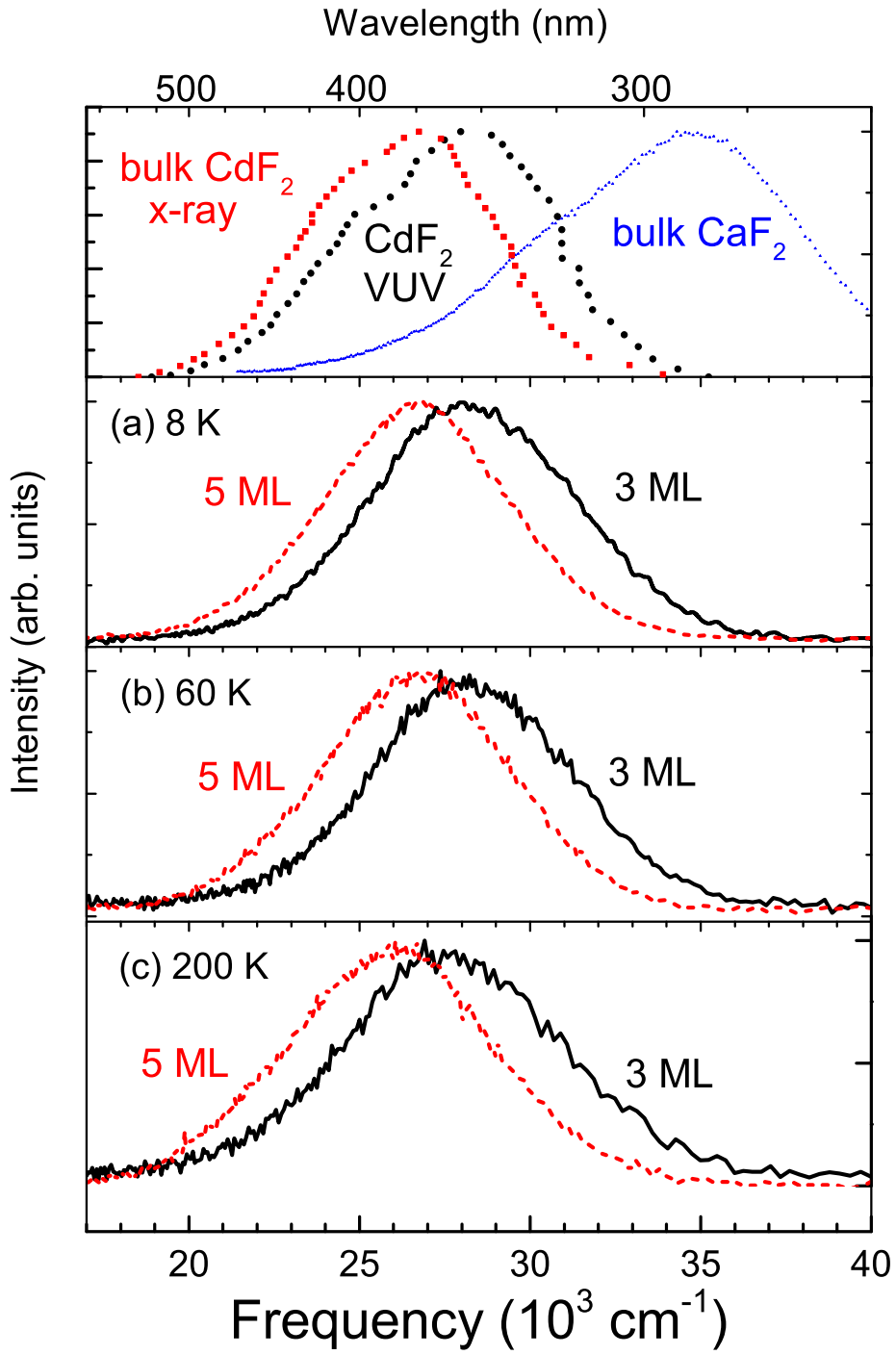

Figure 7.3 Emission spectra from CdF_2–CaF_2 superlattices recorded at a temperature range of 8 K to 150 K compared to the emission of bulk samples. The top panel shows low temperature emission from bulk CdF_2 after X-ray and VUV excitation [145] as well as low temperature bulk CaF_2 emission after VUV excitation as presented in Chapter 6.

Table 7.1 Peak position of intrinsic emission observed in CdF_2–CaF_2 superlattices.

(a) Emission				
Temperature (K)	3 ML	5 ML	CdF_2	CaF_2
8	28 200	26 800	-	34 800
60	28 000	26 700	28 300 [a]	-
200	27 500	26 000	-	-
300	quenched	quenched	25 700 [b]	35 100
(b) Excitation				
Temperature (K)	3 ML	5 ML	CdF_2	CaF_2
8	62 800	61 600	-	87 700
60	62 300	63 100	54 600 [a]	87 700
200	62 400	62 200	-	85 500
300	quenched	quenched	-	84 700

[a] 80 K VUV measurement from Fermi et al. [145];

[b] X-ray measurement by Rodnyĭ et al. [148].

with the excitation spectra of superlattices. The time-integrated excitation spectrum for CaF_2 crystal was recorded at T = 8 K monitoring STE emission at 34 800 cm^{-1}. Reflection spectra for CdF_2 and CaF_2 crystals as well as the excitation spectrum for CdF_2 intrinsic emission (all obtained at liquid nitrogen temperature) were extracted from published sources [105, 145, 149] using graph digitizing software. The position of the band edge peak in excitation spectrum of a CdF_2 single crystal from [145] agrees well with the position of the first maximum of the reflection spectrum observed at 65 000 cm^{-1} [130, 149, 150] which corresponds to an excitonic transition at the Γ point as confirmed by theoretical calculations [151].

The excitation spectrum of the CaF_2 single crystal taken at T = 8 K demonstrates an intense excitonic peak around 87 200 cm^{-1} which is followed by dramatic decrease of intensity at about 91 200 cm^{-1} as discussed in the previous chapter.

The excitonic peak in the CdF_2 spectrum is quite broad compared to the one in the CaF_2 spectrum. This broadness is likely to be connected with the binding energy of CdF_2 exciton (14 100 cm^{-1}) being double that of the CaF_2 exciton (7600 cm^{-1}). A greater binding energy indicates a greater configurational shift and broader emission. The increase in intensity of the intrinsic emission of CdF_2 observed at excitation energies

above 130 000 cm^{-1} is probably associated with photon multiplication. We note that CdF_2 is characterised by a valence band that is broader than the bandgap [152], which implies that the generation of secondary electronic excitations may be induced by both high-energy primary electrons and holes.

In Figure 7.4 we also display for comparison an excitation spectrum for STE emission in a CaF_2 bulk crystal. The CdF_2 spectrum does not show any features which could indicate an energy transfer from electronic excitation in CaF_2 MLs. The lack of CaF_2 excitation features, together with the lack of CaF_2 emission in Figure 7.3, suggests the VUV photons are substantially absorbed in the CdF_2 layers rather than the CaF_2 layers.

Table 7.1(b) compares the energy of the excitation peak corresponding to the exciton resonance in CdF_2–CaF_2 superlattices and CdF_2 and CaF_2 single crystals. The peak excitation for the superlattices is located at an energy about 6500 cm^{-1} higher relative to that observed for the CdF_2 single crystal.

Figure 7.5 shows decay curves for CdF_2 intrinsic emission of SLs recorded upon excitation at 62 100 cm^{-1} demonstrate departure from exponential behaviour. The deviation is most pronounced for the 3 ML sample.

Emission from the self-trapped exciton has been previously assigned to three states in alkali halides [153]. A long π recombination has been identified with a lifetime of several ms and assigned to a mix of B_{2g}, B_{1u} and B_{2u} states of the M_2X_2 alkali halide molecule. Two fast recombinations with lifetimes of ns and σ polarisation are suggested to be from a mix of B_{2g} and B_{3u} states which have different spin multiplicities. These three emission components can be fitted to the transients in Figure 3 by fitting two exponential functions for the σ components w ith lifetimes τ_1 and τ_2 and amplitudes A_1 and A_2, as well as an offset y_0 to represent the long π recombination.

The fitting parameters for the decay transients are given in Table 7.2. For the 5 ML sample at 150 K the time constants of the decays are 2.5 ns and 16.5 ns. These values are comparible to recent measurements of bulk CdF_2 decay after X-ray excitation at room temperature, where the constants were 1.75 ns and 25.5 ns [154]. The decay components are around twice as fast for the 3 ML than for 5 ML sample. For both quantum wells and quantum dots, lifetime is decreased and emission is blueshifted when compared to measurements in corresponding bulk materials. This is because the excitons have increased wavefunction overlap [155, 156].

The amplitude of the fast decay is greater for the 3 ML sample. For the 3 ML sample, the

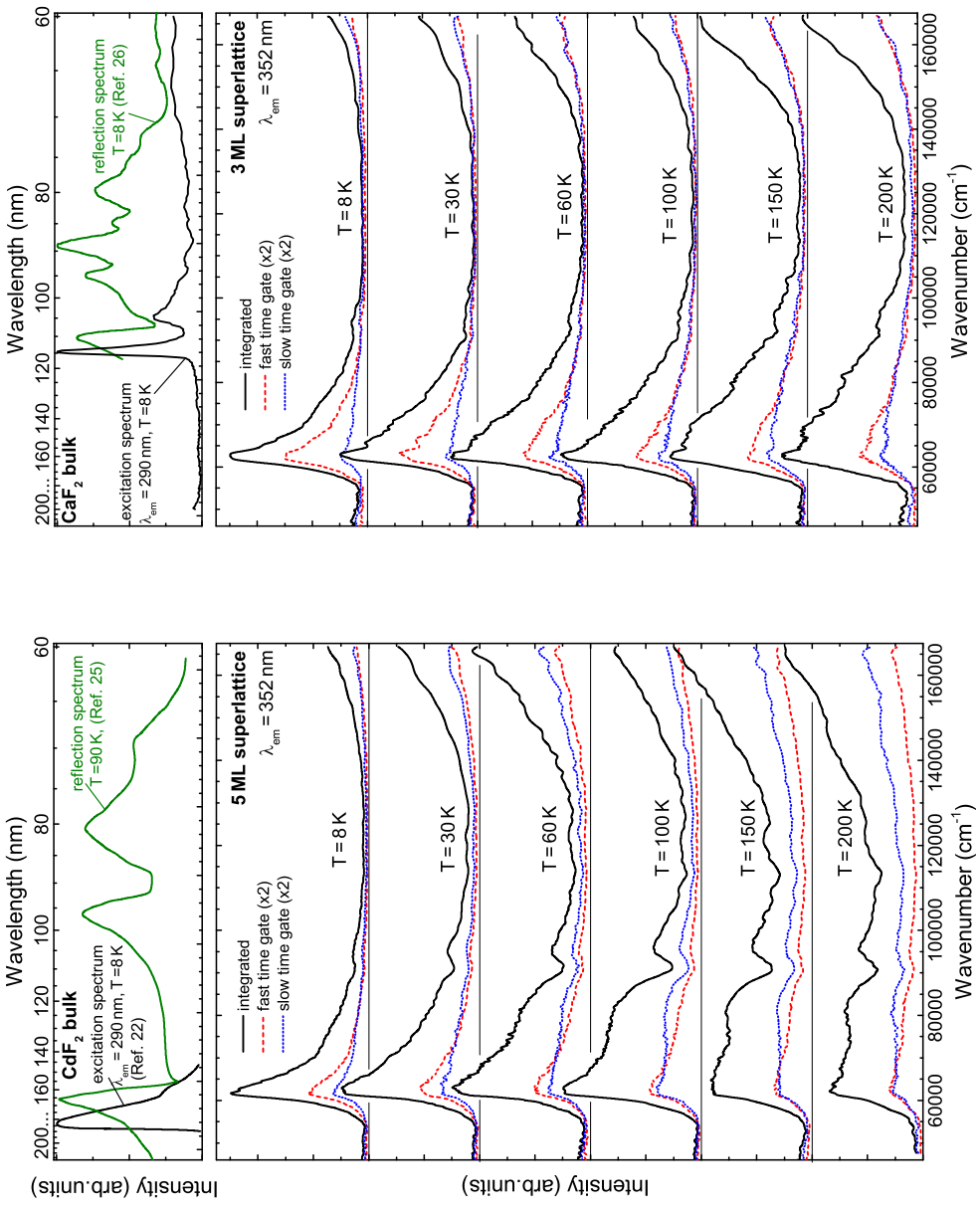

Figure 7.4 Excitation from CdF_2–CaF_2 superlattices monitored at the peak STE emission energy of 28 400 cm^{-1} compared to the emission of bulk samples. Fast time gate is 4–9 ns and the slow time gate is 46–70 ns.

Table 7.2 Parameters fitted to the superlattice emission transients shown in Figure 7.5. Dotted red lines are integrated over the fast time gate (2–9 ns) and blue lines are integrated over the slow time gate (46–70 ns).

	(a) 3 ML			
	8 K	60 K	100 K	150 K
Amplitude A_1	0.63 ± 0.02	0.732 ± 0.015	0.77 ± 0.02	0.725 ± 0.015
Lifetime τ_1 (ns)	1.84 ± 0.10	1.76 ± 0.13	1.60 ± 0.07	1.60 ± 0.07
Amplitude A_2	0.46 ± 0.02	0.39 ± 0.02	0.35 ± 0.02	0.36 ± 0.02
Lifetime τ_2 (ns)	9.0 ± 0.3	8.6 ± 0.3	9.4 ± 0.4	9.0 ± 0.6
Offset y_0	0.0500 ± 0.0008	0.0674 ± 0.0018	0.0799 ± 0.009	0.0815 ± 0.0008
	(b) 5 ML			
	8 K	60 K	100 K	150 K
Amplitude A_1	0.32 ± 0.02	0.35 ± 0.02	0.36 ± 0.03	0.38 ± 0.02
Lifetime τ_1 (ns)	3.2 ± 0.3	3.3 ± 0.3	3.0 ± 0.3	2.5 ± 0.2
Amplitude A_2	0.62 ± 0.03	0.56 ± 0.02	0.54 ± 0.02	0.48 ± 0.02
Lifetime τ_2 (ns)	20.4 ± 0.5	19.2 ± 0.6	18.6 ± 0.7	16.5 ± 0.5
Offset y_0	0.103 ± 0.003	0.144 ± 0.002	0.179 ± 0.003	0.167 ± 0.002

long lifetime does not change with temperature, while the short lifetime decreases slightly. For the 5 ML sample, both lifetimes decrease with temperature. The offset increases with temperature with both samples, which agrees with the observation that for alkali halides the σ components of the decay are quenched at a lower temperature than the π component [153].

7.3 Conclusion

The emission and excitation spectra of 3 ML and 5 ML CdF_2–CaF_2 superlattices under VUV excitation has been presented at sample temperatures from 8 K to 200 K. The decay of the emission was modeled with three components corresponding to STE states with different spin multiplicities. The temperature-dependence of the lifetimes are different for the two superlattices.

Our results on the VUV spectroscopy of CdF_2–CaF_2 super lattices show that the confinement effect seems to equally influence the energy of excitonic (and bandgap) absorption in 3 and 5 ML SLs. At the same time, energy of the self-trapped electronic excitations in

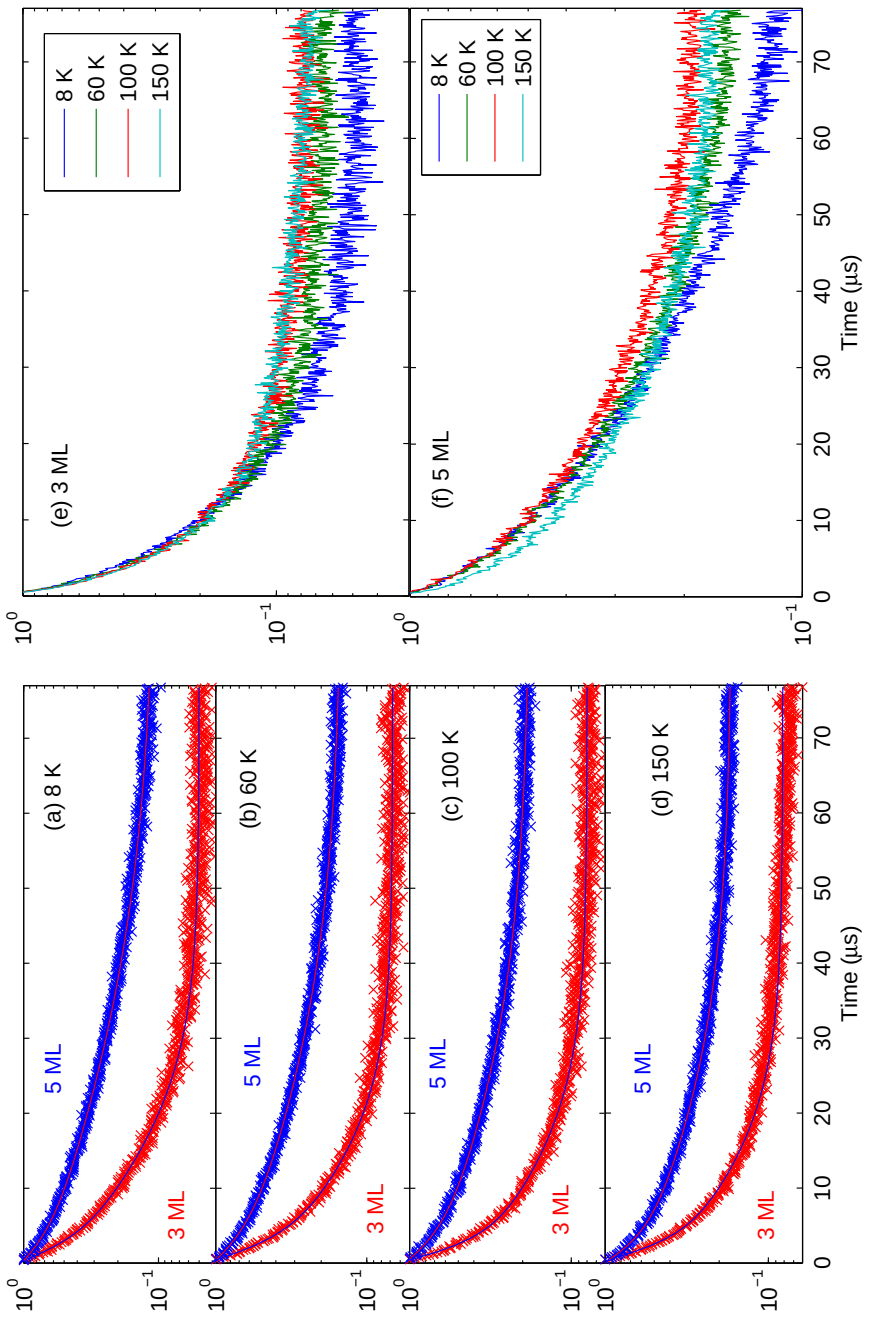

Figure 7.5 Emission decay kinetics from CdF_2–CaF_2 superlattices. For (a) to (d) the crosses are the decay transients and the lines are the double exponential fits using the parameters in table 7.2. (e) and (f) show the temperature evolution of the transients. The log scale illustrates that the decays are not single-exponential.

SLs shows a shift to higher energy by approximately 1600 cm^{-1}. This shift suggests the size of a bound e-h pair is comparible to the thickness of the layers of CdF_2.

Chapter 8

Conclusions and Future Work

This thesis has discussed intraconfigurational transitions and impurity-trapped excitons centred around divalent ytterbium ions, and self-trapped excitons in fluoride crystals. These excitations are processes which occur in phosphor applications. The novel application of two-colour and time-resolved vacuum-ultraviolet spectroscopic techniques to excitons in wide-bandgap fluoride crystals employed in this work has lead to a greater understanding of energy level structure of these excitations and energy-transfer processes between self-trapped excitons, ytterbium centres and impurity-trapped excitons.

In Chapter 5 of this thesis, electronic states within the ITE were successfully accessed and probed directly with the use of tunable IR excitation subsequent to setting up an excited population of ITEs with UV radiation. The two-colour excitation method excited energy levels within the ITE that would have otherwise remained inaccessible due to the broad featureless emission typically observed from ITEs.

Site-selective transient photoluminescence enhancement was measured in multi-site Yb^{2+}-doped $NaMgF_3$. Yb^{2+} ions in two sites of $NaMgF_3$:Yb^{2+} exhibited enhanced emission from impurity-trapped exciton states and we also observed electron trap liberation in both sites. A multi-level rate equation model was used to model the dynamics of the emission and the results were compared for both sites. The dominant process that contributed to the dynamical behaviour was intra-excitonic absorption and relaxation between three ITE levels. Two exciton energy levels were determined to be tens of wavenumbers apart and another level 950 cm^{-1} from the exciton ground state was identified. The model showed electron trap liberation was an important mechanism by which IR radiation increases population in the ITE energy levels. By analysing the difference in emission intensity before and after the IR pulse the electron trap depth was found to be approximately 800 cm^{-1} . A moderate increase in lattice temperature was inferred from the modelling.

Most previous work on ITEs has lacked quantitative analysis due to ITEs being charac-

terised by high energies, broad transitions, relatively rapid non-radiative relaxation, and difficulty in distinguishing ITE states from other highly excited states, such as mixed configurations of the rare-earth impurities. To overcome these difficulties, the work in this thesis employed two-photon spectroscopy using the tunable IR capabilities of a free-electron laser, site-selective excitation, and detailed modeling of the multisite and multilevel relaxation dynamics. Aspects of the material properties that are important for high-energy luminescence applications such as scintillators were studied and interpreted. This work provides valuable insight into the relaxation dynamics of trapped electron-hole pairs and their interaction with their local environment, including localized transient heating and population-depopulation of charge traps intrinsic to the host lattice itself.

The site-selective transient photoluminescence enhancement method could be used in future work to probe similar complicated systems to extract fundamental properties of the states. Other materials which exhibit anomolous emission that may originate from ITE states can be measured, and quantative information about the ITE states extracted and compared for different host materials. This method could also be used to verify the position of $5d$ levels in lanthanides where there is direct $4f^n \rightarrow 4f^{n-1}5d^1$ transitions. The two-colour method can be used to investigate any other kind of temporary defect of a crystal system which emits a broad band on a similar timescale.

Chapter 6 of this thesis presented the results of the excitation of single crystals of CaF_2:Yb, $NaMgF_3$:Yb and MgF_2:Yb by UV-VUV synchrotron radiation excitation. Emission from ITEs or $4f^{13}5d$ configurations has been identified in all three materials. Excitation into the fundamental absorption band of the crystals results in emission from intrinsic states and Yb impurity centres. The interplay between intrinsic distortions and Yb impurity centres was observed and analysed with changing excitation energy and temperature.

Emission bands due to both ITE and STE states were observed when the CaF_2:Yb crystal was excited at an energy to optimally create free excitons, suggesting that the free excitons became trapped as STEs, which then went on to relax radiatively or create ITEs via energy transfer to the Yb^{2+} impurity centres. The temperature dependence of the peak resonant absorption of the free exciton has been measured and was explained by considering the change in band gap with temperature through Viña's equation. The behaviour of the emission with different concentrations of Yb has been explained.

A similar result to CaF_2:Yb was found when $NaMgF_3$:Yb was excited at an energy to optimally create free excitons: emission bands due to both ITE and STE states are observed, so in $NaMgF_3$:Yb^{2+} free excitons decay to STEs, which then go on to relax radiatively

or excite Yb^{2+} ions to ITE states. Unlike CaF_2:Yb where the ITE and STE emission bands are separated by a few thousand wavenumbers; in $NaMgF_3$:Yb the emission bands from ITE and STE states overlap each other. The emission bands were deconvolved by modeling them as Gaussian functions, and the comparitive emission intensity from each band was estimated. The ITE emission approximately doubled in comparison to STE emission as the excitation energy was increased from the intrinsic exciton resonance peak to the conduction band. Along with room temperature excitation measurements this was presented as evidence that emitting ITE states were also created through energy transfer from conduction band states which does not involve STE states.

The excitation spectrum of $NaMgF_3$:Yb presented in Chapter 6 contained the Yb^{2+} $4f^{n-1}5d^1 \rightarrow 4f^n$ transitions. This spectrum was fitted to a semi-emperical crystal field model where the Yb^{2+} site geometry was assumed to be a latitudinally-distorted tetragonal symmetry. The crystal field parameters were compared to previous work on CaF_2 and $SrCl_2$. The B^4 parameter is almost half the value found for CaF_2.

In MgF_2:Yb emission bands due to both Yb^{2+} centres and STE states were observed. The emission from Yb^{2+} was deemed more likely to be $4f^n \rightarrow 4f^{n-1}5d^1$ emission rather than a transition from an ITE state.

The excitation spectra of CaF_2:Yb, $NaMgF_3$:Yb and MgF_2:Yb were compared, and the increased peak energy of the free exciton peak from CaF_2 to $NaMgF_3$ to MgF_2 was explained as the combination of the influence of the changing band gap between the materials, which increases with decreasing lattice constants from CaF_2 to MgF_2 to $NaMgF_3$, and the difference in binding energy of the free excitons, which increases with the size of the ionic radii of cations in the lattice from $NaMgF_3$ to CaF_2 to MgF_2.

The difference in free exciton peak position between CaF_2 monitored at the peak ITE emission and STE emission was measured as 1500 cm^{-1}. This difference was not seen for $NaMgF_3$ or MgF_2, which was explained as being likely due to the overlap between the ITE and STE emission bands making it difficult to distinguish emission from either excitation for $NaMgF_3$ and MgF_2.

The interaction between crystal host excitations and luminescent centres is an important area of research due to the importance these processes have to scintillators and phosphors. No previous work has been performed on the interaction on ITEs and STEs, despite both excitations being present in many scintilator excitation processes. In this thesis, SUPERLUMI is used as a specialist high-intensity VUV source to probe the energies at

which both excitations are created.

Useful experiments on the UV-VUV synchrotron radiation excitation of alkaline earth halides could build upon the measurements presented here. Other fluoride systems could be investigated, as well as Eu^{2+}-doped systems in which ITEs are likely to form, in order to build upon the model of the dynamics between host lattices and ITEs.

In chapter 7 results on VUV spectroscopy of 5 ML and 3 ML CdF_2–CaF_2 superlattices showed the change in behaviour of the STE in CdF_2 when it is confined and give an indication of the radius of the exciton. There was a distinct change in the emission characteristics of the CdF_2 exciton between the 5 ML and 3 ML CdF_2–CaF_2 superlattices. As the STE was more confined, the emission was blue-shifted by 1600 cm^{-1}. The decay of the emission was modeled with three components corresponding to STE states with different spin multiplicities. The lifetime of the decay decreased when the STE was confined. Our results on the VUV spectroscopy of CdF_2–CaF_2 super lattices show that the confinement effect seems to equally influence the energy of excitonic (and bandgap) absorption in 3 and 5 ML SLs. At the same time, energy of the self-trapped electronic excitations in SLs showed a noticeable difference in the samples that indicates the size of a bound e-h pair is commensurable with the thickness of the layers of CdF_2.

Future experiments could use higher energy excitation to try and selectively excite the CaF_2 layers of the superlattice, since CaF_2 is a more common material than CdF_2 and more is known about the CaF_2 STE.

An extension of the study of STEs under two-dimensional confinement in superlattices would be to investigate three-dimensional confinement of ITEs in Yb-doped fluoride nanocrystals. Interesting comparisons could be made between the experiments on bulk samples reported in this thesis and experiments on nanocrystal systems.

References

[1] B. J. Ainslie, *A review of the fabrication and properties of erbium-doped fibers for optical amplifiers*, *J. Lightwave Technol.* **9** (1991), no. 2 220–227.

[2] G. Blasse, *Scintillator materials*, *Chem. Mat.* **6** (1994), no. 9 1465–1475.

[3] M. J. Weber, *Inorganic scintillators: today and tomorrow*, *J. Lumin.* **100** (2002), no. 1 35–45.

[4] P. Pust, V. Weiler, C. Hecht, A. Tücks, A. S. Wochnik, A.-K. Henß, D. Wiechert, C. Scheu, P. J. Schmidt, and W. Schnick, *Narrow-band red-emitting $SrLiAl_3N_4$: Eu^{2+} as a next-generation LED-phosphor material*, *Nat. Mater.* (2014).

[5] Y.-J. You, C.-H. Lin, A. Zaytsev, F.-H. Tsai, C.-L. Wang, and C.-L. Pan, *Optimal design of a high-power picosecond laser system using a dual-stage ytterbium-doped fibre amplifier*, *Laser Phys.* **23** (2013), no. 7 075114.

[6] M. Grinberg and S. Mahlik, *Impurity-trapped excitons: Experimental evidence and theoretical concept*, *J. Non-Cryst. Solids* **354** (2008), no. 35 4163–4169.

[7] G. Sánchez-Sanz, L. Seijo, and Z. Barandiarán, *Energy gaps in the $4f^{13}5d^1$ manifold and multiple spontaneous emissions in Yb^{2+}-doped $CsCaBr_3$*, *J. Phys. Chem. A* **113** (2009), no. 45 12591–12598.

[8] S. Lizzo, A. Meijerink, G. Dirksen, and G. Blasse, *On the luminescence of divalent ytterbium in $KMgF_3$ and $NaMgF_3$*, *J. Phys. Chem. Solids* **56** (1995), no. 7 959 – 964.

[9] P. Dorenbos, *Anomalous luminescence of Eu^{2+} and Yb^{2+} in inorganic compounds*, *J. Phys. Cond. Matter* **15** (2003) 2645.

[10] R. Williams and K. Song, *The self-trapped exciton*, *J. Phys. Chem. Solids* **51** (1990), no. 7 679–716.

[11] S. Ismail-Beigi and S. G. Louie, *Self-trapped excitons in silicon dioxide: mechanism and properties*, *Phys. Rev. Lett.* **95** (2005), no. 15 156401.

[12] B. G. Wybourne, *Effective operators and spectroscopic properties*, *J. Chem. Phys.* **48** (1968), no. 6 2596–2611.

[13] S. V. Eliseeva and J.-C. G. Bünzli, *Rare earths: jewels for functional materials of the future*, *New J. Chem.* **35** (2011), no. 6 1165–1176.

[14] P. Dorenbos, *f d transition energies of divalent lanthanides in inorganic compounds*, *J. Phys. Condens. Matter* **15** (2003), no. 3 575.

[15] P. Dorenbos, *The 5d level positions of the trivalent lanthanides in inorganic compounds*, *J. Lumin.* **91** (2000), no. 3 155–176.

[16] L. Van Pieterson, M. Reid, R. Wegh, S. Soverna, and A. Meijerink, *4 f ^{n} → 4 f $^{n-1}$ 5 d transitions of the light lanthanides: Experiment and theory*, *Phys. Rev. B* **65** (2002), no. 4 045113.

[17] L. Van Pieterson, M. Reid, G. W. Burdick, and A. Meijerink, *4 f ^{n} → 4 f $^{n-1}$ 5 d transitions of the heavy lanthanides: Experiment and theory*, *Phys. Rev. B* **65** (2002), no. 4 045114.

[18] G. H. Dieke, H. M. Crosswhite, and H. Crosswhite, *Spectra and energy levels of rare earth ions in crystals*. Interscience Publishers, New York, 1968.

[19] R. T. Wegh, A. Meijerink, R.-J. Lamminmäki, and J. Hölsä, *Extending Dieke's diagram*, *J. Lumin.* **87** (2000) 1002–1004.

[20] T. Piper, J. Brown, and D. McClure, *fd and f^{13}d configurations in a crystal field, and the spectrum of yb++ in cubic crystals*, *J. Chem. Phys.* **46** (1967), no. 4 1353–1358.

[21] D. S. McClure and C. Pedrini, *Excitons trapped at impurity centers in highly ionic crystals*, *Phys. Rev. B* **32** (1985), no. 12 8465.

[22] A. Kaplyanskii and P. Feofilov, *The spectra of divalent rare earth ions in crystals of alkaline earth fluorides. ii. Europium and ytterbium*, *Opt. Spectrosc.* **13** (1962) 129.

[23] E. Reut, *Luminescence of divalent Eu and Yb ions in fluorite-type crystals*, *Opt. Spectrosc.* **40** (1976) 55–57.

[24] A. Kaplyanskii, V. Medvedev, and P. Smolyanskii, *Spectra, kinetics, and polarization of the luminescence of CaF_2-Yb^{2+} crystals*, *Opt. Spectrosc.* **41** (1976) 615–619.

[25] R. Greene, D. Sell, and G. Imbusch, *Optical fluorescence from impurity-trapped excitons in MnF_2*, *Solid State Commun.* **5** (1967), no. 9.

[26] B. Moine, B. Courtois, and C. Pedrini, *Luminescence and photoionization processes of Yb^{2+} in CaF_2, SrF_2 and BaF_2*, *J. Phys.* **50** (1989), no. 15 2105–2119.

[27] B. Moine, B. Courtois, and C. Pedrini, *Fluorescence, photoconductivity and polarization properties of divalent rare earth ions in fluoride crystals*, *J. Lumin.* **45** (1990), no. 1 248–250.

[28] M. F. Reid, P. S. Senanayake, J.-P. R. Wells, G. Berden, A. Meijerink, A. J. Salkeld, C.-K. Duan, and R. J. Reeves, *Transient photoluminescence enhancement as a probe of the structure of impurity-trapped excitons in CaF_2: Yb^{2+}*, *Phys. Rev. B* **84** (2011), no. 11 113110.

[29] P. S. Senanayake, *Two–Colour Excitation of Impurity Trapped Excitons in Wide Bandgap Insulators*. PhD thesis, University of Canterbury, New Zealand, 2013.

[30] E. Rönnebro, D. Noréus, K. Kadir, A. Reiser, and B. Bogdanovic, *Investigation of the perovskite related structures of $NaMgH_3$, $NaMgF_3$ and $NaAlH_6$*, *J. Alloys Compd.* **299** (2000), no. 12 101 – 106.

[31] J. Gâcon, A. Gros, H. Bill, and J. Wicky, *New measurements of the emission spectra of Sm^{2+} in $KMgF_3$ and $NaMgF_3$ crystals*, *J. Phys. Chem. Solids* **42** (1981), no. 7 587–593.

[32] W. Zhang, H. Seo, B. Moon, S. Yi, and K. Jang, *Site-selective fluorescence excitation spectroscopy of a $KMgF_3$: Sm^{2+} crystal*, *J. Alloys Compd.* **374** (2004), no. 1 32–35.

[33] P. S. Senanayake, J.-P. R. Wells, M. F. Reid, G. Berden, A. Meijerink, and R. J. Reeves, *Electron trap liberation in MgF_2 doped with Yb^{2+} using a two-color excitation experiment*, *Appl. Phys. Lett.* **100** (2012), no. 4 041902.

[34] P. Dorenbos, *Systematic behaviour in trivalent lanthanide charge transfer energies*, *J. Phys. Cond. Matt.* **15** (2003), no. 49 8417.

[35] L. Van Pieterson, M. Heeroma, E. De Heer, and A. Meijerink, *Charge transfer luminescence of Yb^{3+}*, *Journal of Luminescence* **91** (2000), no. 3 177–193.

[36] F. Seitz, *Color centers in alkali halide crystals*, *Rev. Mod. Phys.* **26** (Jan, 1954) 7–94.

[37] M. Kabler, *Low-temperature recombination luminescence in alkali halide crystals*, *Phys. Rev.* **136** (1964), no. 5A A1296.

[38] R. Murray and F. Keller, *Recombination luminescence from V_K centers in potassium iodide*, *Phys. Rev.* **137** (1965), no. 3A A942.

[39] M. Kabler and D. Patterson, *Evidence for a triplet state of the self-trapped exciton in alkali-halide crystals*, *Phys. Rev. Lett.* **19** (1967), no. 11 652.

[40] H. N. Hersh, *Proposed excitonic mechanism of color-center formation in alkali halides*, *Phys. Rev.* **148** (1966), no. 2 928.

[41] N. Itoh, A. M. Stoneham, and A. H. Harker, *The initial protection of defects in alkali halides: F and H centre production by non-radiative decay of the self-trapped exciton*, *J. Phys. C: Solid State Phys.* **10** (1977), no. 21 4197.

[42] R. Williams, M. Kabler, W. Hayes, and J. Stott, *Time-resolved spectroscopy of self-trapped excitons in fluorite crystals*, *Phys. Rev. B* **14** (1976), no. 2 725.

[43] J. Beaumont, W. Hayes, D. Kirk, and G. Summers, *An investigation of trapped holes and trapped excitons in alkaline earth fluorides*, *Proc. R. Soc. A.* **315** (1970), no. 1520 69–97.

[44] W. Hayes, *Crystals with the Fluorite Structure: Electronic, Vibrational, and Defect Properties*. The International series of monographs on physics. Oxford University Press, Incorporated, 1974.

[45] F. Agulló-López, C. R. A. Catlow, and P. D. Townsend, *Point defects in materials*, vol. 149. Academic Press London, 1988.

[46] W. Hayes and J. Twidell, *The self-trapped hole in CaF_2*, *Proc. Phys. Soc.* **79** (1962), no. 6 1295.

[47] P. Call, W. Hayes, and M. Kabler, *Optical detection of exciton EPR in fluorite crystals*, *J. Phys. C* **8** (1975), no. 4 L60.

[48] M. Adair, C. Leung, and K. Song, *Equilibrium configuration of the self-trapped exciton in CaF_2 and SrF_2*, *J. Phys. C* (1985), no. 28 L909.

[49] W. Hayes, I. Owen, and G. Pilipenko, *Optical detection of exciton EPR in $KMgF_3$*, *J. Phys. C* **8** (1975), no. 19 L407.

[50] G. Huang, L. Chen, M. Liu, and D. Xing, *Intrinsic defects in $KMgF_3$: the ab initio and the extended-ion study*, *J. Phys. Condens. Matter* **15** (2003), no. 26 4567.

[51] L. Chen, L. Zhou, and K. Song, *A study of the self-trapped exciton and F centre in MgF_2*, *J. Phys. Condens. Matter* **9** (1997), no. 31 6633.

[52] Y. Toyozawa, *A proposed model of excitonic mechanism for defect formation in alkali halides*, *J. Phys. Soc. Jpn.* **44** (1978), no. 2 482–488.

[53] J. Fischbach, D. Fröhlich, and M. Kabler, *Recombination luminescence lifetimes and the self-trapped excition in alkali halides*, *J. Lumin.* **6** (1973), no. 1 29–43.

[54] D. Pooley and W. Runciman, *Recombination luminescence in alkali halides*, *J. Phys. C* **3** (1970), no. 8 1815.

[55] J. Becker, M. Kirm, V. Kolobanov, V. Makhov, V. Mikhailin, A. Vasil'ev, and G. Zimmerer, *Coexistence of triplet and singlet exciton emission in alkaline earth fluoride crystals*, *J. Electrochem. Soc.* (1998) 415–419.

[56] E. Van der Kolk, P. Dorenbos, C. Van Eijk, A. Vink, M. Weil, and J.-P. Chaminade, *Luminescence excitation study of the higher energy states of Pr^{3+} and Mn^{2+} in $SrAlF_5$, $CaAlF_5$, and $NaMgF_3$*, *J. Appl. Phys.* **95** (2004), no. 12 7867–7872.

[57] R. Williams, C. Marquardt, J. Williams, and M. Kabler, *Transient absorption and luminescence in MgF_2 following electron pulse excitation*, *Phys. Rev. B* **15** (1977), no. 10 5003.

[58] L. Lisitsyna, V. Korepanov, and T. Grechkina, *Effect of temperature on processes of radiation-induced generation of primary defects in MgF_2 crystals*, *Opt. Spectrosc.* **95** (2003), no. 5 746–750.

[59] A. Fix, F. Abuova, R. Eglitis, E. Kotomin, and A. Akilbekov, *Ab initio calculations of the F centers in MgF_2 bulk and on the (001) surface*, *Phys. Scripta* **86** (2012), no. 3 035304.

[60] V. Kolobanov, V. Mikhailin, S. Chernov, D. Spassky, V. Makhov, M. Kirm, E. Feldbach, and S. Vielhauer, *Luminescence of singlet self-trapped excitons in MgF_2*, *J. Phys. Condens. Matter* **21** (2009), no. 37 375501.

[61] K. Stevens, *Matrix elements and operator equivalents connected with the magnetic properties of rare earth ions*, *Proceedings of the Physical Society. Section A* **65** (1952), no. 3 209.

[62] D. Newman and B. Ng, *The superposition model of crystal fields*, *Rep. Prog. Phys.* **52** (1989), no. 6 699.

[63] H. Crosswhite and D. Newman, *Spin-correlated crystal field parameters for lanthanide ions substituted into $LaCl_3$*, *J. Chem. Phys.* **81** (1984), no. 11 4959–4962.

[64] C. Görller-Walrand and K. Binnemans, *Rationalization of crystal-field parametrization*, in *Handbook on the physics and chemistry of rare earths, Vol. 23* (K. G. Jr. and L. Eyring, eds.). Elsevier Science, Amsterdam, 1996.

[65] M. Reid, L. Van Pieterson, and A. Meijerink, *Trends in parameters for the $4f^N \rightarrow 4f^{N-1}$ 5d spectra of lanthanide ions in crystals*, *J. Alloys Compd.* **344** (2002), no. 1 240–245.

[66] Z. Barandiarán and L. Seijo, *The ab initio model potential method. Cowan-Griffin relativistic core potentials and valence basis sets from Li (Z= 3) to La (Z= 57)*, *Can. J. Chem.* **70** (1992), no. 2 409–415.

[67] J. L. Pascual, J. Schamps, Z. Barandiarán, and L. Seijo, *Large anomalies due to insufficiency of Madelung embedding in ab initio calculations of 4f-5d and 4f-6s excitations of lanthanides in ionic crystals: The BaF_2:Ce^{3+} crystal*, *Phys. Rev. B* **74** (2006), no. 10 104105.

[68] A. J. Salkeld, M. F. Reid, J.-P. R. Wells, G. Sánchez-Sanz, L. Seijo, and Z. Barandiarán, *Effective hamiltonian parameters for ab initio energy-level calculations of $SrCl_2$: Yb^{2+} and $CsCaBr_3$:Yb^{2+}*, *J. Phys. Cond. Matt.* **25** (2013), no. 41 415504.

[69] L. Hu, M. F. Reid, C.-K. Duan, S. Xia, and M. Yin, *Extraction of crystal-field parameters for lanthanide ions from quantum-chemical calculations*, *J. Phys. Cond. Matt.* **23** (2011), no. 4 045501.

[70] D. J. Newman and B. Ng, *Crystal field handbook*. Cambridge University Press, The Edinburgh Building, Cambridge University, 2007.

[71] V. Petit, P. Camy, J.-L. Doualan, X. Portier, and R. Moncorgé, *Spectroscopy of Yb^{3+}: CaF_2: From isolated centers to clusters*, *Phys. Rev. B* **78** (2008), no. 8 085131.

[72] G. Liu and B. Jacquier, *Spectroscopic properties of rare earths in optical materials*, vol. 83. Springer, 2006.

[73] B. Henderson and G. F. Imbusch, *Optical Spectroscopy of Inorganic Solids*. Oxford University Press, 1989.

[74] G. Sánchez-Sanz, L. Seijo, and Z. Barandiarán, *Yb^{2+}-doped $SrCl_2$: Electronic structure of impurity states and impurity-trapped excitons*, *J. Chem. Phys.* **133** (2010), no. 11 114509.

[75] R. B. Hughes-Currie, A. J. Salkeld, K. V. Ivanovskikh, M. F. Reid, J.-P. R. Wells, and R. J. Reeves, *Excitons and interconfigurational transitions in CaF_2: Yb^{2+} crystals*, *J. Lumin.* **158** (2015) 197–202.

[76] S. Lizzo, A. Meijerink, G. Dirksen, and G. Blasse, *Luminescence of divalent ytterbium in magnesium fluoride crystals*, *J. Lumin.* **63** (1995), no. 5 223–234.

[77] J. K. Choi, *Laser Spectroscopy of Eu Centres in MBE Grown CaF_2:Eu-CdF_2 Superlattices and CaF_2:Eu Thin Films*. PhD thesis, University of Canterbury, New Zealand, 2009.

[78] M. Newville, *Fundamentals of XAFS*, *Rev. Mineral. Geochem.* **78** (2014), no. 1 33–74.

[79] S. Heald, D. Brewe, E. Stern, K. Kim, F. Brown, D. Jiang, E. Crozier, and R. Gordon, *XAFS and micro-XAFS at the PNC-CAT beamlines*, *J. Synchrotron Radiat.* **6** (1999), no. 3 347–349.

[80] D. Oepts, A. Van der Meer, and P. Van Amersfoort, *The free-electron-laser user facility FELIX*, *Infrared Phys. Technol.* **36** (1995), no. 1 297–308.

[81] G. Zimmerer, *SUPERLUMI: A unique setup for luminescence spectroscopy with synchrotron radiation*, *Radiat. Meas.* **42** (2007), no. 4 859–864.

[82] E. Negodine, *Inter-and intraconfigurational luminescence of $LiYF_4$: Er^{3+} under selective VUV excitation*. PhD thesis, DESY, 2003.

[83] E. Johnson and L. T. Chadderton, *Anion voidage and the void superlattice in electron irradiated CaF_2*, *Rad. Effects* **79** (1983), no. 1-4 183–233.

[84] D. Bingham, A. Cormack, and C. Catlow, *Rigid-ion potentials for SrF_2, CaF_2 and GdF_3*, *J.Phys. Cond. Matter* **1** (1989), no. 7 1205.

[85] W. H. Baur and A. A. Khan, *Rutile-type compounds. IV. SiO_2, GeO_2 and a comparison with other rutile-type structures*, *Acta Crystallogr. Sect. B* **27** (1971), no. 11 2133–2139.

[86] L. Zhen-Li, A. Xin-You, C. Xin-Lu, W. Xue-Min, Z. Hong, P. Li-Ping, and W. Wei-Dong, *First-principles study of the electronic structure and optical properties of cubic perovskite $NaMgF_3$*, *Chin. Phys. B* **23** (2014), no. 3 037104.

[87] J. Kirton and A. White, *Zeeman effect in the absorption spectra of trivalent ytterbium ions in different site symmetries in calcium fluoride*, *Phys. Rev.* **178** (1969), no. 2 543.

[88] N. Kristianpoller and B. Trieman, *Colour centres in alkali halides: Defects induced in $NaMgF_3$ crystals by X-and VUV-irradiation*, *J. Phys. Colloques* **41** (1980), no. C6 C6–109.

[89] G. A. Waychunas, *Synchrotron radiation XANES spectroscopy of Ti in minerals: effects of Ti bonding distances, Ti valence, and site geometry on absorption edge structure*, *Am. Mineral.* **72** (1987) 89–101.

[90] M. Benfatto and C. Meneghini, *A close look into the low energy region of the XAS spectra: The XANES region*, in *Synchrotron Radiation*, pp. 213–240. Springer, 2015.

[91] J. J. Rehr, J. J. Kas, F. D. Vila, M. P. Prange, and K. Jorissen, *Parameter-free calculations of X-ray spectra with FEFF9*, *Phys. Chem. Chem. Phys.* **12** (2010), no. 21 5503–5513.

[92] L. Soderholm, G. Liu, M. R. Antonio, and F. Lytle, *X-ray excited optical luminescence (XEOL) detection of x-ray absorption fine structure (XAFS)*, *J. Chem. Phys.* **109** (1998), no. 16 6745–6752.

[93] P. Willmott, *An introduction to synchrotron radiation: Techniques and applications*. John Wiley & Sons, 2011.

[94] B. Ravel and M. Newville, *ATHENA and ARTEMIS: Interactive graphical data analysis using IFEFFIT*, *Phys. Scripta* **2005** (2005), no. T115 1007.

[95] A. Fuse, G. Nakamoto, M. Kurisu, N. Ishimatsu, and H. Tanida, *The valence state of Yb metal under high pressure determined by XANES measurement up to 34.6 GPa*, *J. Alloys Comp.* **376** (2004), no. 1 34–37.

[96] M. Antonio, L. Soderholm, and I. Song, *Design of spectroelectrochemical cell for in situ X-ray absorption fine structure measurements of bulk solution species*, *J. Appl. Electrochem.* **27** (1997), no. 7 784–792.

[97] I. Nicoara, M. Stef, and A. Pruna, *Growth of YbF_3-doped CaF_2 crystals and characterization of Yb^{3+}–Yb^{2+} conversion*, *J. Crys. Growth* **310** (2008), no. 7 1470–1475.

[98] D. B. Gatch, D. Boye, Y. Shen, M. Grinberg, Y. Yen, and R. Meltzer, *Pressure dependence of the impurity-trapped exciton emission in BaF_2:Eu and $Ba_{\mathrm{x}}Sr_{1-\mathrm{x}}F_2$:Eu*, *Phys. Rev. B* **74** (2006), no. 19 195117.

[99] M. Karbowiak, A. Urbaniowicz, and M. F. Reid, *$4f^6 \rightarrow 4f^5 5d^1$ absorption spectrum analysis of Sm^{2+}: $SrCl_2$*, *Phys. Rev. B* **76** (2007) 115125.

[100] P. Senanayake, J. Wells, M. Reid, G. Berden, A. Meijerink, and R. Reeves, *Impurity-trapped excitons and electron traps in CaF_2:Yb^{2+} and SrF_2:Yb^{2+} probed by transient photoluminescence enhancement*, *J. Lumin.* **133** (2013), no. 0 81 – 85.

[101] N. Ashcroft and N. Mermin, *Solid State Physics*. Cengage Learning, 2011.

[102] J. Andruszkow, B. Aune, V. Ayvazyan, N. Baboi, R. Bakker, V. Balakin, D. Barni, A. Bazhan, M. Bernard, A. Bosotti, et al., *First observation of self-amplified spontaneous emission in a free-electron laser at 109 nm wavelength*, *Phys. Rev. Lett.* **85** (2000), no. 18 3825.

[103] C. W. King and O. H. Nestor, *Calcium fluoride: new properties for an old material*, in *OE/LASE'89, 15-20 Jan., Los Angeles. CA*, pp. 80–86, International Society for Optics and Photonics, 1989.

[104] T. Tomiki and T. Miyata, *Optical studies of alkali fluorides and alkaline earth fluorides in VUV region*, *J. Phys. Soc. Japan* **27** (1969), no. 3 658–678.

[105] G. W. Rubloff, *Far-ultraviolet reflectance spectra and the electronic structure of ionic crystals*, *Phys. Rev. B* **5** (1972), no. 2 662.

[106] V. Denks, T. Savikhina, and V. Nagirnyi, *Dependence of luminescence processes and transmission in vacuum-ultraviolet region on surface condition in CaF_2 single crystals*, *Appl. Surf. Sci.* **158** (2000), no. 3 301–309.

[107] E. Radzhabov and A. Nepomnyashchikh, *Charge-transfer bands in alkaline-earth fluoride crystals doped by Eu^{3+} or Yb^{3+} ions*, *Solid State Commun.* **146** (2008), no. 9 376–379.

[108] K. ODonnell and X. Chen, *Temperature dependence of semiconductor band gaps*, *Applied Physics Letters* **58** (1991), no. 25 2924–2926.

[109] M. Cardona and R. Kremer, *Temperature dependence of the electronic gaps of semiconductors*, *Thin Solid Films* (in press).

[110] L. Vina, S. Logothetidis, and M. Cardona, *Temperature dependence of the dielectric function of germanium*, *Phys. Rev. B* **30** (1984), no. 4 1979.

[111] C. Dotzler, G. Williams, U. Rieser, and A. Edgar, *Optically stimulated luminescence in $NaMgF_3$: Eu^{2+}*, *Appl. Phys. Lett.* **91** (2007), no. 12 121910–121910.

[112] N. Le Masson, A. Box, C. Van Eijk, C. Furetta, and J.-P. Chaminade, *Optically and thermally stimulated luminescence of $KMgF_3$:Ce^{3+} and $NaMgF_3$:Ce^{3+}*, *Radiat. Prot. Dosim.* **100** (2002) 229–234.

[113] H. Takahashi and R. Onaka, *The XUV spectra of $KMgF_3$ and $NaMgF_3$*, *J. Phys. Soc. Japan* **43** (1977), no. 6 2021–2029.

[114] A. Belsky and J. Krupa, *Luminescence excitation mechanisms of rare earth doped phosphors in the VUV range*, *Displays* **19** (1999), no. 4 185–196.

[115] Y. Zhou, S. Feofilov, H. Seo, J. Jeong, D. Keszler, and R. Meltzer, *Energy transfer to Gd^{3+} from the self-trapped exciton in $ScPO_4$: Gd^{3+}: Dynamics and application to quantum cutting*, *Phys. Rev. B* **77** (2008) 075129.

[116] R. D. Cowan, *The theory of atomic structure and spectra*, vol. 3. Univ of California Press, 1981.

[117] Z. Pan, C. K. Duan, and P. A. Tanner, *Electronic spectra and crystal field analysis of Yb^{2+} in $SrCl_2$*, *Phys. Rev. B* **77** (2008), no. 8 085114.

[118] A. P. Sergeev and P. B. Sergeev, *Individual induced absorption bands in MgF_2*, *Quant. Electron.* **38** (2008), no. 3 251–257.

[119] M. Klinger, C. B. Lushchik, T. Mashovets, G. Kholodar', M. Sheĭnkman, and M. Elango, *Defect formation in solids by decay of electronic excitations*, *Phys. Usp.* **28** (1985), no. 11 994–1014.

[120] S. Kück, M. Henke, and K. Rademaker, *Crystal growth and spectroscopic investigation of Yb^{2+}-doped fluoride crystals*, *Laser Phys.* **11** (2001), no. 1 116–119.

[121] O. Rubio, *Doubly-valent rare-earth ions in halide crystals.*, *J. Phys. Chem. Sol.* **52** (1991), no. 1 101–174.

[122] R. Shannon, *Revised effective ionic radii and systematic studies of interatomic distances in halides and chalcogenides*, *Acta Crystallogr., Sect. A: Found. Crystallogr.* **32** (1976), no. 5 751–767.

[123] M. Scrocco, *Electron-energy-loss and X-ray photoelectron spectra of MgF_2*, *Phys. Rev. B* **33** (1986), no. 10 7228.

[124] M. Williams, R. MacRae, and E. Arakawa, *Optical properties of magnesium fluoride in the vacuum ultraviolet*, *J. Appl. Phys.* **38** (1967), no. 4 1701–1705.

[125] M. Yang and C. Flynn, *Growth of alkali halides by molecular-beam epitaxy*, *Phys. Rev. B* **41** (1990), no. 12 8500.

[126] S. Sinharoy, *Fluoride/semiconductor and semiconductor/fluoride/semiconductor heteroepitaxial structure research: A review*, *Thin Solid Films* **187** (1990), no. 2 231–243.

[127] N. Sokolov, S. Gastev, S. Novikov, N. Yakovlev, A. Izumi, and S. Furukawa, *Molecular beam epitaxy of CdF_2 layers on CaF_2 (111) and Si (111)*, *Appl. Phys. Lett.* **64** (1994), no. 22 2964–2966.

[128] N. Sokolov, S. Gastev, A. Y. Khilko, R. Kyutt, S. Suturin, and M. Zamoryanskaya, *CdF_2–CaF_2 superlattices on Si (111): MBE growth, structural and luminescence studies*, *J. Crys. Growth* **201** (1999) 1053–1056.

[129] A. J. Nozik, *Spectroscopy and hot electron relaxation dynamics in semiconductor quantum wells and quantum dots*, *Annu. Rev. Phys. Chem.* **52** (2001), no. 1 193–231.

[130] R. A. Forman, W. Hosler, and R. Blunt, *The bandgap of cadmium fluoride*, *Solid State Commun.* **10** (1972), no. 1 19–24.

[131] C. Paracchini and G. Schianchi, *Electroluminescence in CdF_2 crystals*, *Solid State Commun.* **21** (1977), no. 12 1107–1110.

[132] J. Langer, T. Langer, and B. Krukowska-Fulde, *Multicoloured electroluminescence in CdF_2*, *J. Phys. D: Appl. Phys.* **12** (1979), no. 7 L95.

[133] R. Jones and J. Pollard, *The scintillation properties of cadmium fluoride*, *Proc. Phys. Soc.* **79** (1962), no. 2 358.

[134] M. Ishii and M. Kobayashi, *Single crystals for radiation detectors*, *Prog. Cryst. Growth Charact. Mater.* **23** (1992) 245–311.

[135] S. Benci and G. Schianchi, *Recombination luminescence in pure and rare earth doped CdF_2*, *J. Lumin.* **11** (1976), no. 5 349–355.

[136] N. Sokolov and S. Suturin, *MBE-growth peculiarities of fluoride (CdF_2–CaF_2) thin film structures*, *Thin Solid Films* **367** (2000), no. 1 112–119.

[137] T. Kanazawa, R. Fujii, T. Wada, Y. Suzuki, M. Watanabe, and M. Asada, *Room temperature negative differential resistance of CdF_2/ CaF_2 double-barrier resonant tunneling diode structures grown on Si (100) substrates*, *Appl. Phys. Lett.* **90** (2007), no. 9 092101.

[138] C. Deiter, M. Bierkandt, A. Klust, C. Kumpf, Y. Su, O. Bunk, R. Feidenhans, and J. Wollschläger, *Structural transitions and relaxation processes during the epitaxial growth of ultrathin CaF_2 films on Si (111)*, *Phys. Rev. B* **82** (2010), no. 8 085449.

[139] A. Izumi, Y. Hirai, K. Tsutsui, and N. Sokolov, *Study of band offsets in CdF_2/CaF_2/Si (111) heterostructures using x-ray photoelectron spectroscopy*, *Appl. Phys. Lett.* **67** (1995), no. 19 2792–2794.

[140] G. Valkovskiy, M. Durnev, M. Zamoryanskaya, S. Konnikov, A. Krupin, A. Moroz, N. Sokolov, A. Trofimov, and M. Yagovkina, *Investigation of the structure and luminescence properties of CdF_2-CaF_2: Eu superlattices on Si (111)*, *Phys. Solid State* **55** (2013), no. 7 1498–1504.

[141] N. Sokolov, S. Gastev, A. Y. Khilko, S. Suturin, I. Yassievich, J. Langer, and A. Kozanecki, *Tunneling-assisted autoionization of the localized impurities in nanostructures*, *Phys. Rev. B* **59** (1999), no. 4 R2525.

[142] S. Suturin, S. Basun, S. Gastev, J. Langer, R. Meltzer, and N. Sokolov, *Optical detection of electron transfer through interfaces in CaF_2: Eu–CdF_2 SLs*, *Appl. Surf. Sci.* **162** (2000) 474–478.

[143] V. Chernyshev, A. Abrosimov, S. Gastev, A. Krupin, A. Nikiforov, J. Choi, R. Reeves, S. Suturin, and N. Sokolov, *Energy structure of Eu^{3+} centres in CdF_2–CaF_2: Eu superlattices on silicon*, *J. Phys. Cond. Matt.* **19** (2007), no. 39 395023.

[144] R. Reeves, J. Choi, S. Gastev, A. Krupin, K. Hoffman, and N. Sokolov, *Laser spectroscopy of Eu^{3+} centers in CaF_2: Eu–CdF_2 superlattices*, *J. Alloys Compd.* **451** (2008), no. 1 84–87.

[145] F. Fermi, C. Paracchini, and N. Zema, *Intrinsic luminescence in CdF_2 crystals*, *J. Lumin.* **31** (1984) 108–110.

[146] Y. Wang and N. Herron, *Nanometer-sized semiconductor clusters: materials synthesis, quantum size effects, and photophysical properties*, *The J. Phys. Chem.* **95** (1991), no. 2 525–532.

[147] Y. D. Glinka, S.-H. Lin, L.-P. Hwang, Y.-T. Chen, and N. H. Tolk, *Size effect in self-trapped exciton photoluminescence from SiO_2-based nanoscale materials*, *Phys. Rev. B* **64** (2001), no. 8 085421.

[148] P. Rodnyĭ, I. Khodyuk, and G. Stryganyuk, *Location of the energy levels of the rare-earth ions in BaF_2 and CdF_2*, *Phys. Solid State* **50** (2008), no. 9 1639–1643.

[149] C. Raisin, J. Berger, and S. Robin-Kandare, *UPS and XPS spectra of CdF_2 and SrF_2 and interpretation of optical properties of these compounds*, *J. Phys. C: Solid State Phys.* **13** (1980), no. 9 1835.

[150] A. Bourdillon and J. Beaumont, *The reflection spectra of $SrCl_2$ and CdF_2*, *J. Phys. C* **9** (1976), no. 17 L473.

[151] A. Kalugin and V. Sobolev, *Electronic structure of cadmium fluoride*, *Phys. Rev. B* **71** (2005), no. 11 115112.

[152] G. D. Scholes and G. Rumbles, *Excitons in nanoscale systems*, *Nature Mat.* **5** (2006), no. 9 683–696.

[153] I. Blair, D. Pooley, and D. Smith, *The lifetimes of fast recombination luminescence transitions in alkali halides*, *J. Phys. C: Solid State Phys.* **5** (1972), no. 12 1537.

[154] T. Yanagida, Y. Fujimoto, M. Koshimizu, and K. Fukuda, *Scintillation properties of CdF_2 crystal*, *J. Lumin.* (2014).

[155] T. Takagahara and K. Takeda, *Theory of the quantum confinement effect on excitons in quantum dots of indirect-gap materials*, *Phys. Rev. B* **46** (1992), no. 23 15578.

[156] G. Schinner, E. Schubert, M. Stallhofer, J. Kotthaus, D. Schuh, A. Rai, D. Reuter, A. Wieck, and A. Govorov, *Electrostatically trapping indirect excitons in coupled In x Ga 1- x As quantum wells*, *Phys. Rev. B* **83** (2011), no. 16 165308.

[157] H. M. Assenheim, *Introduction to electron spin resonance*. Hilger & Watts Ltd., 1966.

[158] A. Abragam and B. Bleaney, *Electron paramagnetic resonance of transition ions*. Oxford University Press, 2012.

[159] D. Sholl and J. A. Steckel, *Density functional theory: a practical introduction*. John Wiley & Sons, 2011.

[160] S. Hüfner, *Photoelectron spectroscopy: principles and applications*. Springer, 2003.

[161] E. Kraut, R. Grant, J. Waldrop, and S. Kowalczyk, *Precise determination of the valence-band edge in x-ray photoemission spectra: Application to measurement of semiconductor interface potentials*, *Physical Review Letters* **44** (1980), no. 24 1620.

Appendix A

Additional Experimental Techniques

This thesis refers to several experiments which were not performed as part of this work. For the reader's reference, this appendix gives a qualitative description of the experimental methods.

A.1 Electron Paramagnetic Resonance

Electron paramagnetic resonance (EPR) is a technique for studying materials with unpaired electrons [157, 158]. It works using the physical phenomenon in which electrons in a magnetic field absorb and re-emit electromagnetic radiation. This energy is at a specific resonance frequency which depends on the strength of the magnetic field and the magnetic properties of the electrons.

In the presence of an external magnetic field with strength B_0 an electron's magnetic moment aligns itself either parallel or antiparallel to the field, each alignment having a specific energy due to the Zeeman effect. The separation between the lower and the upper state is $\Delta E = g_{\mathrm{e}}\mu_{\mathrm{B}}B_0$ for unpaired free electrons. Thus the splitting of the electron energy levels is directly proportional to the magnetic field's strength.

In a typical EPR experiment, a collection of paramagnetic centers is exposed to microwaves at a fixed frequency. By increasing an external magnetic field, the gap between the spin energy states is increased until it matches the energy of the microwaves, At this point the unpaired electrons can move between their two spin states. Since there typically are more electrons in the lower state, there is a net absorption of energy, and it is this absorption that is monitored and converted into a spectrum. Figure A.1 shows a simulated absorption for a system of free electrons in a varying magnetic field. The lower spectrum is the first derivative of the absorption spectrum, which is commonly presented in publications.

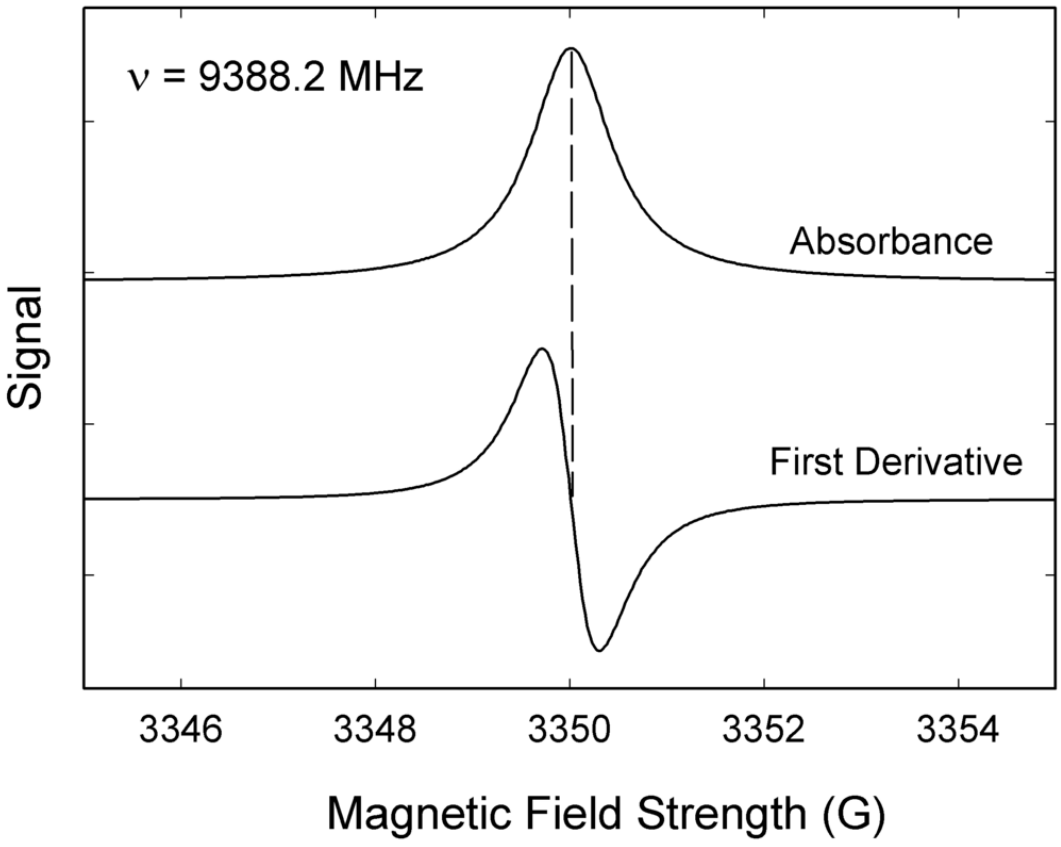

Figure A.1 The simulated absorption spectrum of a system of free electrons in a varying magnetic field.

Spin-orbit coupling of the electron with nearby nuclei causes multi-line spectra because additional energy states are allowed. In such cases, the spacing between the EPR spectral lines indicates the degree of interaction between the unpaired electron and the perturbing nuclei.

When the EPR spectrum has many elements which become difficult to resolve, an extension of EPR which can be used is electron nuclear double resonance (ENDOR) [158]. ENDOR works by subjecting the material to be examined to a magnetic field and then exciting the material sequentially with a microwave followed by radio frequency and monitoring variations in the polarization of the saturated EPR transition as the magnetic field strength is changed.

A.2 Density Functional Theory

Density functional theory (DFT) is a computational quantum mechanical modelling method. It allows the properties of a many-electron system to be determined by using functionals of the spatially-dependent electron density [159].

DFT calculations are based on two fundamental mathematical theorems. The Hohenberg-Kohn theorems state that (1) the ground-state energy from Schrödinger's equation is a unique functional of the electron density and (2) the electron density that minimizes the energy of the overall functional is the true electron density corresponding to the full solution of the Schrödinger equation.

For Kohn-Sham DFT calculations, the intractable many-body problem of interacting electrons in a static external potential is reduced to a tractable problem of non-interacting electrons moving in an effective potential. The effective potential includes the external potential and the effects of the exchange and correlation Coulomb interactions between the electrons. Modeling these interactions is difficult within Kohn-Sham DFT. The simplest approximation is the local-density approximation (LDA), which is based upon fits to the correlation energy for a uniform electron gas. An alternative class of functional is the generalised gradient approximation (GGA) which uses information about the gradient of the local electron density.

A.3 X-ray Photoelectron Spectroscopy

X-ray Photoelectron Spectroscopy (XPS) is a surface chemical analysis technique that can be used to analyze the surface chemistry of a material [160]. XPS spectra are obtained by irradiating a material with a beam of X-rays while simultaneously measuring the kinetic energy and number of electrons that escape from the surface of the material being analyzed.

XPS can be used to measure semiconductor interface potentials as it can accurately measure the change in the position of the valence band [161].

Publications

Chapter 4

Valency of Yb in CaF_2 and SrF_2 crystals measured by XANES, Rosa B. Hughes-Currie, Konstantin V. Ivanovskikh, Jon-Paul R. Wells, and Michael F. Reid, *Manuscript in preparation.*

Chapter 5

Site-selective transient photoluminescence enhancement of impurity-trapped excitons in $NaMgF_3$:Yb^{2+}, Rosa B. Hughes-Currie, Pubudu S. Senanayake, Jon-Paul R. Wells, Michael F. Reid, Giel Berden, Roger J. Reeves, and Andries Meijerink. Phys. Rev. B 88, 104304 (2013).

Chapter 6

Excitons and interconfigurational transitions in CaF_2:Yb^{2+} crystals, Rosa B. Hughes-Currie, Alex J. Salkeld, Konstantin V. Ivanovskikh, Michael F. Reid, Jon-Paul R. Wells ,and Roger J. Reeves. J. Lumin. 158 197-202 (2015).

Vacuum ultraviolet synchrotron measurements of excitons in $NaMgF_3$:Yb^{2+}, Rosa B. Hughes-Currie, Konstantin V. Ivanovskikh, Michael F. Reid, Jon-Paul R. Wells, Roger J. Reeves, and Andries Meijerink. J. Lumin. *In press.*

Dynamics of fundamental excitations in fluoride lattices probed with vacuum ultraviolet radiation, Rosa B. Hughes-Currie, Konstantin V. Ivanovskikh, Michael F. Reid, Jon-Paul R. Wells, Roger J. Reeves, and Andries Meijerink. *Manuscript in preparation.*

Chapter 7

Spectroscopy and relaxation dynamics of intrinsic electronic excitations in CdF_2-CaF_2 superlattices, Konstantin V. Ivanovskikh, Rosa B. Hughes-Currie, Michael F. Reid, Jon-Paul R. Wells, N. S. Solokov, and Roger J. Reeves, *Manuscript in preparation.*